Characterisation and Measurement of Laser Produced Plasma Emission and Applications in Opacity Experiments

Andrew K. Rossall

A thesis submitted for the degree of

Doctor of Philosophy

University of York

Department of Physics

May 2011

Abstract

The work presented in this thesis investigates the characterization of laser produced plasmas and develops applications in opacity experiments using plasma emission as a back-lighting source. A diagnostic is developed to analyse bremsstrahlung emission from hot electrons produced in the laser plasma interaction. Combining a compensating filter technique with an x-ray diode array allows for the hot electron temperature to be deduced with good accuracy (±0.5keV). A layered target comprising 0.8μm Al and 1.0μm Fe is used to investigate the opacity of iron plasma. A laser of modest irradiance (~ 10^{15} W cm^{-2}) is fired onto the aluminium surface, producing Al K_α emission (1.5 keV) which is used to measure the opacity of the conductively heated iron layer. The aluminium plasma is characterized using source broadened spectroscopy and continuum emission analysis. The experimental transmission data is in good agreement with 2D modelling using opacities from the Ionised Materials Package. A line focus back-lighter, produced using a high power laser system, is characterized through imaging the time and spectrally integrated emission profile of the plasma using a crossed-slit camera. The emission profile is used to infer a spatially dependant electron temperature profile. Finally, a Ti K_α back-lighter is used to investigate the temporal evolution of the Rayleigh-Taylor instability in a laser produced plasma. A target, seeded with an initial perturbation between layers of copper and plastic exhibited Rayleigh-Taylor growth within the first 100ps of the interaction with a growth rate of 10 ± 2 ns^{-1}.

Contents

List of Figures

List of Tables

Acknowledgements

First and foremost I would like to thank my supervisor, Prof. Greg Tallents. His willingness to share his time, experience and knowledge has been invaluable throughout the completion of this thesis. The patience and support he has shown me has been immensely helpful and has played an important role in the work presented here.

During my time at the University of York I have had the opportunity to work with some fantastic people, all of whom I am grateful to have worked with in the experiments contained within this thesis. In particular I would like to thank Erik Wagenaars, Lauren Gartside, Lucy Wilson, and Nicola Booth for our long hours spent on experiment and I thank Nigel Woolsey and John Pasley for their guidance and helpful discussions. I would also like to thank Bob Hide, Chief Electronics technician, for constructing the electronics described in chapter 3.

I extend thanks to the Target Area staff at the Central Laser Facility, particularly Margaret Notley, Rob Heathcote, Rob Clarke and Kate Lancaster, without their assistance the experiments would not have been a success.

I would like to express sincere gratitude to Shivanand Chaurasia, Lalitha Dhareshwar and the staff at the Bhabha Atomic Research Centre, Mumbai for our collaboration and their hospitality during our experiment.

Finally I would like to thank my family who has supported me through every trial and tribulation thus far. I especially thank my wonderful fiancée, Emma, her patience knows no bounds and without her support, the work here would not have been possible.

Declaration

I declare that the work presented in this thesis, except where otherwise stated in the next section, is based on my own research and has not been submitted previously for a degree at this or any other university.

Parts of chapters 3, 4, 5 and 6 presented in this thesis have been published in the papers listed in Appendix A.

Andrew. K. Rossall

Role of the Author

This section outlines the role of the author in the work presented in this thesis as high power laser experimentation generally requires a number of team members. In chapter 3, the author is responsible for the design of the compensated channel diode array, including the read-out electronics. The author also collected and analysed the data shown in chapter 3. The read-out electronics were built by Bob Hide, Chief Electronics technician at the University of York. In chapter 4, the author collected the data with the experimental team including S. Chaurasia, L. Dhareshwar, D. Munda, and N. Gupta. The author analysed the experimental data obtained in chapter 4 and h2d simulations were carried out by L. Gartside in conjunction with J. Gaffney and S. Rose, who provided the IMP code data. In chapter 5, the author collected the experimental data in conjunction with the experimental team, consisting of E. Wagenaars, L. Gartside, N. Booth, S. White, M. Notley and R. Heathcote. The author is responsible for the analysis and Ehybrid modelling of the line focus back-lighter using the crossed-slit camera. Transmission measurements and pinhole camera analysis was carried out by E. Wagenaars and modelling using h2d, IMP, and SESAME was done by L. Gartside. In chapter 6, the author collected the data with the experimental team including, I. Bush, K. Lancaster, R. Heathcote and J. Pasley. The author is responsible for the experimental data analysis presented in chapter 6.

For Emma-Lou

1. Introduction

The first maser (microwave amplification by stimulated emission of radiation) was observed by Townes, Zeiger and Gordon [1] at Columbia University, New York in 1954. Townes went on to share the 1964 Nobel Prize in physics with Basov and Prokhorov for their work which led to the construction of the first laser in 1960 by Maiman [2]. Many advances have been made since this first demonstration using a ruby rod and a xenon flash lamp. The advent of the Chirped Pulse Amplification (CPA) scheme introduced a method of amplifying the short pulses that had arisen from improvements in active and passive mode locking. The CPA scheme was first implemented by Strickland and Mourou at the Laboratory for Laser Energetics (LLE), Rochester and was originally designed to be analogous to the amplification used in radar transmission [3].

A short light pulse produced in a laser oscillator is stretched temporally using a system of gratings before being introduced into the gain medium. As a result of the increase in pulse length, the intensity of the pulse remains below the damage threshold of the gain medium, the original limiting factor in maximum output intensity. After amplification, the laser pulse is passed through another series of gratings, reversing the dispersive stretching, reducing the pulse duration to one similar to the input pulse length. This technique allows the production of high power laser pulses in the petawatt regime, and is now being used to explore fascinating new physics with irradiances > 10^{21} W cm^{-2}. Such lasers can potentially heat material to relativistic energies (electron velocities approaching the speed of light) and produce large volume (100μm × 100μm × 100μm) approximately uniform plasmas. Similarly, other laser advances have enabled the development of cheap table-top lasers capable of producing interesting plasmas. The use of a table-top laser with focussed irradiances up to 10^{15} W cm^{-2} is described in this thesis alongside results from more intense lasers.

High power lasers have been used to produce and probe the opacity of dense plasmas. There are difficulties in modelling the atomic and other physics involved in plasma opacity calculations, especially in the low temperature, high density (warm dense matter) regime [4]. Opacity describes how radiation diffuses through a medium as a function of temperature, density and composition of the material. Workshops are regularly held [5] to compare the predictions of opacity from various computer codes under specific conditions, and large discrepancies are regularly seen [6]. As a result of this, experimental benchmarking of these codes is required to ascertain the correct methods for calculation. In astrophysics, knowledge of plasma opacity is required for radiation diffusion modelling of stars [7], and of particular interest, is resolving the discrepancy between helioseismological observations and solar modelling using opacity simulations [8]. In addition, opacity is relevant to inertial confinement fusion (ICF) as accurate data is required to model radiative hydrodynamics [9] and hohlraum physics [10].

In order to probe plasma opacity experimentally, a back-lighter of sufficient intensity is usually required so as to 'outshine' the opaque target plasma, i.e. the transmitted intensity of the back-lighter must be greater than the emission of the opaque plasma. Assuming black-body emission of a uniform sample plasma, the incident back-lighter intensity, I_0, must be such that

$$I_0 \exp(-\sigma L N) \; > \; \Omega \int_{\nu 1}^{\nu 2} \frac{2h\nu^3}{c^2} \frac{1}{e^{\frac{h\nu}{kT}} - 1} d\nu \tag{1.1.1}$$

where σ is the absorption cross-section (see chapter 2), L is the path length through the plasma, N is the number density of absorbers, Ω is the solid angle subtended by the back-lighter, and ν is the frequency of the radiation. An alternative method to experimentally measure opacity includes recording emission from a buried layer target and invoking Kirchhoff's law [11] (see section 2.3.3). Measuring the propagation time of a radiation heat wave (Marshak Wave) [12] can also provide a measure of the frequency averaged (Rosseland) mean opacity.

The method commonly used to investigate opacity employs x-rays emitted from a second laser produced plasma created by irradiating a high Z target [13-16]. Plasma based EUV lasers (often referred to as x-ray lasers for historical reasons) have been generated using a grazing incidence pumping (GRIP) scheme and used to measure longitudinal transmission through plasma at specific wavelengths [17]. The grazing incidence pumping scheme utilises a long laser pulse, normally incident onto a slab target focussed into a line to create a long scale length plasma, to enhance the x-ray lasing by reducing refraction. A second shorter pulse is fired into the pre-pulse plasma, at a grazing incidence, producing the population inversion necessary to generate lasing.

The purpose of utilising grazing incidence pumping in the production of EUV lasers is two-fold; firstly it establishes a travelling wave which is used to pump the x-ray laser, and secondly, by modifying the angle, absorption can be maximised at the optimum density for lasing. The x-ray laser has been used to probe an opaque target, heated by a second optical laser, ensuring the beam passes through unheated and heated material simultaneously to allow for direct comparison on each shot. The experiment demonstrated by Edwards et al. [17] utilised a Ni-like ($1s^22s^22p^63s^23p^63d^{10}$) silver x-ray laser (4d – 4p transition) at 13.9nm to probe a 50nm layer of iron, tamped in plastic, heated by an 80ps pulse containing 6 - 9J. This allowed for the direct comparison between the obtained experimental data and simulated data produced by considering approximately 26 000 tabulated transitions.

When testing simulation results of opacity, iron is often used as a test case for a number of reasons. Firstly, iron is the heaviest element produced via stellar nucleosynthesis, so is particularly relevant to the internal structure of stars. This is especially seen in the case of our sun, as although the abundance of iron is ~30,000 times smaller than that of hydrogen, iron opacity contributes significantly to the radiative transfer in the solar interior, particularly in the region of the interface layer between the radiative and convective zones [18]. Secondly, iron makes for a practical case study with regards to simulations, due to the different methods involved in simulating opacity. There are two commonly used methods in opacity calculations, the unresolved transition array (UTA) and detailed term accounting (DTA) [4] (see section 2.2.5). Iron has enough complexity to enable the averaging methods of UTA and STA to be utilised, but is not so complex as to make detailed term accounting impractical.

Improvements in the understanding and production of high order harmonics [19-21] are now providing a possible new avenue for investigating opacity. High harmonic generation (HHG) can provide a method in which the opacity for a number of different wavelengths could be investigated simultaneously, as opposed to a single wavelength per shot. In a small number of shots, introducing an incremental shift in the fundamental frequency, enough data can be collected to directly measure the Planck and Rosseland mean opacities (discussed in Chapter 2).

When an intense laser pulse is focused into a low density gas, non-linear interactions cause the emission of radiation at integer multiples of the fundamental frequency of the laser. The laser electric field gives rise to a distortion in the atomic potential which in turn allows an electron to tunnel ionise. This free electron is accelerated by the lasers electric field, outwards and back again when the field reverses, causing the electron to recombine with the parent ion, emitting radiation. However, strong ionisation inhibits harmonic production in the gas and as a result the intensity of the laser must be kept below 10^{15} – 10^{16} Wcm^{-2} [22], which in turn limits the intensity of the harmonic, meaning the relationship denoted in equation 1.1.1 is difficult to achieve. A more suitable option for utilising harmonics would be those produced in laser plasma interactions on solid surfaces. It is known that a number of different mechanisms contribute to the production of harmonics in this interaction [22], including resonance absorption, parametric instabilities, ionisation fronts and relativistic nonlinearities. Some of these processes are discussed in Chapter 2. From this point onwards, when harmonic generation is discussed, I refer to the laser plasma interaction at a solid surface.

The advent of x-ray free electron lasers (XFELs), such as FLASH in Hamburg and the LCLS at Stanford, provide further possibilities for opacity experiments. Free electron lasers are created by passing a relativistic beam of electrons through a transverse, periodic magnetic field, causing them to follow a sinusoidal path. The motion of the electrons results in the emission of synchrotron radiation, the frequency of which can be tuned by adjusting the energy of the electron beam or the strength of the magnetic fields. Due to the lack of appropriate x-ray mirrors, the magnetic undulator cannot be placed within a laser cavity to amplify the beam. It is therefore necessary for the XFEL to have a high enough amplification over a single pass of the electron beam. This is achieved via self-amplified spontaneous emission (SASE) and microbunching. As the electron beam enters the magnetic undulator, spontaneous undulator radiation is produced. This radiation then acts as a seed for the remaining section of the undulator. The radiation seed initiates the process of microbunching. Electrons that lose energy to the light wave travel on a sinusoidal path with a larger amplitude than the electrons gaining energy from the light wave. This difference in amplitude causes a modulation of the longitudinal velocity, resulting in the bunching of the electrons close to the position of maximum energy transfer to the light wave. This increase in radiation energy enhances the microbunching effect, causing an exponential increase in the energy of the pulse until all available electrons have been optimised. This process of microbunching produces a high gain XFEL without the requirement of a laser cavity.

The tuneable nature of the free electron lasers would allow opacity to be investigated over a range of wavelengths readily and easily. X-ray free electron lasers could also be used to heat opaque target materials to create warm dense matter, a regime of particular interest as stated. An experiment performed using FLASH in Hamburg by Nagler et al. [23] demonstrates how a sample absorbed the 13.5nm (92eV) x-rays through direct photoionisation from the inner L-shell. Due to an increase in ionisation potential after the first electron was removed, the 92eV photons were unable to eject a second electron, causing the sample to become highly transmissive. The photoionised electrons decay via radiative or Auger decay, the latter transferring energy to the valence electrons, heating the material to the warm dense matter regime (< 25eV in temperature).

A requirement for all opacity experiments is accurate information concerning plasma conditions in both the back-lighter and the opaque target. For this reason a large portion of this work is devoted to modelling and analysing emission from these plasmas to provide high quality data concerning plasma parameters. As previous experiments have normally required high powered laser systems with multiple beams, an investigation has been carried out to examine the possibility of using a single beam, table top laser system to perform opacity experiments.

The outline of this thesis is as follows, chapter 2 will cover the physics of the laser plasma interaction and a discussion of some of the computer modelling codes used. Chapter 3 will describe the development of a solid state diode array for hard x-ray detection for use in opacity experiments. Chapter 4 will examine an opacity experiment which utilises a single beam laser system of modest parameters. Chapter 5 will investigate the spatial temperature distribution of a Germanium back-lighter in an experiment that has a similar set-up to the plasma based x-ray laser experiment by Edwards et al. [17]. Chapter 6 will present an experiment which examines the Rayleigh-Taylor instability within laser produced plasma through use of a Ti K_α back-lighter. Chapter 7 will present the conclusions of this work.

2. Plasma Physics and the Laser Plasma Interaction

This chapter reviews some background physics behind the work presented in subsequent chapters. Section 2.1 presents a discussion of laser plasma interactions, including electromagnetic wave propagation in plasmas and various processes which occur in laser produced plasmas, such as the generation of fast electrons. Section 2.2 examines the atomic physics behind plasma opacity, and includes a discussion of the Rosseland and Planck mean opacities, different methods used for simulating opacity and the need for experimental opacity benchmarking. Section 2.3 reviews the theory of plasma emissivity. Detection of plasma emission is a useful diagnostic for conditions within plasma, as is shown in chapters 3, 4, 5 and 6. Section 2.4 discusses spectral line shapes and broadening effects that can be used to investigate plasma parameters, followed by a description of the models that can be used to determine population dynamics within plasma in section 2.5. The theoretical framework behind three simulation codes, used for the modelling of laser produced plasmas in this work, is discussed in section 2.6.

2.1 The Laser Plasma Interaction

A laser pulse incident onto a solid target is partially reflected and partially absorbed within the material causing localized heating, ablation, ionisation, and subsequently, the expansion of material from the absorption region of the laser. This expansion of material from the target produces a density gradient of approximate scale length $L \approx c_s t$, where c_s is the ion acoustic speed of the plasma and t is the duration of the expansion. The ion acoustic speed is a function of ionisation, ζ, electron temperature, T_e, and ion mass, m_i, with $c_s = \left(\frac{\zeta k T_e}{m_i}\right)^{1/2}$ cm s^{-1}. A laser pulse with sufficient duration will produce a density gradient before the end of the laser pulse which subsequently interacts with the expanding plasma.

2.1.1 Electromagnetic Wave Propagation and Absorption in Plasma

The linear dispersion relationship for a high frequency, planar electromagnetic wave of the form $E(z,t) = E_0\exp[i(kz - \omega t)]$ in a plasma with a uniform density is given by $\omega^2 = \omega_{pe}^2 + k^2c^2$, where ω_{pe} is the density dependant plasma frequency describing charge-density fluctuations within the plasma. The plasma frequency defines the minimum frequency which a light wave must possess when propagating through the plasma as the wave vector k becomes imaginary if $\omega < \omega_{pe}$. The plasma frequency is given by $\omega_{pe} = \left(\frac{n_e e^2}{m_e \varepsilon_0}\right)^{1/2}$, where n_e is the local electron density, and m_e is the mass of the electron. A critical density, $n_c = \frac{4\pi^2 c^2 m_e \varepsilon_0}{e^2 \lambda_L^2} = 1.1 \times 10^{21}\left(\frac{1\mu m}{\lambda_L}\right)^2 cm^{-3}$ [24], can be defined, beyond which a light wave of wavelength λ_L cannot penetrate. Positions within the plasma where $n_e < n_{cr}$ are described as 'under-dense' and positions with $n_e > n_{cr}$ are 'over-dense'.

Laser absorption occurs by inverse bremsstrahlung (see section 2.2) within the under-dense region and near the critical surface at typical densities ≤ 0.01 g cm^{-3} [2]. Beyond the critical surface, lies the 'transport domain' (with densities ranging from ~0.01 g cm^{-3} to solid density) where the absorbed energy from the laser pulse is transported to the ablation surface. This energy is generally transported via the diffusive process of thermal conduction. However, a small component of higher energy electrons ('hot' electrons – see section 2.1.3) can propagate ahead of the thermal conduction front, pre-heating the target. Plasma radiation can also pre-heat the target ahead of thermal conduction. Due to conservation of momentum, ablating plasma causes a shock wave to propagate away from the absorption region, into the solid target, creating the 'compression domain' typically at densities up to 4 times solid. Figure 2.1 demonstrates the different regions.

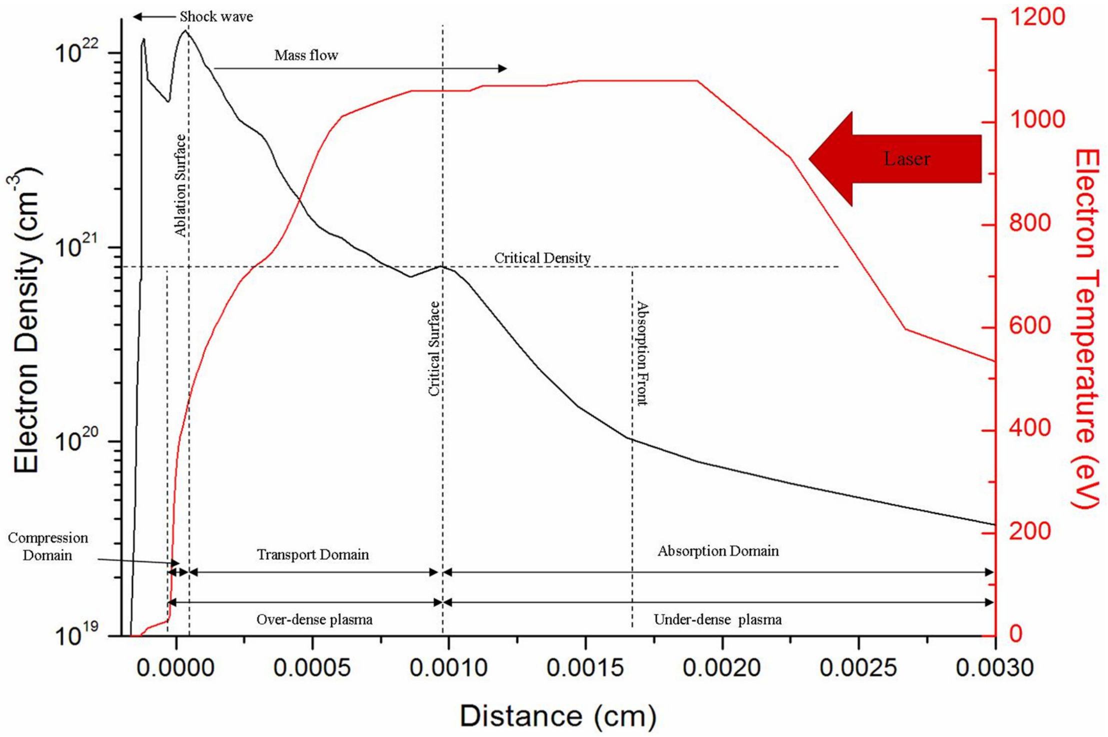

Figure 2.1 Different regions, and typical temperatures and densities in the laser plasma interaction, as simulated by the 1D hydrodynamic code EHYBRID [25] (see section 2.4) for a pre-pulse of 8x10^{12} Wcm^{-2} with duration 300ps and a main pulse of 1x10^{15} Wcm^{-2} of duration 3ps incident 250ps after the peak of the pre-pulse. The profiles are shown for a time corresponding to 9ps after the start of the main pulse.

A self-similar solution [24] describing the one-dimensional expansion of a planar, isothermal plasma shows that the electron density profile of freely expanding plasma can be described by $n_e = n_0 \exp\left(-\frac{x}{c_s t}\right)$. We see in figure 2.1 that the electron density profile does fall approximately exponentially, while the temperature profile is such that there is a steep rise from the ablation surface to an approximately constant value followed by a small drop at larger distances as plasma expansion becomes significant.

A high intensity laser pulse exerts light pressure P_L on the plasma [2];

$$P_L = \frac{I_L}{c}(1+R) \approx 3.3\ Mbar\left(\frac{I_L}{10^{16}\ W\ cm^{-2}}\right)(1+R) \tag{2.1.1}$$

where R is the reflectivity of the laser. The effect of this light pressure is to steepen the density gradient near the critical surface, although localised heating at the critical density can also cause steepening (as can be seen in figure 2.1).

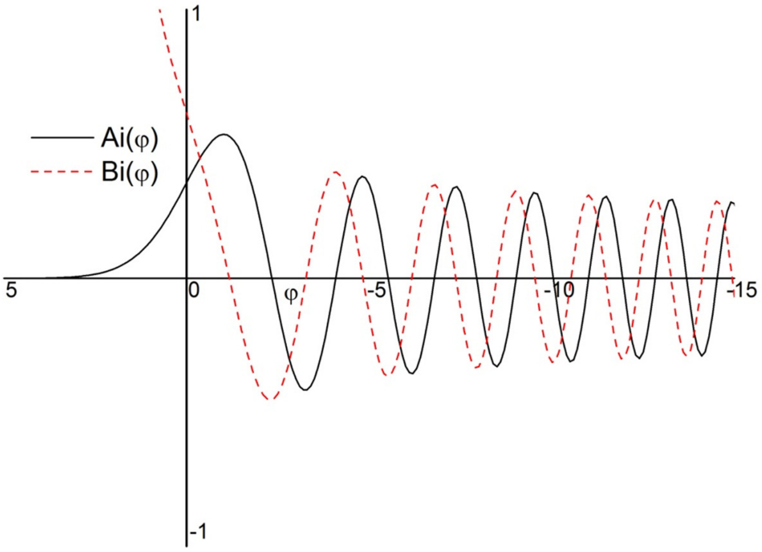

Figure 2.2 Airy values as a function of φ. $Ai(\varphi)$ represents the electric field of the laser pulse.

The electromagnetic propagation of a laser in a plasma density profile can be treated analytically by assuming a linear density profile [2] with $n_e = n_c \frac{z}{L}$, where $z = 0$ is the plasma-vacuum interface and L is the scale length of the plasma such that when $z = L$, then $n_e = n_c$. Using this linear relationship, the dielectric function of a plasma, $\varepsilon = 1 - \frac{n_e}{n_c} = 1 - \frac{z}{L}$, and substitution into the electric field wave equation gives

$$\frac{d^2E(z)}{dz^2} + \frac{\omega^2}{c^2}\left(1 - \frac{z}{L}\right)E(z) = 0. \tag{2.1.2}$$

By changing the variable z to the dimensionless variable φ, where $\varphi = \left(\frac{\omega^2}{c^2L}\right)^{1/3}(z - L)$, one obtains,

$$\frac{d^2E(\varphi)}{d\varphi^2} - \varphi E(\varphi) = 0 \tag{2.1.3}$$

which is known as the Stokes differential equation. The solution to this equation is given by the Airy functions, Ai and Bi, such that

$$E(\varphi) = aAi(\varphi) + bBi(\varphi) \tag{2.1.4}$$

where a and b are coefficients found by examining the solution at the plasma boundaries. The values for Ai and Bi, as a function of φ are shown in figure 2.2.

As $Bi(\varphi) \to \infty$ as $\varphi \to \infty$, $b = 0$ in equation 2.1.4, as the laser cannot penetrate beyond the critical density of the plasma at $\varphi = 0$. Therefore the electric field variation of the laser within the plasma is represented by the Airy function, $Ai(\varphi)$.

2.1.2 Obliquely Incident Laser-Plasma Interaction

The previous analysis assumes a planar electromagnetic (EM) wave normally incident onto a target, with the density gradient opposing the direction of propagation of the laser. If we consider an obliquely incident planar EM wave, with an angle θ between the direction of the density gradient and the direction of propagation of the incident laser pulse, as shown in figure 2.3, the waves are refracted before reaching the critical density surface. With an obliquely incident wave, the wave vector $\boldsymbol{k}$ has an additional constant component in the y-direction. Reflection of the light pulse occurs when $k_z = 0$, where $k_z = \left(\frac{\omega}{c}\right)\cos\theta$, therefore the light is reflected when $n_e = n_c \cos^2\theta$ as shown in figure 2.3.

There are two cases to consider for the polarisation of the electric field with oblique incidence, s- and p- polarised light. For both s- and p-polarised light there is an evanescent wave (which decays approximately exponentially) that penetrates beyond the light reflection point and swells at the critical density to give a large electric field. The swelling of the electric field is due to the resonant response of the plasma when $\omega_{pe} = \omega_L$.

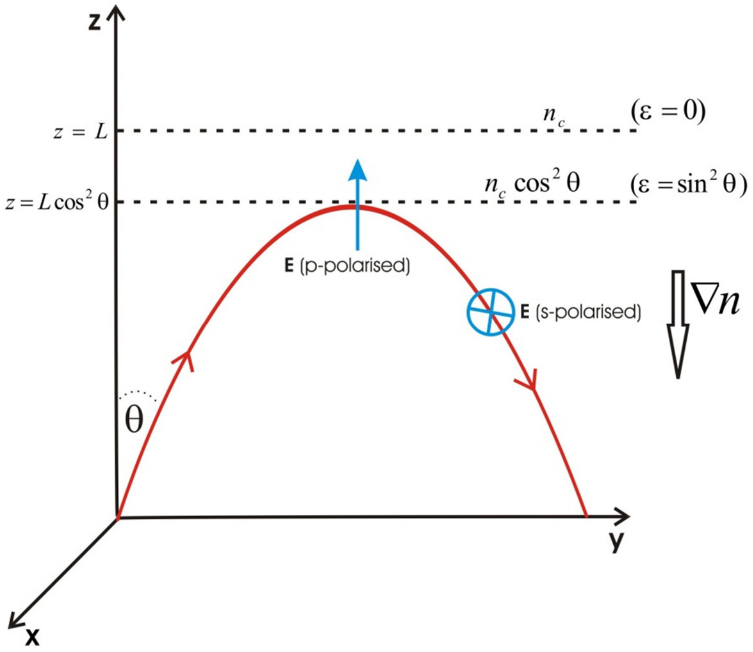

Figure 2.3 Schematic demonstrating a laser pulse obliquely incident onto linearly varying density plasma with $n_e = n_c \frac{z}{L}$.

For s-polarised light, the electric field is in the *x* direction, perpendicular to (or ‘out of’) the plane of incidence (*y*-*z* plane), as shown in figure 2.3. In this case, the large electric field resonantly produced at the critical density is orthogonal to the density gradient. For p-polarised light, the electric field of the laser pulse is parallel to (or ‘in’) the plane of incidence, as shown in figure 2.3. Here there is a component of the electric field which drives charge density fluctuations along the direction of the density gradient, which can be in turn resonantly enhanced by the plasma, producing an electron plasma wave. The energy of this non-linear plasma wave is then absorbed through collisional and collision-less processes. This is referred to as resonance absorption and can provide a source of ‘hot’ electrons.

2.1.3 Hot Electrons

The term ‘hot electron’ describes an electron that has gained a high kinetic energy through its interaction with the electric field of the laser. Unlike inverse bremsstrahlung, where the absorbed energy is used to heat the bulk of the electrons, resonance absorption transfers the absorbed energy to a small group of electrons, resulting in high energies.

The hot electrons are produced by the resonant interaction of the laser electric field with the plasma and therefore the electron energy has a dependence on the value of $I\lambda^2$ of the laser. This stems from the ponderomotive force induced by the high frequency field of the laser, and the relation can be seen simply by examining the equation of motion in the direction of the laser electric field for an electron with charge e and mass m_e we have that,

$$\dot{x} = \frac{eE}{m_e \omega_L} \sin(\omega_L t) \tag{2.1.5}$$

where E is the linearly polarised electric field amplitude and ω_L is the angular frequency of oscillation of the laser electric field. The ponderomotive energy, U_p, is the cycle averaged kinetic energy

$$U_p = \int_0^{2\pi/\omega} \frac{1}{2} m_e \dot{x}^2 = \frac{e^2 E^2}{4 m_e \omega_L^2} \tag{2.1.6}$$

where the electric field of the laser is related to the intensity by

$$I = \frac{1}{2} \varepsilon_0 n c E^2 \tag{2.1.7}$$

where n is the refractive index of the medium, thus

$$U_p = \frac{e^2 I}{2\varepsilon_0 c n m_e \omega_L^2} = \frac{e^2 I \lambda_L^2}{8 \varepsilon_0 c^3 n m_e \pi^2}. \tag{2.1.8}$$

A number of scaling laws have been experimentally deduced [26-28], relating $I\lambda^2$ of the laser to the hot electron temperature. Two commonly accepted scaling laws are [2]

$$T_h(keV) = 10 \left(\frac{I_L \lambda_L^2}{10^{15} Wcm^{-2} \mu m^2}\right)^{0.30 \pm 0.05} \quad \text{(for } I\lambda^2 \geq 10^{15} \text{ Wcm}^{-2}\mu\text{m}^2\text{)} \tag{2.1.9}$$

and

$$T_h(keV) = 10 \left(\frac{I_L \lambda_L^2}{10^{15} Wcm^{-2} \mu m^2}\right)^{2/3} \quad \text{(for } I\lambda^2 \leq 10^{15} \text{ Wcm}^{-2}\mu\text{m}^2\text{).} \tag{2.1.10}$$

Hot electron generation in laser produced plasmas and the subsequent interaction with matter is currently a much debated topic due to the relevance with inertial confinement fusion [27]. These high energy particles propagate ahead of the laser induced shock wave and pre-heat the target material, changing the compression hydrodynamics of the fusion capsule. High velocity electrons could also be used to transfer energy into the high density fuel created through the laser ablation of the outer shell of the fusion capsule, igniting the fusion reaction (known as fast ignition) [29].

2.1.4 Generation of High Harmonics

The process of resonance absorption discussed above is also of particular significance to the generation of high harmonics at the critical density. Resonance absorption provides a large ponderomotive force which causes a localised oscillation around the critical density. If a component of the electric field lies in the direction of the density gradient, an electrostatic charge separation is produced and the wave is no longer entirely sinusoidal and as the EM wave cannot penetrate the over dense region of the plasma, a non-propagating, localised, electrostatic oscillation is established. As the motion of the electrons is along the direction of the plasma density gradient, the oscillation generated is non-sinusoidal and so contains high order Fourier components which generate harmonics of the fundamental frequency, ω_L. It is useful to note that these non-sinusoidal oscillations can also be produced via vacuum heating or the Lorentz force when the electrons move relativistically [30].

High harmonic generation is of particular interest in opacity experiments. If one were able to achieve a high enough intensity of the harmonics to achieve the condition described by equation 1.1.1, then it would enable a range of frequencies to be probed in a single shot. Introducing a slight shift in the fundamental frequency, would cause the produced harmonics to also shift, meaning enough data could be acquired to directly measure the Planck and Rosseland mean opacities (discussed in the next section) in a small number of shots [31].

2.2 Plasma Opacity

Opacity describes the interaction of radiation within a medium, i.e. the scattering and absorption processes, and is a frequency-dependant measure of the impenetrability of a medium to electromagnetic radiation. Plasma opacity can be difficult to model computationally due to the sheer number of possible transitions and processes within a hot, dense plasma with a range of ionisation species, temperatures and densities.

As radiation propagates through plasma, photons are absorbed resulting in a loss of overall radiation intensity when exiting the medium. The reduction in intensity, described by the transmission, $T=I/I_0$, where I_0 is the initial intensity and I is the transmitted intensity, is given by

$$T = \exp\left(-\int_0^x \kappa_\nu \rho dx\right) = \exp\left(-\int_0^x \alpha_\nu dx\right) \tag{2.2.1}$$

where κ_ν is the opacity (cm^2/g), ρ is the material density (g/cm^3), x is the thickness of the medium, and α_ν is the absorption coefficient (cm^{-1}). The absorption coefficient of plasma can be calculated using [32]

$$\alpha_\nu = n_j \sigma_{j,k} = \frac{h\nu}{4\pi} B(j,k) n_j \mathcal{L}(\nu) \tag{2.2.2}$$

where n_j is the number density of particles of type j, σ_{jk} is the cross-section for the scattering/absorption process being considered between energy levels j and k, $\mathcal{L}(\nu)$ is the absorption line profile (see section 2.4) and $B(j,k)$ is the Einstein B coefficient. The difficulty in calculating the opacity using equation 2.2.2 comes from calculating atomic energy level populations, degrees of ionisation and excitation, and in determining the cross-sections for the various processes.

2.2.1 Free-Free Absorption

Inverse bremsstrahlung (free-free absorption), where a photon is absorbed by an electron in the presence of an ion, is particularly relevant to photon energies of a couple of eV or less. The cross-section for this process is related to the ion and electron density, n_i and n_e, the ionisation, ζ, and the photon frequency, ω, and is given by [33]

$$\sigma_{ff} = \frac{32\pi^3}{3\sqrt{3}} \frac{e^6(\hbar c)^2}{m_e c^2} \frac{1}{(2\pi m_e c^2 k T_e)^{1/2}} \zeta n_i n_e \frac{1}{(\hbar\omega)^3} g_{ff}(\hbar\omega) \tag{2.2.3}$$

where g_{ff} is the Gaunt factor with value approximately equal to unity [34].

2.2.2 Bound-Free Absorption

Photo-ionisation processes (bound-free absorption), exhibit a series of absorption edges in the absorption coefficients corresponding to different ionisation stages. Photoionisation is particularly relevant in optically thick plasmas ($\alpha_\nu D \geq 1$, where D is the thickness of the plasma) due to the mean free path of the photon being smaller than the dimensions of the plasma. There are a number of different methods to calculate the cross-section for photo-ionisation, each with a different level of accuracy. The simplest method is to calculate the cross-section for K-shell electrons only, where for a photon with energy above the binding energy of the K-shell, the cross-section is given by [33]

$$\sigma_{bf}^{(K-shell)}(\hbar\omega) = \frac{8\pi e^2}{3 m_e c^2} \alpha^4 Z^5 2^{5/2} \left(\frac{m_e c^2}{\hbar\omega}\right)^{7/2} \tag{2.2.4}$$

and with a photon energy below the binding energy, $\sigma_{bf}^{(K-shell)} = 0$. In equation 2.2.4, α is the fine structure constant and Z is the atomic number of the plasma. A more sophisticated model includes an analysis of the explicit hydrogenic wavefunction to calculate the cross-section for hydrogen-like ions. The cross section for H-like ions is given by [33]

$$\sigma_{bf}^{(H-like)} = \frac{64\pi n_p \hbar}{3^{3/2} m_e c} \frac{1}{Z^2} \left(\frac{\left|E_{\zeta-1,n_p}\right|}{\hbar\omega}\right)^3 \tag{2.2.5}$$

which considers the binding energy, $E_{\zeta-1,n_p}$, of an electron in shell n_p. Work has been carried out to extend the theory further to consider inner shell electrons in complex ions [35-37]. The main difficulty in calculating the total bound-free cross section is performing a weighted sum of the absorption coefficients of all ionisation stages and excitation levels contained within a plasma.

2.2.3 Bound-Bound Absorption

Line photo-absorption occurs when an incident photon has the same energy as the difference between two bound electron states, resulting in an electron excited from a lower energy level to a higher level. In order to deduce the line photo-absorption cross-section, one needs to determine the degeneracies n_u and n_l for the upper and lower levels, the oscillator strength, $f_{u\text{-}l}$, for the transition and assign a normalised line profile, $\mathcal{L}(\hbar\omega)$ (discussed in section 2.4). The cross-section is then given by [33],

$$\sigma_{bb} = 2\pi^2 r_0 \hbar c \frac{n_l}{n_u} f_{u\rightarrow l} \mathcal{L}(\hbar\omega) \tag{2.2.5}$$

where $r_0 = e^2/mc^2$ is the electron electromagnetic radius.

The final process to consider is scattering of the light by electrons (Thompson or Compton scattering if the electron is relativistic) which can dominate at very high plasma temperatures. The Thompson scattering cross-section is independent of temperature with the classical cross section [33], σ_{th},

$$\sigma_{th} = \frac{8\pi}{3} r_0^2 \tag{2.2.6}$$

It has been found that free electron degeneracy has an effect on the contribution of Thompson scattering to the total opacity [38]. This is especially relevant in high density plasmas such as those found in the central region of the sun. For accurate opacity calculations, this must be taken into account by introducing a correction factor [39] to equation 2.2.6 that is dependent upon the temperature and density of the plasma.

2.2.4 Rosseland and Planck Mean Opacities

As the opacity of plasma is photon frequency dependant, it is useful to be able to refer to some average value that can be determined for a certain frequency range. There are two such averages that can be considered, each valid for different plasma conditions. The

Rosseland mean opacity is applicable when plasma is optically thick, (when $\alpha_\nu D \geq 1$, where D is the thickness of the plasma) and radiation propagation can be treated as a diffusion process. The Rosseland mean opacity is the average opacity, harmonically weighted by the temperature derivative of the Planck black body equation. The Rosseland mean opacity, κ_R, can be expressed as [33]

$$\frac{1}{\kappa_R} = \frac{\int \frac{1}{\kappa_\nu} \frac{dB_\nu}{dT} d\nu}{\int \frac{dB_\nu}{dT} d\nu} \tag{2.2.7}$$

where κ_ν is the frequency dependant opacity as in equation 2.2.1 and B_ν is the Planck black body function. The Planck mean opacity, κ_p, is more relevant when plasma is optically thin, (when $\alpha_\nu D \ll 1$) and is weighted using the Planck black body equation, such that [33]

$$\kappa_P = \frac{\int \kappa_\nu B_\nu d\nu}{\int B_\nu d\nu}. \tag{2.2.8}$$

In both equations 2.2.7 and 2.2.8, the Planck equation and its temperature derivative is

$$B_\nu(\nu, T) = \frac{2h\nu^3}{c^2} \frac{1}{e^{\frac{h\nu}{kT}} - 1} \tag{2.2.9}$$

$$\frac{dB_\nu}{dT} = \frac{2h^2\nu^4}{c^2(kT)^2} \frac{e^{\frac{h\nu}{kT}}}{\left(e^{\frac{h\nu}{kT}} - 1\right)^2} \tag{2.2.10}$$

It is often useful to use approximations when examining opacity. One such approximation is Kramer's law [40], which states that, $\kappa_\nu \propto \rho T^{-1/2}$, and that the Rosseland mean opacity, $\kappa_R \propto \rho T^{-7/2}$, where ρ is the density of the material. The Kramer opacity is generally applicable when free-free absorption is the dominant absorption process.

2.2.5 Opacity Simulations

Numerous computer codes have been written to simulate opacity. There are some large discrepancies between the codes that need resolving, particularly when simulating warm dense matter [41]. The codes available use one of 3 general methods for opacity simulation. The average atom (AA) model assumes all atoms within a plasma are identical and have the same ionisation and excitation as the average values of the plasma before calculating the opacity. This method is not particularly accurate due to the complex distribution of ionisation species and levels of excitation within a plasma.

The unresolved transition array (UTA) method does not resolve each individual term or multiplet within the bound-bound opacity calculation, and therefore does not require a detailed line shape. It instead assumes that lines associated with terms and multiplets overlap, and can be treated as a single line with a Gaussian line shape. This is the case when the number of bound electrons increases so as to create a spectrum with a large number of closely spaced lines, with spacing smaller than their width, making them unresolvable. Each transition array is primarily characterised by the first two moments of the spectral distribution, i.e. the average energy and the spectral width [42]. However, in some cases [43] the skewness (third moment and measure of asymmetry in the spectral distribution) must be considered to allow for a non-symmetrical line shape.

The third method for opacity calculation is generally accepted as the most accurate but the most computationally intensive. Detailed term accounting (DTA) takes into account every possible process a photon could undergo when traversing a plasma. This method requires detailed line shapes for all transitions which must include any line broadening mechanisms (discussed in section 2.4). The UTA approach is more suitable for the heavier atoms with large numbers of lines present, and the DTA approach is more suitable for the lighter elements.

The issue that arises from using computer codes is the lack of experimental evidence. In an astronomical sense, plasma opacity is not directly observable and thus makes it difficult to compare theory and experiment directly. High power laser experiments, with carefully controlled conditions, allow for plasma opacity data to be collected in order to benchmark these codes and confirm their accuracy.

2.3 Emissivity of Plasma

Section 2.2 discussed radiation absorption processes within a plasma. A similar analysis can be applied to emission radiating from a plasma, as the inverse of the opacity processes.

2.3.1 Free-Free Emission

Bremsstrahlung (free-free emission) produces a continuum of radiation where the logarithm of the x-ray energy spectrum is a straight line when the electron distribution is a Maxwellian. Often laser produced plasmas are best represented using a bi-Maxwellian structure due to the presence of hot electrons (see section 2.1). The plasma is described by two temperature components, a thermal (or 'cold') temperature, T_c, representing the bulk of the plasma electrons, and a suprathermal (or 'hot') temperature, T_h, describing the smaller number of high energy electrons produced by the interaction of the laser electric field with the plasma. A sample bremsstrahlung x-ray spectrum for aluminium is shown in figure 2.4, assuming a bi-Maxwellian structure, an electron density of $1\text{x}10^{21}$ cm^{-3}, (critical density for a 1μm laser), a thermal temperature of 500eV and a suprathermal temperature of 10keV. This spectrum shows that, for the example considered, the emission of photons with energy $h\nu <$ 1keV is dominated by the thermal region of the plasma and the emission of photons with energies above 1keV is dominated by the suprathermal component. The free-free emission from plasma can be calculated [33] using

$$P_{ff}(\hbar\omega)d(\hbar\omega) = \frac{32}{3}\left(\frac{\pi}{3}\right)^{1/2} \frac{e^4}{m_e^2 c^3}\left(\frac{R_y}{kT_e}\right)^{1/2} \zeta^2 n_i n_e \exp\left(-\frac{\hbar\omega}{kT_e}\right) d(\hbar\omega) \tag{2.3.1}$$

where P_{ff} is the energy (eV) emitted in a 1eV spectral region around the photon energy $\hbar\omega$ per unit volume and time, R_y is the Rydberg energy, and the other symbols used have the same meanings as in equation 2.2.3. As with free-free absorption, a multiplicative Gaunt factor, g_{ff}, can be introduced to account for quantum mechanical effects. To account for a two-temperature electron distribution, equation 2.3.1 is calculated for both temperatures and the total emission is given by the summation (figure 2.4), taking into account the smaller number of hot electrons, n_h, in comparison to the number of cold electrons, n_c, by introducing a relative fraction, f, such that $n_h = fn_c$.

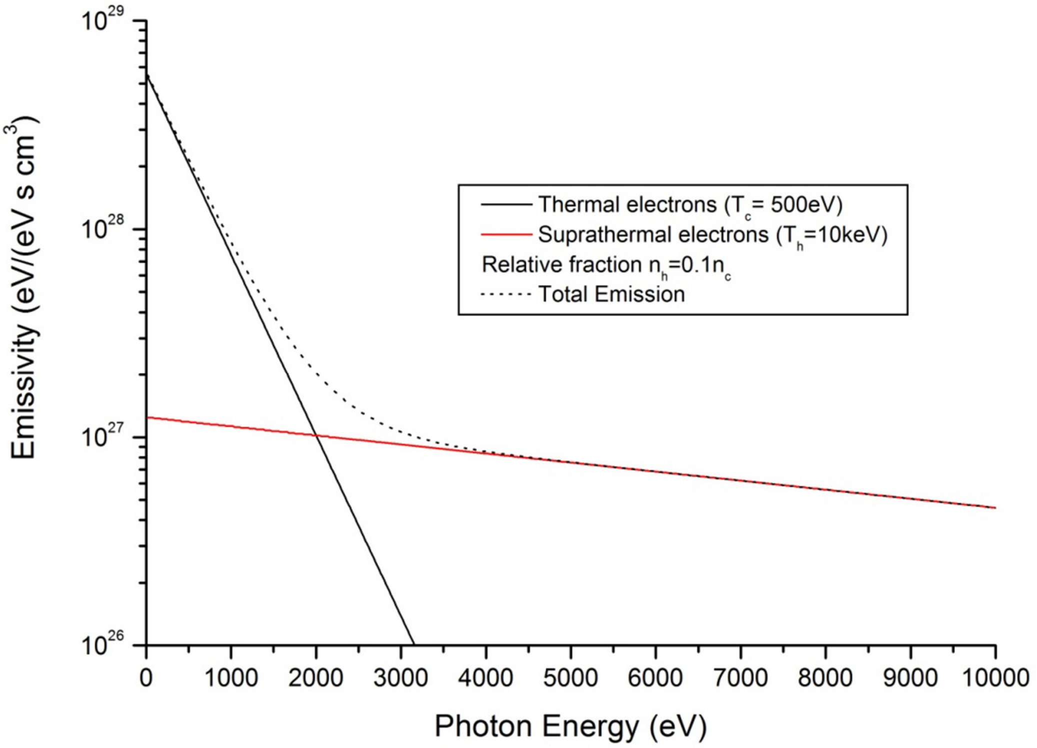

Figure 2.4 Two-temperature component x-ray energy spectrum due to free-free emission (bremsstrahlung) for an aluminium plasma with density n_e=1x10^{21} cm^{-3} and assuming the number of hot electrons consists of 10% of the number of cold electrons.

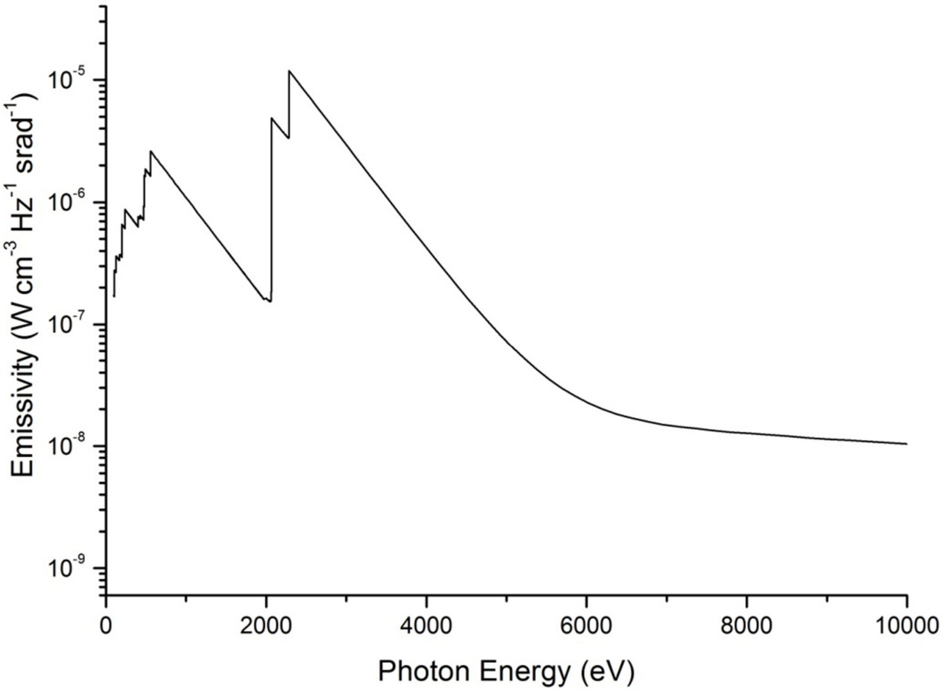

Figure 2.5 Bound-free contribution to continuum emission showing edge structure. Calculated using the spectral modelling code FLYCHK [44] for aluminium with n_e=1x10^{21}cm^{-3}, T_c=500eV, T_h=10keV, and with the number of suprathermal electrons as 10% of the total number of electrons.

2.3.2 Free-Bound Emission

Recombination radiation (free-bound) occurs when an electron recombines with an ion, emitting a photon, and contributes to the continuum emission spectrum. This type of emission contains an 'edge' structure (figure 2.5) corresponding to the binding energies of the various ionisation states. For photons with energy greater than the binding energy, $E_{\zeta-1,m}$, of the ion after recombination, the power emitted due to a free-bound process is given by [33]

$$P_{fb} = \frac{64}{3}\left(\frac{\pi}{3}\right)^{1/2} c r_0^2 \zeta n_i n_e \left[\left(\frac{E_{\zeta-1,m} - \Delta\chi_{\zeta-1}}{kT_e}\right)\right]^{3/2} \times \left(\frac{1}{n_p^3}\right) \exp\left(-\frac{\hbar\omega}{kT_e}\right)\left[1 - P_{\zeta,m}\right] \tag{2.3.2}$$

where m indicates the quantum numbers of the state, $m = (n_p, l)$, $\Delta\chi_{\zeta-1}$ is the continuum lowering due to an increased plasma density and $P_{\zeta,m}$ is the population probability of the final bound state. The contribution to the total continuum emission by recombination radiation is shown in figure 2.5 and is calculated using the spectral modelling code FLYCHK [44] (discussed in section 2.6.2).

2.3.3 Bound-Bound Emission

Spectral line emission (bound-bound) is emitted when an electron decays from an excited state to a lower energy level, emitting a photon with energy equal to the difference between the levels. The power of line emission can be calculated using [33]

$$P_{bb} = N_{\zeta,m'}\hbar\omega_{\zeta,m'\to\zeta,m}A(\zeta,m' \to \zeta,m)\mathcal{L}(\hbar\omega) \tag{2.3.3}$$

where ζ is the ion charge, m and m' are the lower and upper states respectively, $\hbar\omega_{\zeta,m'\to\zeta,m}$ is the energy of the transition and thus the emitted photon energy, $N_{\zeta,m'}$ is the density of ions with charge and state $(\zeta,\ m')$, $A(\zeta,m' \to \zeta,m)$ is the Einstein A coefficient for the decay from state m' to m and $\mathcal{L}(\hbar\omega)$ is the normalised line shape. Line emission is characteristic of the element and the plasma conditions from which it originated and as such can be used to characterise the laser produced plasma. K-alpha (K_α) emission is of particular interest to this work (see chapters 4 and 6) and originates when an electron has a transition from the L-shell of an ion to fill a vacancy in the innermost K-shell, emitting characteristic radiation at a specific wavelength. In laser plasmas, the vacancies in the K-shell are predominantly caused by the interaction with hot electrons generated by the laser electric field, so K_α emission can be assumed to only occur during the laser interaction, giving a well defined time of emission.

Now that absorption and emission processes within plasma have been discussed, it is useful to note that even though it is stated in section 2.2 that plasma opacity is not directly observable; Kirchhoff's Law can be used to estimate plasma opacity. Kirchhoff's Law states that, in equilibrium, the emissivity of a plasma is related to its absorptivity by

$$\frac{\eta_\nu}{\alpha_\nu} = \frac{2h\nu^3}{c^2}\frac{1}{e^{\frac{h\nu}{kT}} - 1} = B_\nu(\nu, T) \tag{2.3.4}$$

where η_ν is the emission coefficient, related to the Einstein A coefficient in a relationship similar to that of the absorption coefficient, α_ν, in equation 2.2.2. By detecting the radiation emitted from plasma, one can estimate its absorption and thus the opacity.

2.4 Spectral Line Shapes and Line Broadening Effects.

The profile associated with line emission can be used to diagnose conditions within plasma. One such method examines broadening effects that have different dependences on the conditions surrounding the ion emitting the radiation. The line profile introduced in sections 2.2 and 2.3 is a function normalized to unity and describes the shape of a spectral line such that

$$I(\omega)d\omega = I_0\mathcal{L}(\omega)d\omega \tag{2.4.1}$$

where $I(\omega)$ is the number of photons emitted within the frequency range ω to $\omega + d\omega$ and I_0 is the total number of photons emitted in the spectral line. The line profile function is generally described by either a Gaussian or Lorentzian distribution or a convolution of the two known as a Voigt function.

2.4.1 Line Broadening

There are a number of broadening mechanisms that can affect the shape and width of a spectral line. The minimum width a spectral line can have is determined by natural line broadening and is due to the finite lifetime of ionic excited states and results in a Lorentzian profile. This process is the smallest of the broadening mechanisms and as a result is generally difficult to detect due to effects from other processes.

Doppler broadening originates from the motion of the emitting ions which results in a difference in frequency between the detected photon in the laboratory frame and the emitted photon in the moving frame of the emitting ion. For a Maxwellian distribution of velocities, the net result is the broadening of the spectral line into a Gaussian shape with a width dependent upon the temperature of the plasma, i.e. the higher the temperature, the faster the ion, the greater the line width.

Two additional broadening mechanisms are due to the interaction of the emitting ion with surrounding particles within the plasma and are collectively known as pressure broadening. Electron impact broadening occurs when the emitting ion undergoes a collision with a free electron within the plasma. The effect of this process is to produce a shifted Lorentzian profile with a width which is proportional to the electron density and inversely proportional to the square root of the plasma temperature [33]. Quasi-static Stark broadening occurs when the radiating ion interacts with another slow moving ion. The slow moving ion generates a fluctuating static electric field on the emitting ion which in turn causes the energy levels to split and shift as described by the Stark effect. The result of this process is to produce an almost Lorentzian line profile with a slightly stronger decrease in the wings of the line which is proportional to the distribution of the electric field strength within the plasma [33].

One final broadening effect that is relevant to the experimental measurement of line width, as is shown in chapter 4, is that of source broadening. In this case, the linear source size of the plasma causes photons of the same wavelength, originating from discrete regions of the plasma, to strike different areas on the dispersion element (see figure 2.6). As the dispersion angle is the same for photons of the same energy, the line is broadened on the recording media (e.g. CCD) as a result. This results in a broadening mechanism that acts as an ‘emission map’ of the laser produced plasma. This effect is covered in more detail in chapter 4.

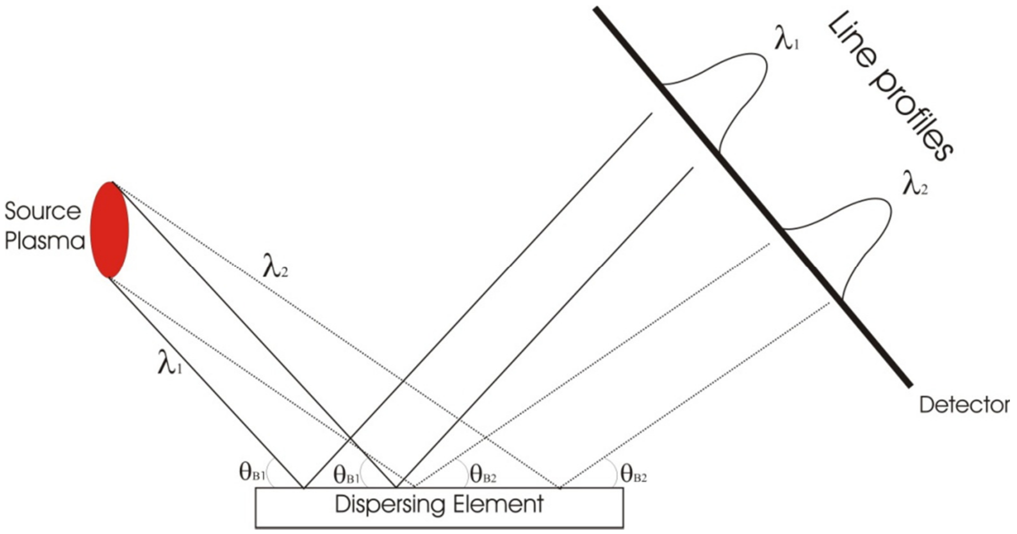

Figure 2.6 Source size line broadening (not to scale) showing the effect on two different wavelengths, λ_1 and λ_2, with Bragg angles θ_{B1} and θ_{B2} respectively, resulting in Gaussian line profiles at the detector.

2.5 Population Dynamics

As discussed in the previous sections, one of the issues when modelling laser produced plasmas is the complex distribution of ionisation stages and levels of excitation. There are a number of approximations that can be used in order to establish the population distribution within plasma at a specific temperature.

2.5.1 Local Thermodynamic Equilibrium (LTE)

Thermodynamic equilibrium occurs when the rate of each process within a plasma is exactly equal to its inverse process, the electron and ion velocities are described by a Maxwell-Boltzmann distribution, and the photons have a Planck energy distribution. Local thermodynamic equilibrium is applicable when the size of a plasma is smaller than the mean free path of photons emitted from within the plasma, yet larger than the collision length of the electrons and ions and the population densities of quantum states (but not the radiation field) are in thermal equilibrium [33]. For plasma in LTE, the ratio between the partial ion densities of each ionisation stage, N_ζ, can be deduced using the Saha equation,

$$\frac{N_\zeta}{N_{\zeta-1}} = \frac{2}{n_e}\left(\frac{mc^2kT_e}{2\pi(\hbar c)^2}\right)^{3/2}\frac{U_\zeta}{U_{\zeta-1}}\exp\left(-\frac{E_{\zeta-1}-\Delta\chi_{\zeta-1}}{kT_e}\right) \tag{2.5.1}$$

where $U_\zeta = V\left(\frac{m_i c^2 kT_e}{2\pi(\hbar c)^2}\right)^{3/2}\sum_m \exp\left(-\frac{E_{\zeta,m}}{kT_e}\right)$ is the partition function of an ion of charge ζ in quantum state m in a plasma with volume V. The Saha equation can be used for each ionisation state to form a set of homogenous linear equations which can be solved provided the following conditions are met

$$\sum_{\zeta=0}^{Z} N_\zeta = n_i \tag{2.5.2}$$

and

$$n_e = \sum_{\zeta=0}^{Z} \zeta N_\zeta. \tag{2.5.3}$$

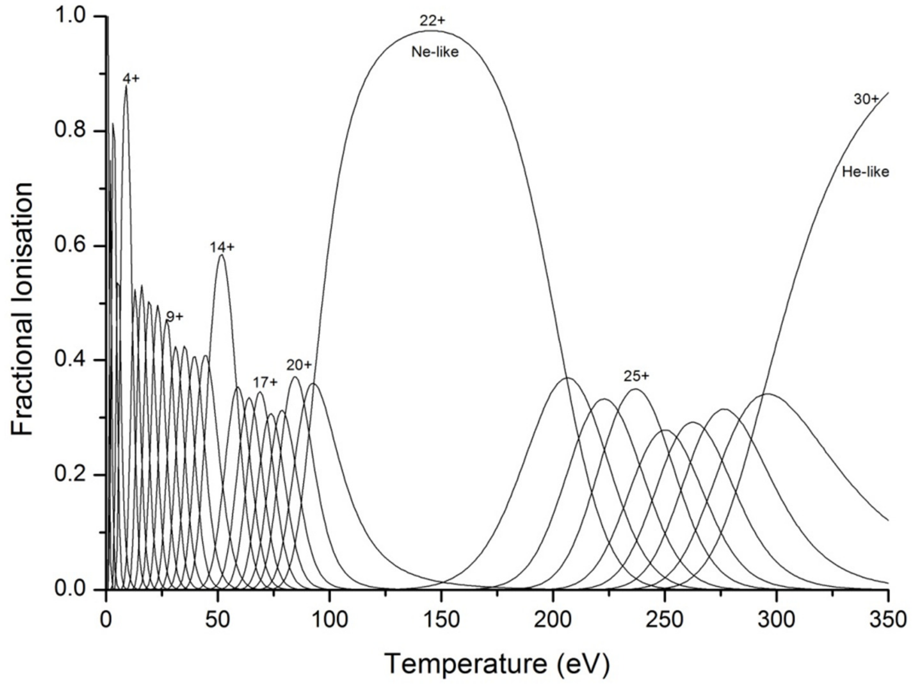

Figure 2.7 Fractional ionisation plot for germanium (*Z*=32) at n_e=1x10^{21} cm^{-3}, assuming LTE.

The relationships denoted by equations 2.4.2 – 2.4.4 have been incorporated into a computer code written in FORTRAN in order to deduce the fractional ionisation of an element for a range of temperatures (figure 2.6). The behaviour of the average ionisation according to the LTE approximation for germanium is shown in figure 2.7.

Once the charge state distribution for an element has been determined, the Boltzmann equation can be used to deduce the distribution of excited states. The notation, $N_{\zeta,m}$, is used to represent the density of ions with charge ζ in quantum state m (where m=0 is the ground state), where

$$N_{\zeta} = \sum_{m=0}^{M_{\zeta}} N_{\zeta.m} \tag{2.5.4}$$

and M_{ζ} is the maximum number of excited states for a particular ionisation level. The Boltzmann equation states

$$\frac{N_{\zeta,m}}{N_{\zeta}} = \frac{g_{\zeta,m}}{U_{\zeta}} \exp\left(-\frac{E_{\zeta.m}}{kT_e}\right) \tag{2.5.5}$$

where $g_{\zeta,m}$ is the statistical weight of state m within an ion of charge ζ. Combining the Saha and Boltzmann equations (2.5.1 and 2.5.5) enables a full description of the population distribution for a plasma with temperature T_e to be deduced.

2.5.2 Coronal Equilibrium

The coronal equilibrium approximation is applicable in low density, optically thin plasmas. Due to the low plasma density, collisions between particles are infrequent and thus the collisional excitation rate is low in comparison to the spontaneous decay rate. As a result, the majority of the ions can be assumed to be in their ground state, simplifying the population distribution. The process of collisional de-excitation can also be neglected as the rate of radiative de-excitation is much greater. The main processes occurring in coronal plasmas are electron impact ionisation, and radiative and dielectronic recombination, the rates of which are equated in order to deduce the charge state distribution. Hence for coronal equilibrium, the distribution of charge states is given by [33]

$$\frac{N_\zeta}{N_{\zeta-1}} = \frac{\mathcal{I}_{\zeta-1\to\zeta}}{\mathcal{R}^{(r)}_{\zeta\to\zeta-1} + \mathcal{R}^{(d)}_{\zeta\to\zeta-1}} \tag{2.5.6}$$

where $\mathcal{I}_{\zeta-1\to\zeta}$ is the rate of electron impact ionisation, $\mathcal{R}^{(r)}_{\zeta\to\zeta-1}$ is the rate of radiative recombination and $\mathcal{R}^{(d)}_{\zeta\to\zeta-1}$ is the rate of dielectronic recombination. Calculation of these different rates can be somewhat problematic, however there are approximations that can be used [33]. The behaviour of the average ionisation, as calculated using the coronal equilibrium approximation, as a function of temperature is shown in figure 2.7 with a comparison to the average ionisation as calculated by the LTE approximation.

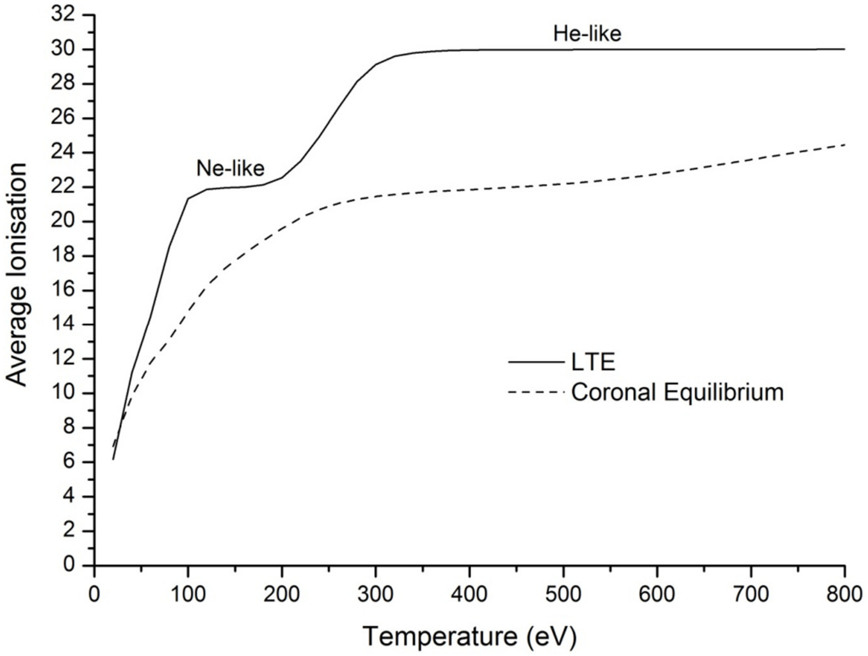

Figure 2.8 Average ionisation as a function of temperature for germanium at an electron density of n_e=5x10^{20} cm^{-3} using the LTE and coronal approximations.

2.5.3 Collisional-radiative steady state (CRSS)

The collisional-radiative steady state (CRSS) approximation relies on all of the rates of population and de-population being equal in a steady state plasma in order to determine the population distribution. Due to the large number of processes involved, the calculations can become rather complex and as a result often the excited state distribution is not considered using this model and obtained elsewhere (for example from the LTE model). This reduces the number of rate coefficients to those involving ionisation and recombination only. The ionisation distribution is then obtained by considering the rates of, electron impact ionisation $\mathcal{I}_{\zeta\to\zeta+1}$, radiative and dielectronic recombination (two-body interactions), $\mathcal{R}^{(2)}_{\zeta+1\to\zeta}$ and 3-body recombination $\mathcal{R}^{(3)}_{\zeta+1\to\zeta}$ respectively. The distribution is then determined by

$$\frac{N_{\zeta+1}}{N_\zeta} = \frac{\mathcal{I}_{\zeta\to\zeta+1}}{\mathcal{R}^{(2)}_{\zeta+1\to\zeta} + n_e\mathcal{R}^{(3)}_{\zeta+1\to\zeta}} \tag{2.5.7}$$

where again approximations [33] are used to estimate the various rate coefficients.

2.6 Computer Simulation Codes

There are a number of different computer codes available for the simulation of a wide range of plasma parameters. The purpose of this section is to introduce three of these codes that are used in the work contained in this thesis.

2.6.1 EHYBRID

EHYBRID is a hydrodynamic/atomic code developed by G.J. Pert at the University of York, UK. The code is used to simulate detailed atomic interactions and hydrodynamic expansion for high temperature laser produced plasmas. It treats single and multi-layer targets by dividing the material into 98 Lagrangian cells and evolving them according to the hybrid model of flow [25], producing a plasma profile for each time step. In the Hybrid model of flow, the Lagrangian cell matrix is orientated and evolved in the direction normal to the target surface, parallel to the direction of the driving laser. The evolving plasma is assumed to be isothermal in the direction parallel to the target so expansion in the transverse direction can be treated by assuming a self-similar Gaussian profile. The density and temperature information computed is used to perform detailed atomic calculations in order to determine the lasing on x-ray lines such as those seen in Ni-, Ne-, and F-like systems. The atomic calculations use a collisional-radiative model to give a full time-dependant ionisation balance for each Lagrangian cell. In addition to the terms considered in equation 2.5.7, collisional excitation and de-excitation are taken into account in order to determine level populations for an arbitrary number of atomic levels within each ionisation stage. The collisional excitation and ionisation rates are calculated via either a Gaunt factor approximation or an analytical fit to the collision strengths for a range of temperatures [45]. Three body recombination rates are deduced using the principle of detailed balance. Dielectronic recombination is approximated using Hagelsteins model [46] for specified ionisation stages (e.g. Ne-like) and uses an average atom model for all other ionisation stages. Radiative recombination is accounted for using Griem's method [47] and modified by a trapping factor [48]. An example calculation using EHYBRID, undertaken by the author, is shown in figure 2.1.

2.6.2 FLYCHK

FLYCHK is a population kinetics and spectral modeling code produced by the National Institute of Standards and Technology (NIST) in the US [44] and is accessible through a web interface. The code uses the LTE and CRSS approximations stated in section 2.5 (user specifies) to deduce the ionization and population distributions of a specified element at different temperatures and densities in zero dimension. The collisional and radiative rate equations are solved for steady state and time dependant cases (user specifies) using locally stored atomic data to provide the user with a range of spectroscopically observable output.

2.6.3 LPIC ++

LPIC++ is an electromagnetic, relativistic 1D3V (1 spatial, 3 velocity dimension) particle-in-cell (PIC) simulation code [49], written in C++, for the laser-plasma interaction created at the Max-Planck-Institut für Quantenoptik, Germany. The code solves Maxwell's equations for particles within a plasma in order to deduce electric and magnetic field strengths, particle velocities, particle and current densities, etc. The algorithms of Birdsall and Langdon [50], and Villasenor and Bunemann [51] are used. A relativistic Lorentz transformation is used to account for obliquely incident laser pulses and thus can be used to investigate hot electron and high harmonic production.

2.7 Conclusion and Summary

This chapter has outlined the theoretical principles behind the work presented in the subsequent chapters. It has defined terminology and demonstrated how an electromagnetic wave propagates and is absorbed within a laser produced plasma. Plasma opacity gives a frequency-dependant measure of the impenetrability of a medium to electromagnetic radiation and can be a difficult quantity to model computationally. For this reason, experiments using high powered lasers must be designed and carefully controlled in order to benchmark the numerous codes available and aid with solving the discrepancies observed. For these experiments to be successful, accurate methods of characterising the laser produced plasmas must be employed. The theory of plasma emission is well understood and by resolving plasma emission, either spectrally, spatially, or temporally, one can gain an accurate insight into the inner processes within plasma. This further understanding of plasma opacity can then be carried forward and used in other areas such as radiation diffusion models of stars or in energy generation using ICF.

3. Development of a Solid State Diode Array for Hard x-ray Detection

3.1 Introduction

This chapter outlines the development of a silicon inversion layer photodiode array for the detection of bremsstrahlung emission from a laser produced plasma. The aim is to determine the temperature of the hot electron component of the laser-plasma. Accurate measurement of the temperature of hot electron populations in laser-plasmas is needed as the hot electrons are responsible for K_α emission [24,52-54], for preheating the target ahead of the thermal conduction front [54-57] and for generating ion sources [57,58]. The diagnostic development described here is designed to be used with our Nd:YAG laser system in operation at the University of York. This table top, high repetition rate (5 Hz) laser system fires 0.5J energy in a 170ps pulse giving a focussed irradiance of $\sim 10^{14}$–10^{15} Wcm^{-2}.

The x-ray diagnostic consists of 4 silicon inversion layer photodiodes (XUV-100, OSI Optoelectronics) mounted on a plastic flange plate, using BNC feedthroughs, inside a vacuum chamber, directed towards the front side of targets. The diode array housing prevents light leakage and employs different filtering over each diode to investigate the hot electron energy spectrum in order to deduce the temperature. Electronics outside of the vacuum chamber amplify the diode signals and produce voltage pulses proportional to the amount of energy incident on each diode, which are in turn captured using an oscilloscope and can be read by a computer for analysis.

This chapter will introduce the theory behind the EUV enhanced silicon inversion layer photodiodes and the electronics built in situ that are used in this diagnostic. Section 3.4 will describe the diode array housing and the considerations undertaken to ensure lowest possible noise signals. Section 3.5 will discuss the filtering used in conjunction with the photodiodes and the method used to determine the hot electron temperature in the laser-plasma. Section 3.6 presents data taken during the testing phase of the diagnostic, including a comparison to a single photon counting charge coupled device (CCD). The chapter will conclude with proposals for future experimentation.

3.2 Photodiode theory

A p-n junction exists where there is a transition from a p-type material to an n-type material within a single crystal of semiconductor. A p-type semiconductor is a material which is doped in such a way to have an excess of positively charged holes in its equilibrium state and an n-type semiconductor is doped to have an excess of free electrons at equilibrium. When a p-n junction is formed, the majority carriers (holes in p-type region, electrons in n-type region) diffuse into the opposite region due to the difference in Fermi levels (chemical potentials) between the two regions. This recombination of electrons and holes continues until a potential (known as the built-in potential) is established across the junction which inhibits the diffusion currents [59]. The built-in potential is formed by the regions either side of the junction becoming charged. These charged areas extend a short distance on either side of the junction (see figure 3.1) and form the depletion layer of the semiconductor. When an incident photon has sufficient energy to excite an electron from the valence band of the semiconductor to the conduction band, an electron-hole pair is created. If this electron-hole pair is generated within the depletion layer of the p-n junction then the built-in potential separates the hole and electron generating a photocurrent proportional to the incident energy of the photon. In silicon, one electron-hole pair is created for every 3.63 eV of incident energy for photons of energy >30eV [60].

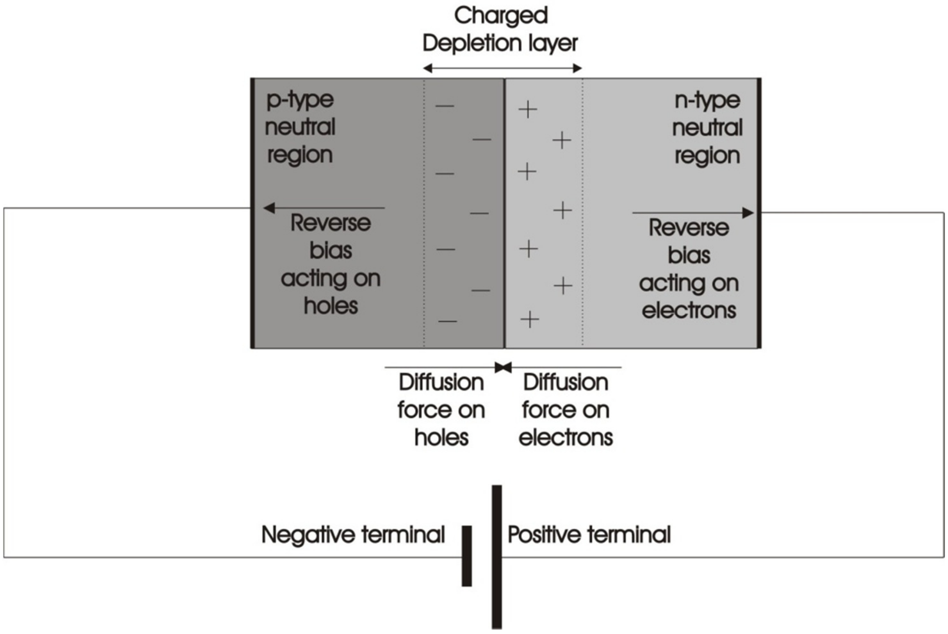

Figure 3.1 p-n junction diode cross-section operating under reverse bias.

Photodiodes are operated in either a photovoltaic or photoconductive mode. The photovoltaic mode has no bias across the diode and as incident light generates electron-hole pairs, the voltage increases across the p-n junction. This increased voltage causes a dark current to flow. The photoconductive mode utilises a reverse bias across the diode and is primarily used for the detection of light as the photocurrent produced is linearly proportional to the incident luminous flux [59]. To reverse bias a photodiode, the negative terminal of the voltage source (e.g. battery) is connected to the p-type side of the p-n junction and the positive terminal is connected to the n-type side (figure 3.1). By introducing this additional voltage across the diode, the holes and electrons in the p-type and n-type material respectively are pulled away from the depletion layer. This in turn increases the width of the depletion layer and prohibits current from flowing when light is not incident due to the increase in potential across the p-n junction. Increasing the voltage across the diode increases the width of the depletion layer up until a critical value (breakdown voltage) where the depletion region breaks down and current can once again flow through the p-n junction [59].

In order to fully utilise a p-n junction as a photodiode, careful attention must be given to the design of the diode itself. For example, if light cannot reach the depletion region then no signal will be detected. Figure 3.2 shows a cross section of a silicon inversion layer photodiode similar to those used in the diagnostic discussed in this chapter. Electron-hole pairs are created as the incident radiation penetrates through to the depletion layer and excites electrons from the valence band to the conduction band of the semiconductor. As the diagnostic discussed in this chapter examines the hard x-ray region of the spectrum, the depletion layer must be large enough so as a significant number of photons interact within the depletion region.

As photon energy increases, silicon becomes more transmissive. However, in some regions in the UV, silicon is highly effective at absorbing the radiation as can be seen by the transmission plot for 1μm thickness of silicon in figure 3.3. This means UV radiation at these wavelengths is absorbed very close to the surface of the silicon and does not penetrate through to the depletion layer and subsequently is not detected. This effect is counteracted through the use of an induced inversion layer which inhibits surface recombination [61]. Using a thermally grown silicon oxide (SiO_2) on the surface of p-type silicon, a surface state charge is introduced, situated within the oxide [61]. At the interface between the SiO_2 and Si, a spatially shallow junction (of nm thickness) is created and is sufficient to collect any photo generated carriers near the surface [61]. This junction is due to a thin layer of electrons forming an n-type inversion layer due to the charge contained within the oxide at the surface. This technique increases the sensitivity of the diodes in the spectral regions where Si absorption is high.

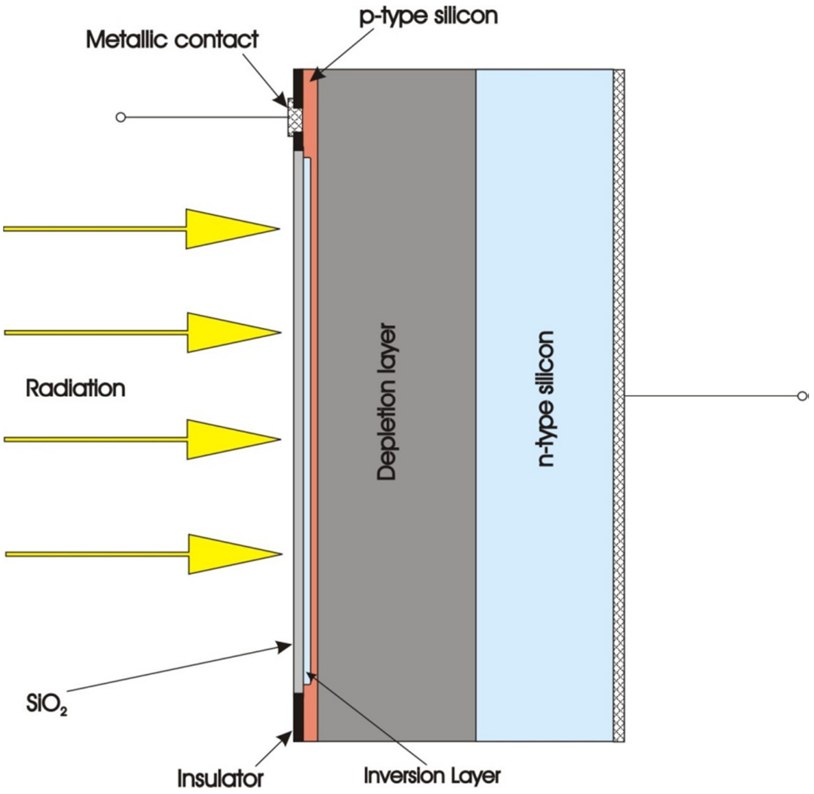

Figure 3.2 Cross-section of a silicon inversion layer photodiode

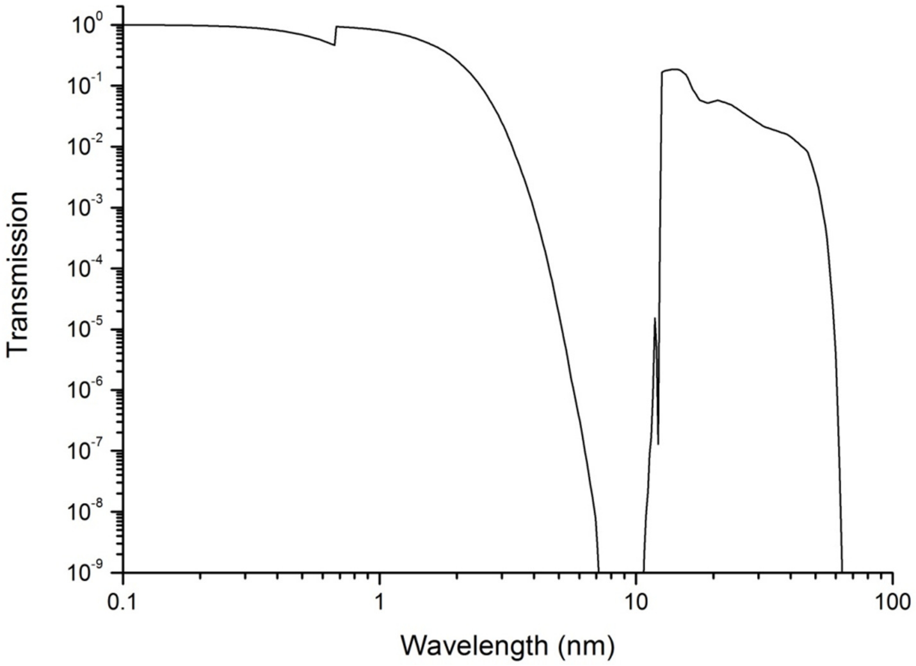

Figure 3.3 Transmission plot for 1µm thickness of silicon highlighting the efficient absorption of silicon for photons of wavelength 6 - 10nm and above 60nm [62].

We used an XUV-100 diode (manufactured by OSI Optoelectronics) for the diagnostic described in this chapter. This diode has a depletion depth of around 5mm [60]. With such a large depletion region, ~ 100% of photons with energies up to 18keV are absorbed [62], above which photons begin to pass through the silicon layer with a fraction being absorbed. This type of diode has very high stable quantum efficiencies, with one electron-hole pair produced for every 3.63eV of incident radiation for photon energies above ~30eV [60].

3.3 Reverse Biasing and Charge Sensitive Pre-amplifier

As mentioned in the previous section, photodiodes are normally operated under reverse bias for radiation detection and require some form of current amplification in order to detect low light or x-ray signals. For these reasons, electrical circuitry has been designed to collect, temporally integrate, and amplify the diode charge pulse signals before providing output to an oscilloscope for measurement. The circuit used for each diode is shown in figure 3.4 and is split up into 7 different components. Firstly, the reverse bias, shown as component 1 in figure 3.4, consists of a DC battery supply (in order to ensure a low noise level) of 3.8V, chosen taking into account the breakdown voltage of the photodiode of 5V. Component 2 is a low pass RC filter which is used to remove high frequency noise from the bias source. This component is predominantly in place in case an AC power supply is to be used in place of the batteries. The third component is the detector bias resistor and provides AC coupling of the detector to the bias supply. This is opposed to DC coupling which involves connecting the detector to the bias directly, giving rise to an offset of the preamplifier output signal. The detector bias resistor works in conjunction with the coupling capacitor (component 4). The feedback capacitor (component 5), the feedback resistor (component 6) and the operational amplifier (component 7) form a charge sensitive pre-amplifier and all work together to amplify the signal generated by the photodiode. Radiation striking the diode produces charge pulses which raise the input-end potential of the charge amplifier causing a reverse polarity potential to generate at the output end [63]. As the operational amplifier has a very large open loop gain (~700,000), this reverse polarity potential works through the feedback loop reducing the input-end potential to zero, meaning the charges produced are integrated into the feedback capacitor. The integrated charge is then output as a voltage pulse, V_{OUT}, with an opposite polarity to the input voltage induced by the charge pulse from the diodes. As the feedback resistor is connected in parallel to the feedback capacitor, the capacitor slowly discharges, meaning the output voltage pulse has a decay constant of $\tau = C_f R_f$, where C_f and R_f are the feedback capacitance and resistance respectively. For the set-up demonstrated in figure 3.4, the decay constant τ = 100µs.

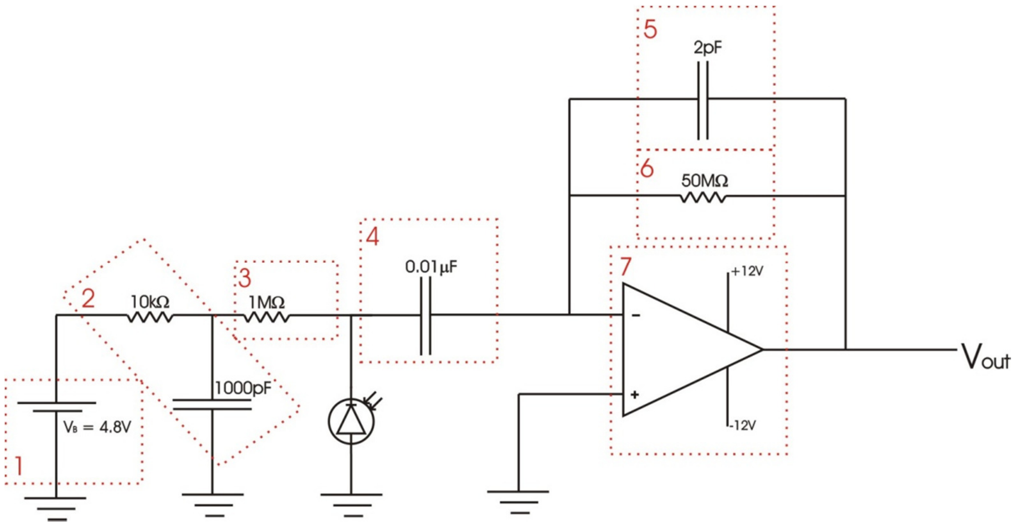

Figure 3.4: Pre-amplifier and reverse bias circuit for a silicon inversion layer photodiode, numbered boxes are referred to in the text.

The gain produced by the circuitry shown in figure 3.4 comes from using the feedback capacitance C_f in the circuitry to produce the output voltage pulse as opposed to the in-built capacitance of the diode, C_d. The voltage across a capacitor is determined by, $V=Q/C$, where Q is the charge and C is the capacitance. The XUV-100 diodes used here have an internal capacitance of typically 6nF [60], and as this is being substituted by a

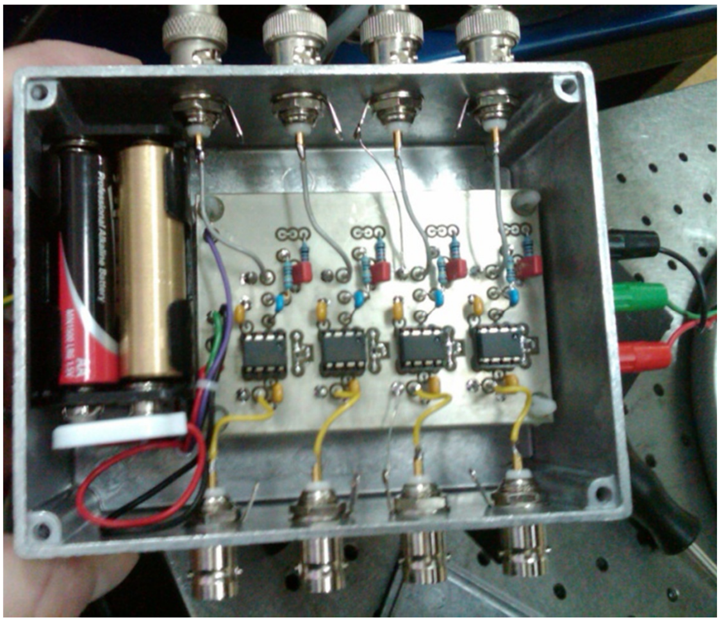

Figure 3.5 Charge sensitive pre-amplifier and reverse bias for x-ray diode array with BNC input/output and separate power supply for op-amps. Batteries of size AA shown on the left hand side of the box illustrate the scale.

feedback capacitance of 2pF, the circuit will give a gain of ~3000. A useful parameter to consider in this case is the sensitivity, *S*, of the whole system, taking into account the charge released by the detector knowing that one electron-hole pair is produced for every 3.63eV of incident energy. The output voltage V_{OUT} can be calculated by using equation 3.3.1,

$$V_{OUT} = \frac{Q}{C_f} = \frac{Ee}{C_f \delta} = SE \tag{3.3.1}$$

where *E* is the incident energy on the diode (in eV) and δ= 3.63eV is the amount of energy required to produce an electron-hole pair. For the components used (values shown in figure 3.4),

$$S = \frac{V_{OUT}}{E} = \frac{e}{C_f \delta} = 0.02 mV/keV, \tag{3.3.2}$$

meaning for every keV of incident x-ray energy a 0.02mV output voltage signal is produced.

The circuitry shown in figure 3.4 has been duplicated for each of the four diodes (using a common bias for all channels) and placed in a metal box to minimise noise (figure 3.5). As is seen in figure 3.5, the charge sensitive pre-amplifier has BNC input/output to allow for coaxial cables to connect the box to the diodes and oscilloscope.

3.4 Diode array housing and isolation

One of the main issues arising when using a diagnostic that involves amplification of a low level signal is that of electrical noise. The largest source of noise for the diode system was found to be voltage pulses originating from the flash lamps of the laser charging/discharging acting on the diodes through a ground loop. The laser electronics were at first found to produce a signal in the diodes which is then amplified before reaching the oscilloscope as is seen in figure 3.6, dominating over any other signal present. This source of noise was removed by completely isolating the diode array from anything grounded, including the vacuum chamber. Careful consideration had to be given to the design of the x-ray diode (XRD) housing. The diodes are mounted on a plastic (Tufset – Rigid Polyurethane) flange with 6 BNC vacuum compatible feedthroughs. By mounting the diodes on a plastic flange, not only are ground loops prevented, but also capacitive coupling between the coaxial cables, by ensuring the diodes are isolated from one another. An aluminium cylinder surrounds all diodes and an aluminium plate, on the front, held by a post through the centre is used to cover the diodes and to hold filters in place. The housing is designed to keep a 1mm separation between the diodes and the front plate so as not to complete the ground loop. Aluminium piping is also used to restrict the solid angle of the diodes to provide direct line of sight to the target only so that the diodes do not act as antennas receiving radio frequency noise. The housing and diodes are shown in figure 3.7.

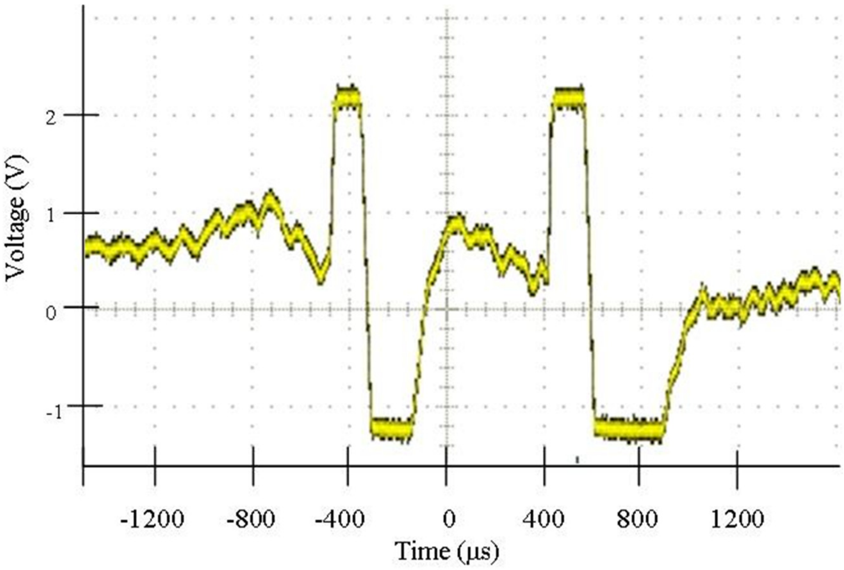

Figure 3.6 Signal (saturated) due to voltage pulses caused by the laser flash lamps, as seen on the oscilloscope after amplification. The vertical axis is voltage with a scale of 0.2V per division and the horizontal axis is time with a scale of 80μs per division.

3.5 Hot Electron Temperature

In order to deduce the temperature of the hot electron component within the plasma produced by a 0.5J, 170ps laser focussed to 10^{15} Wcm^{-2}, the x-ray diodes (XRDs) are used to measure bremsstrahlung emission from the plasma with photon energies above 5keV. Each of the four XRDs is covered with a different filter to restrict the spectral region which is recorded. The measurements in different spectral regions allows for the slope of the Maxwellian distribution to be deduced giving the temperature as described by equation 2.3.1 in Chapter 2. As the XRD are recording the emission of photons above 5keV, there is a negligible contribution from the thermal temperature plasma to the readings.

Figure 3.7 X-ray diodes (left) mounted on plastic (Tufset) flange with BNC feedthroughs and the covering aluminium housing (right). Each diode has an active area of 12mm.

Photon energy dependant transmission of solid materials can easily be calculated using Beer's Law, given by equation 2.2.1 in Chapter 2, with absorption coefficient data readily available online [62]. The four filters chosen for this diagnostic consist of different combinations of metal foils and plastic and have been specifically chosen to optimise the process of hot electron temperature determination in the temperature regime between 5 to 15 keV. The filters chosen are shown in table 3.1.

Filter Number	Filter Components
Channel 1	200µm Polyimide and 15µm Ni
Channel 2	200µm Polyimide and 30µm Sn
Channel 3	15µm Ag and 10µm Al
Channel 4	50µm Cu and 100µm Ti

Table 3.1 Filter components used for XRD diagnostic, optimised for hot electron temperatures between 5 and 15keV

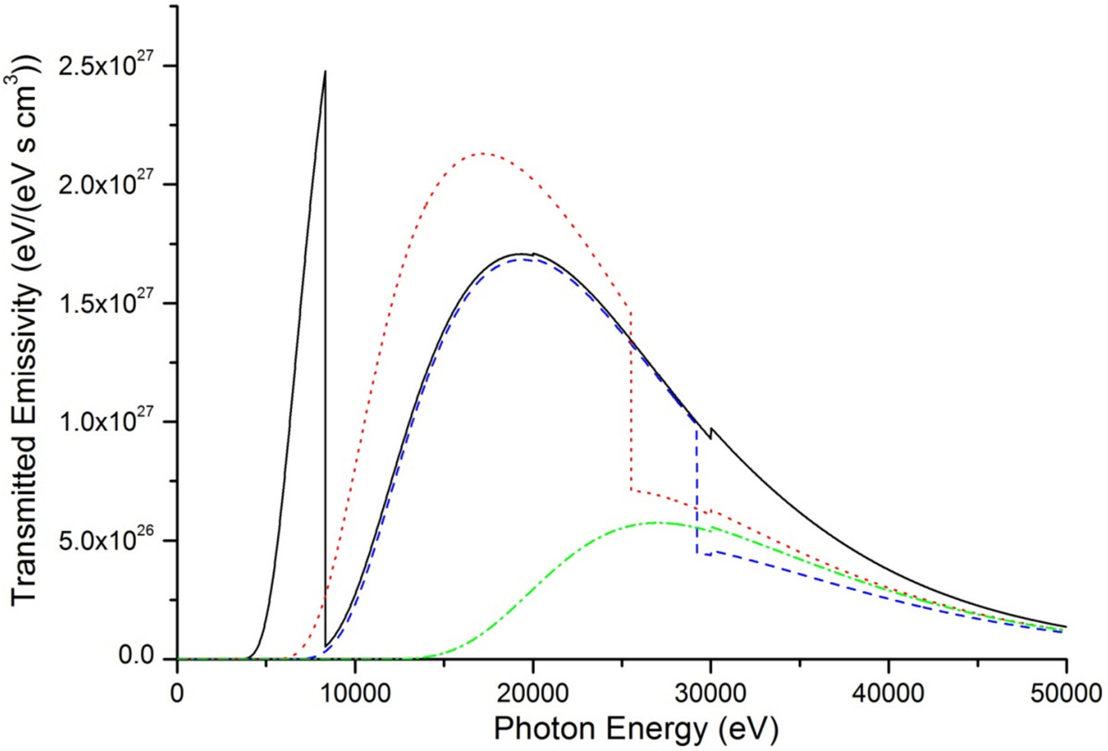

Figure 3.8 Transmitted emissivity due to bremsstrahlung from a laser produced plasma with a hot electron temperature of 10keV, assuming a plasma volume of 8.8x10^{-10} cm^{-3} and a time of emission of 170ps. Filters 1, 2, 3, and 4 are shown by the black solid line, blue dashed line, red dotted line and the green dash-dot line respectively. The transmission of the 5mm depletion layer of the photodiode is taken into account.

The transmission of each filter (including the transmission of the 5mm depletion depth of the diode) can be combined with equation 2.3.1 to give a transmitted emissivity plot as a function of photon energy incident on the XRDs (see figure 3.8). Filter number 2 has been carefully selected to match the high energy component of filter number 1 as is seen in figure 3.8. This is to allow the signal received by the diode behind filter 2 to compensate the diode behind filter 1 by removing the high energy component, thus giving a clear measurement of the emission of 5 - 8keV photons. Using this compensation technique gives a measurement of the bremsstrahlung emission in three distinct spectral regions as is shown in figure 3.9.

One of the main sources of error in determining the hot electron temperature using absolute numbers of photons comes from the estimation of the plasma size and the plasma time of emission. This can be avoided by calculating ratios between the different diode signals, as the plasma volume and emission time terms cancel out, assuming all emission originates from the same volume of plasma over the same time period for a single shot. The variation of the diode signal ratios as a function of hot electron temperature is shown in figure 3.10. The most accurate method for doing this uses the ratios between channels 3 and 4 (*R1*) and between the compensated signal from channel 1 and channel 4 (*R2*). Assuming a 10% error on the oscilloscope reading shows that the hot electron temperature can be measured to an accuracy of within 0.5keV. Hot electron temperatures can be measured on a shot to shot basis and calculated quickly using figure 3.10.

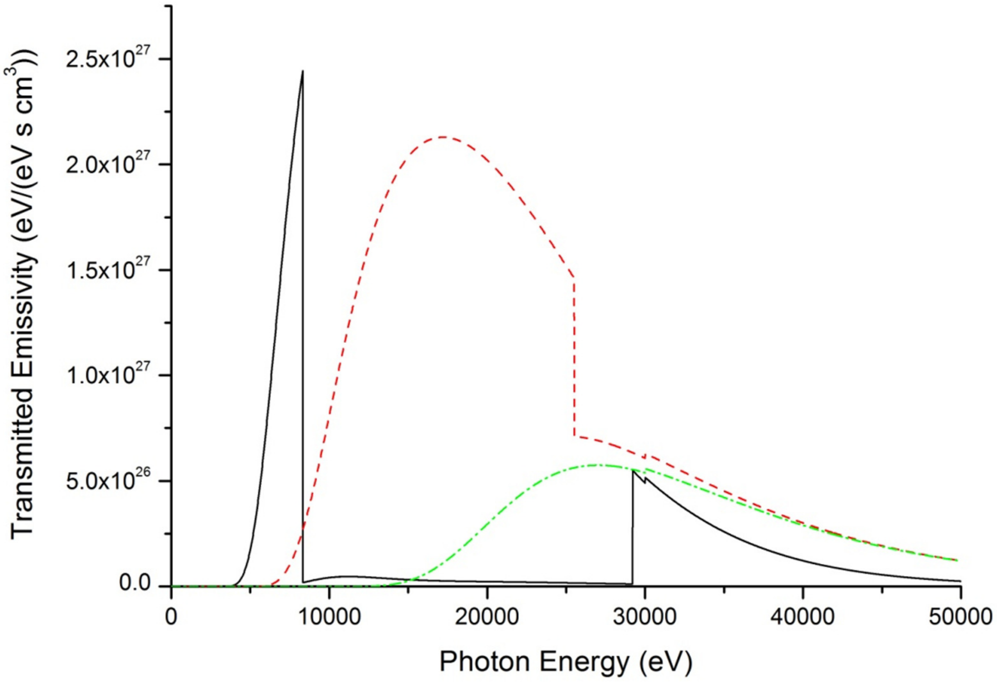

Figure 3.9 Transmitted emissivity plot showing a compensated signal for channel 1. There are 3 signal peaks in distinct regions of the hot electron spectrum. Plasma parameters and symbols are the same as in figure 3.8.

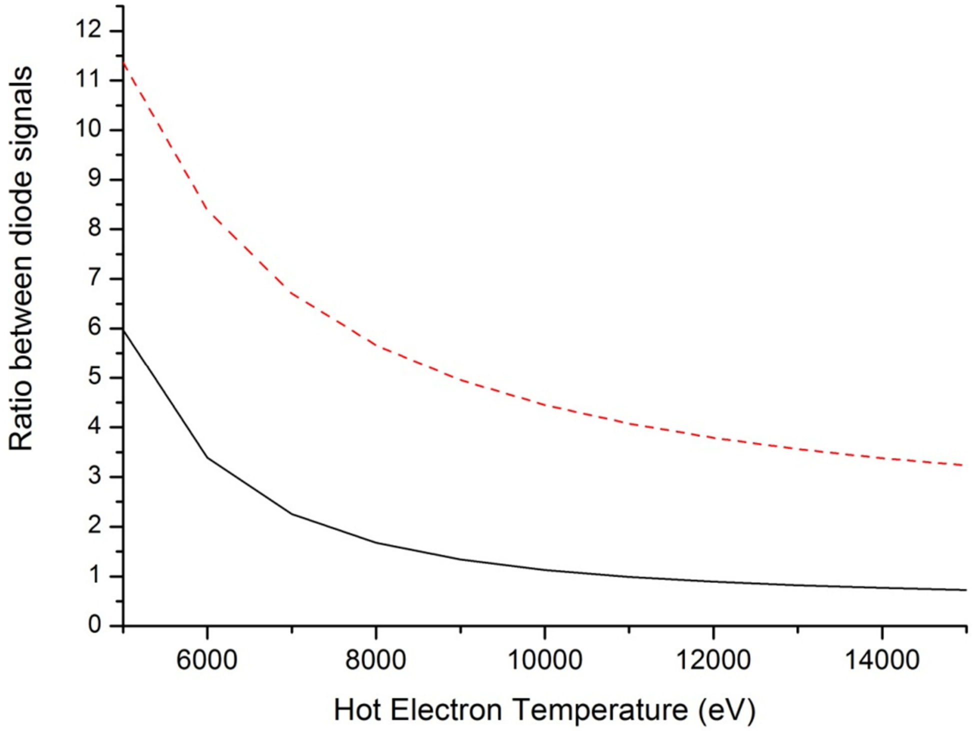

Figure 3.10 Variation of diode signal ratios as a function of hot electron temperature. Red dashed line is the ratio *R1* = (Channel 3)/(Channel 4) and black solid line is the ratio *R2* = (Compensated Channel 1)/(Channel 4)

3.6 Diode Array Testing

The XRD array described above has been used to measure the hot electron temperature produced by a 0.5J, 170ps, Nd:YAG (EKSPLA SL-312P) laser focussed with an f/4 lens on to solid aluminium targets. The maximum on target intensity achievable with this laser is ~1x10^{15} Wcm^{-2}, as we found best focussing to a spot size of 15µm diameter, approximately four times the diffraction limit. The scaling law given by equation 2.1.10 predicts a hot electron temperature of 5 – 10keV is produced by a laser with an on target intensity ranging from 10^{14} – 10^{15} Wcm^{-2}.

3.6.1 Experimental Set-up

The 1.064μm Nd:YAG laser is passed through a Faraday isolator before focussing by an f/4 positive 'bestform' lens (CVI Melles Griot – BFPL-25.4-100.0-UV) onto an aluminium disk at an angle of ~30° to the target normal (figure 3.11). A bestform lens minimises coma, spherical aberration and astigmatism, allowing the laser to be focussed to the smallest focal spot size possible with the laser pulse. The lens has a low-loss, high damage threshold anti-reflective coating. The 2mm thick aluminium target disk is mounted on a rotational stage which can be triggered manually or automatically using the laser trigger and an arbitrary time delay. As is shown in figure 3.11, a leakage beam is taken from the fourth mirror (point x) along path A and sent to a photodiode (path B), calibrated using a calorimeter inside the target chamber, to calculate the on target laser energy per shot. Back reflected infra-red light from the target travels back along path A in the opposite direction to the incident laser beam, where the Faraday isolator prevents back scattered light from re-entering the laser oscillator and causing damage. The Faraday isolator utilises the magneto-optic Faraday effect to rotate the linear polarisation of the laser as it propagates through the medium. By combining this effect with an input and output polariser, laser light can only pass in one direction (towards the target), thus preventing back-scattered light from re-entering the laser oscillator.

Before the back-scattered laser light enters the Faraday isolator, a second leakage beam is established and focussed onto a CCD (Basler Scout with Sony ICX 267 Sensor) as shown by optical path C in figure 3.11. Lens 2 shown on optical path C is set at best focus using direct reflection of the laser beam by placing a mirror (M1 in figure 3.11) on the laser side of lens 1 and focussing the back reflection onto the CCD. Once lens 2 is set at best focus, the mirror M1 is removed, giving the CCD on path C a line of sight to the target. When the focussed laser is incident upon the target it is diffusely scattered over 2π steradians and as a result, this set-up can be thought of as a collimation system for a point source situated at the focal point of lens 1. Only rays which pass through the focal point of lens 1 will have an image distance tending to infinity and will be collimated by lens 1 and thus follow approximately parallel beam paths back along path A to C. Any rays not passing through the focal point will not be collimated by lens 1 and thus will propagate out of the path A to C and so will not be detected by the CCD. As lens 1 approaches best focus, the spot size becomes smaller and moves closer to the focal position of the lens. More of the diffusely reflected laser light passes through the focal point of lens 1, meaning more light reaches the CCD. When lens 1 is defocused, the spot size moves away from the focal point and becomes larger. As a result, less light passes through the focal point of lens 1 and thus less light reaches the CCD. This effect produces a spot seen on the CCD which varies in intensity as lens 1 is moved in and out of focus as shown in figure 3.12.

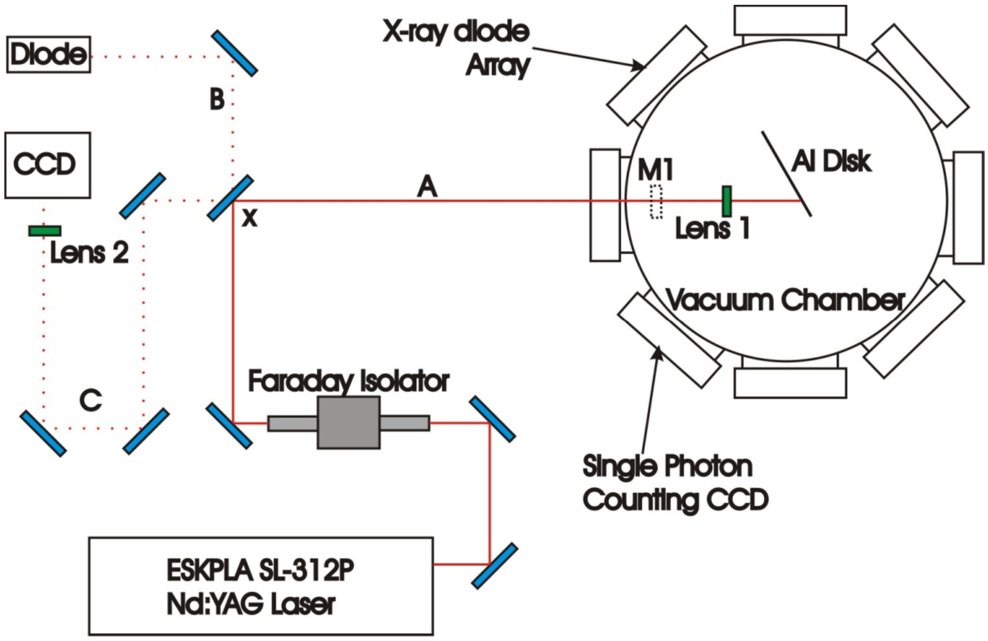

Figure 3.11 Experimental laser set-up used for the XRD array testing. The green components are lenses and the blue components are infra-red mirrors. The solid red line represents the main laser optical path (path A), the dotted lines are leakage beams for energy calibration (path B) and retro-focussing (path C). The dotted component M1 is a removable mirror used to set-up the retro-focussing system.

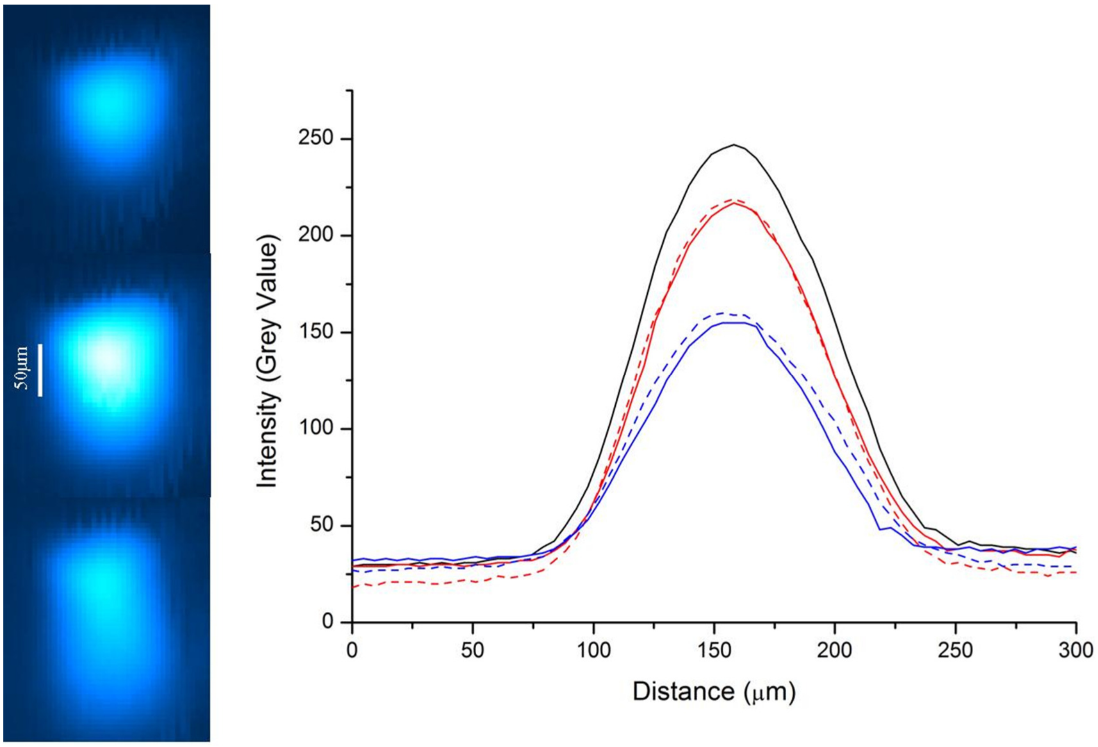

Figure 3.12 False colour images from retro-focussing CCD (left) showing best focus (middle) and a lateral movement of lens 1 of +400μm and -400μm (top and bottom respectively), a negative movement brings the lens closer to the target. Plots of intensity for various lens positions (right), the black line is at best focus, red lines are 200μm movements and blue are 400μm movements, dashed are negative movements (target closer to lens than best focus) and solid lines are positive movements (target further from lens than best focus).

The x-ray diode array is positioned facing the front side of the target as shown in figure 3.11. Short co-axial cables are then used to connect the BNC feedthroughs to the circuitry described in section 3.3. This part of the system is very sensitive to noise as any electronic fluctuations picked up at this stage are amplified by the circuitry along with the diode signal. For this reason short co-axial cables are used and the diodes are isolated from one another as capacitive coupling between the co-axial cables can produce such fluctuations. After amplification, the signals are sent to oscilloscopes (Tektronix TDS-220) for capture and processing.

3.6.2 Comparison with Single Photon Counting

In order to compare the effectiveness of the diode array in calculating hot electron temperature, a single photon counting charge coupled device (CCD) was set-up as shown in figure 3.11 and calibrated using a ^{55}Fe radioactive source. Single photon counting is a technique which uses moderate filtering over a charge-coupled detector in order to attenuate the signal to reduce the probability of two photons striking the same pixel. As the charge produced within each pixel of the silicon based device is proportional to the incident photon energy, an energy spectrum can be produced through analysis of the image recorded [64-66].

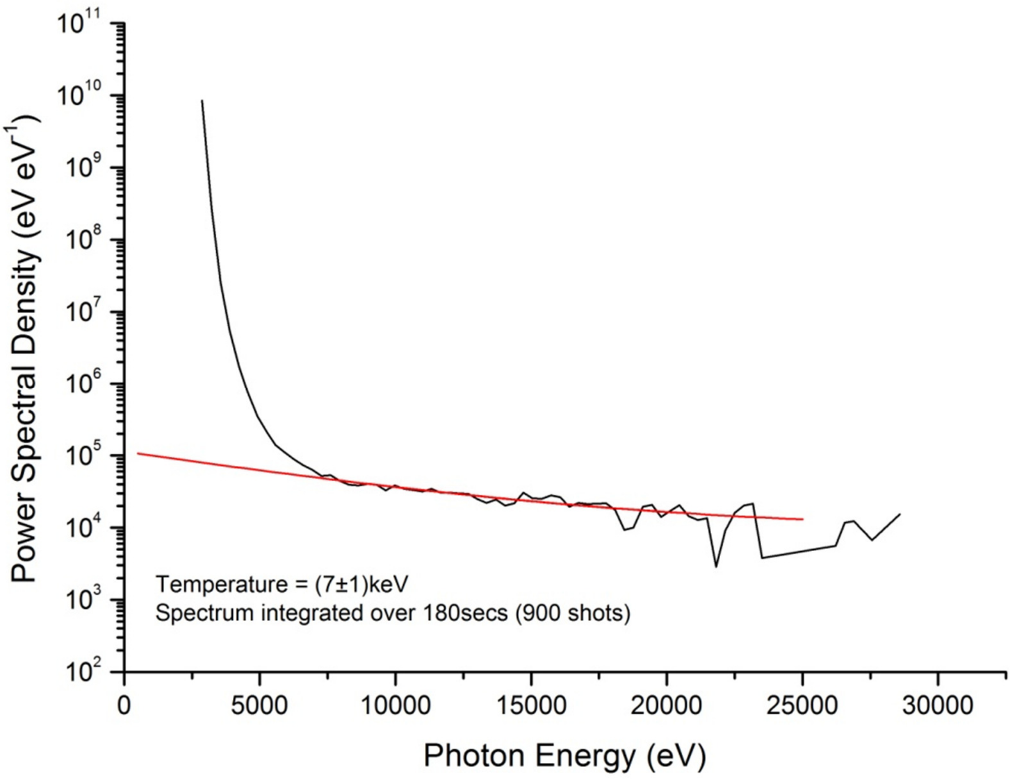

Figure 3.13 Single photon counting spectrum integrated over 900 laser shots on a 2mm thick Al disk. Filtering covering the CCD was 56μm aluminium and 100 μm polyimide. The disk is rotated once a second to provide a fresh surface every 5 shots.

The on target laser intensity in this experiment is approximately 10^{15} W cm^{-2}, which is a few orders of magnitude less than the experimental facilities normally used in conjunction with this technique. As a result, the plasma temperatures achieved are cooler, resulting in less high energy photon emission. Due to the high level of thermal emission in comparison to suprathermal emission, heavy filtering of 56μm Al and 100μm Polyimide is required to remove the lower energy photons and consequently a large number of laser shots needed to be integrated to achieve a signal level from which a bremsstrahlung spectrum could be produced and a hot electron temperature determined. The resulting single photon counting spectrum in this work was integrated over 900 shots (3 minutes at 5Hz) and predicted an average temperature over the shots of 7 ± 1 keV as shown in figure 3.13. The aluminium target disk was rotated once a second to provide a fresh target surface every 5 shots.

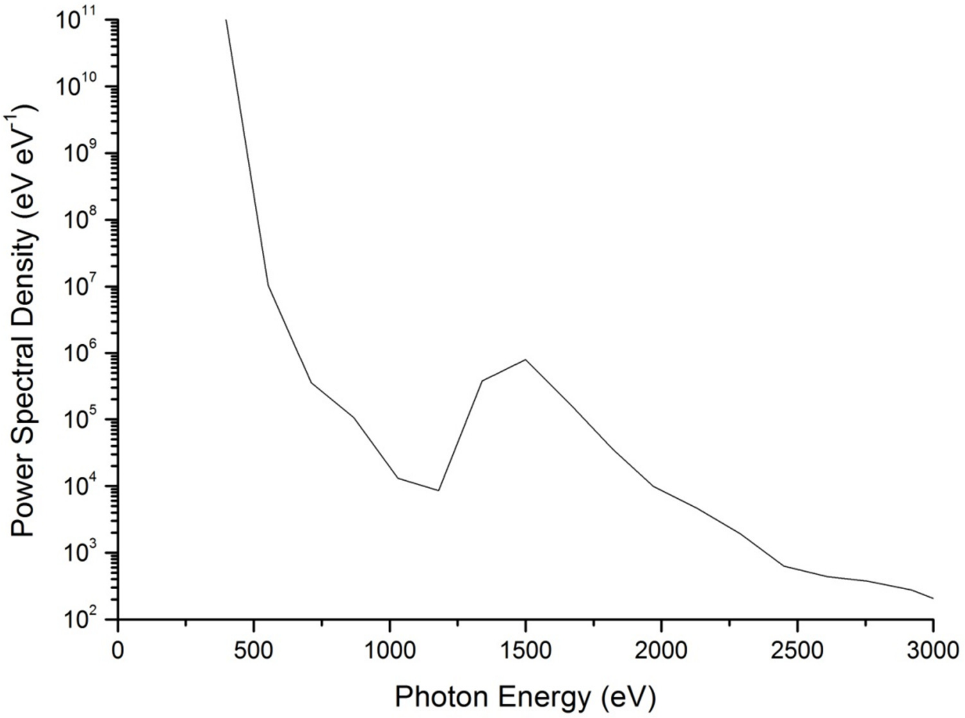

Figure 3.14 Single photon counting spectrum showing Al emission lines at 1.5 keV, integrated over 5 shots on a 2mm thick Al disk. The filtering used was 14μm Al and 2μm aluminised mylar.

During the testing phase of the single photon counting diagnostic when much lighter filtering (14μm aluminium and 2μm aluminised mylar) was being used, an aluminium emission peak at 1.5keV was observed in the produced spectrum, integrated over 5 shots (figure 3.14). This peak is due to aluminium K_α emission originating from the interaction of the hot electrons with the solid target. Al He-like lines would have been present also, however, the energy of these transitions are above the Al K-edge and thus would have been heavily filtered by the 14μm of aluminium used as a filter for the CCD. The resolution of the technique does not allow for absolute numbers of K_α photons to be determined. Figure 3.14 demonstrates the requirement for heavy filtering as the power spectral density for thermal emission ($h\nu <$ 5keV) is similar to that shown in figure 3.13, integrated over 900 shots. This represents the highest level of exposure for the CCD before the analysis can no longer distinguish between individual photons.

For comparison to the CCD single photon counting the x-ray diode array signals were averaged over 128 shots (25.6 seconds at 5Hz) rather than being utilised for temperature measurement of single shots. Averaging over 128 shots, the average temperature of the plasma over a large number of shots can be more readily compared to the single photon counting result averaged over 900 shots. The Tektronix TDS-2000 oscilloscope was used and allowed for the voltage signals to be averaged over a maximum of 128 shots. The signals obtained are shown in figure 3.15 and predict an average temperature of 7.5 ± 0.5 keV in agreement with the single photon counting diagnostic. The comparison between the single photon counting diagnostic and the x-ray diode array results is viable due to the high reproducibility of the laser system. Figure 3.16 demonstrates the variation of on target laser energy, where the variation in laser energy between shots is within 10%.

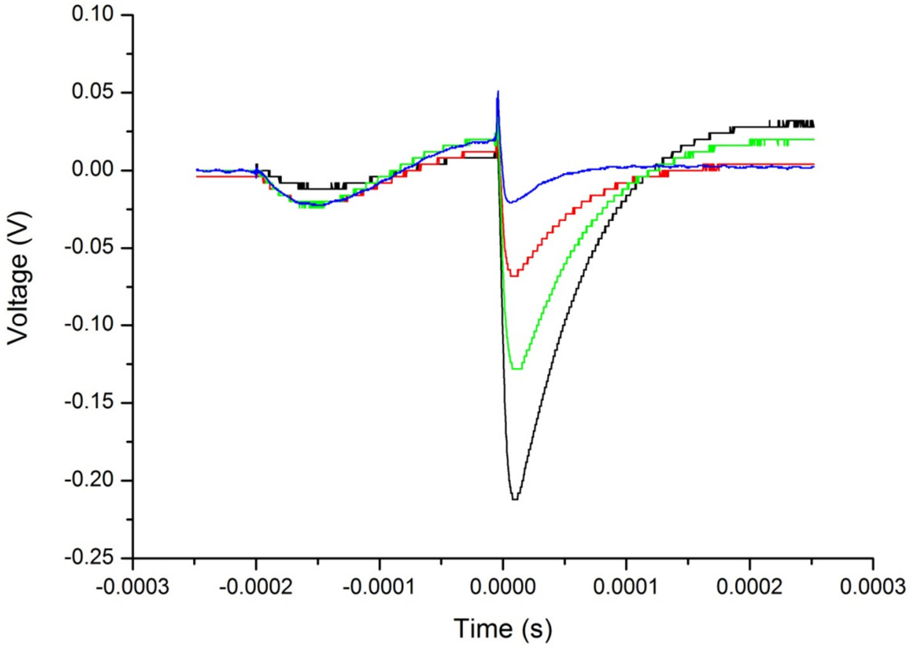

Figure 3.15 X-ray diode signals averaged over 128 shots giving an average temperature of 7.5 ± 0.5 keV. The filter combinations (table 3.1) shown are channel 1 (black), channel 2 (red), channel 3 (green), and channel 4 (blue).

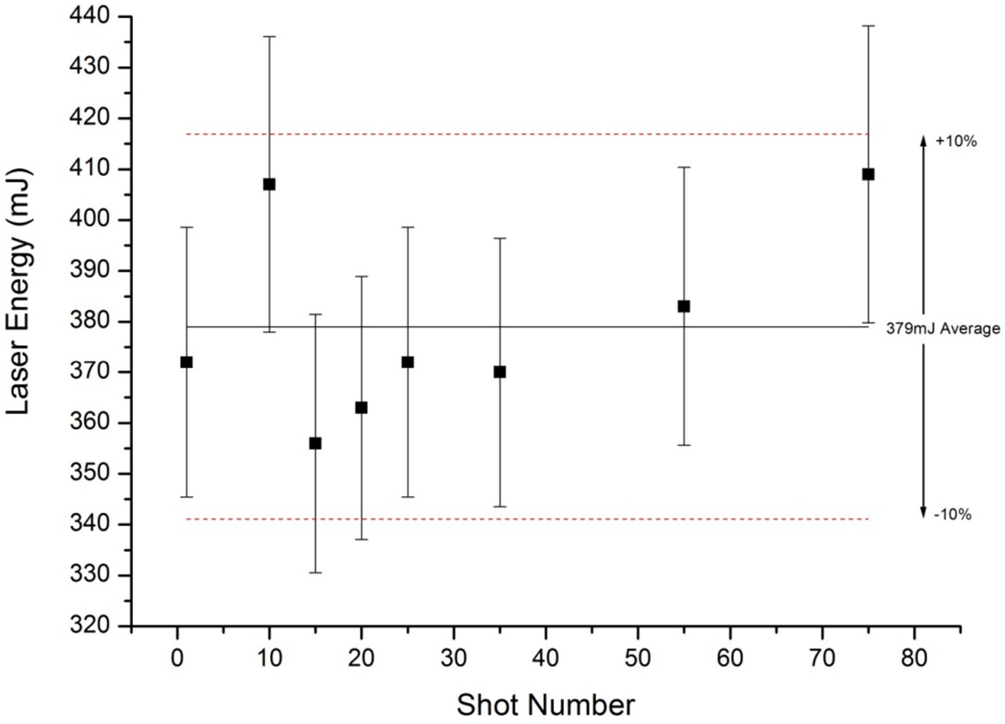

Figure 3.16 Variation of on target laser energy. The average energy on target seen is 379mJ and the variation shot to shot is within 10%.

A feature of the diode signals is the MHz frequency peak that appears before the decay curve of the signal. Figure 3.17 shows the diode output on a shorter timescale and shows the signal from two different diodes for the same laser shot. The signal itself follows the same trend on both diodes with different peak voltages and is thought to be a feature of the response of the electronics. As the voltage produced by the diode is read from a base line to the peak of the decay curve and that the integrated noise signal shown in figure 3.17 is approximately zero, this noise signal has a negligible effect on the overall result.

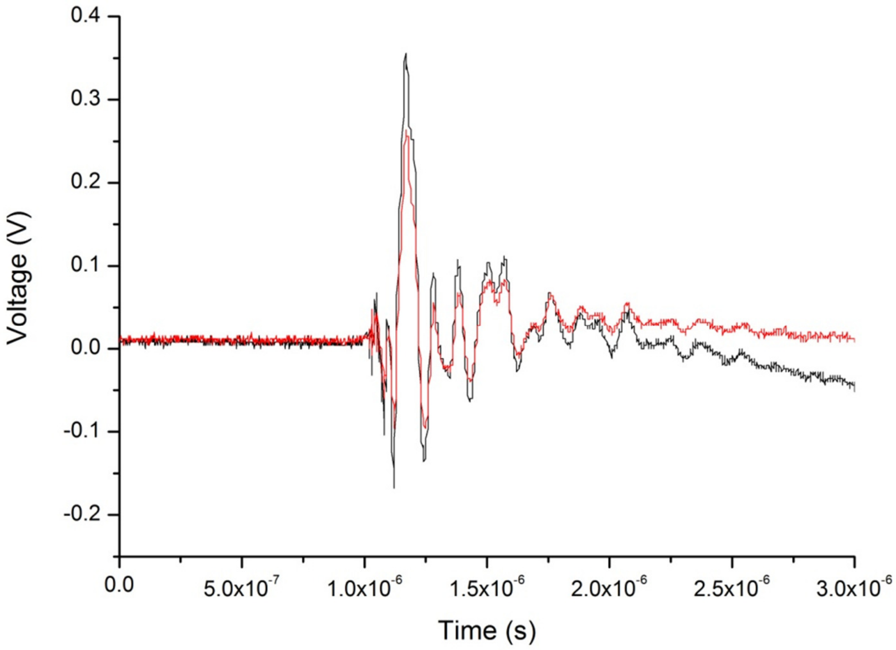

Figure 3.17 Noise signal from two separate diodes from the same laser shot, the signal has a 10 MHz frequency and the integrated signal is approximately zero.

3.6.3 X-ray diode results

The main disadvantage of using the single photon counting CCD to determine the hot electron temperature of plasmas produced by lasers of intensity ~ 10^{15} W cm^{-2} is the large number of shots required to obtain an analysable spectrum. This method cannot be operated in a single shot mode for this laser intensity regime and the analysis is difficult to do in real time due to image processing requirements. The x-ray diodes offer a method to deduce the hot electron temperature quickly and on a shot by shot basis. The diodes have been specifically designed to detect and amplify very low radiation levels in different regions of the spectrum and by comparing the 4 signals, a suprathermal temperature can be determined quickly and accurately, and can be automated using a program to read off the oscilloscope traces and perform real time analysis.

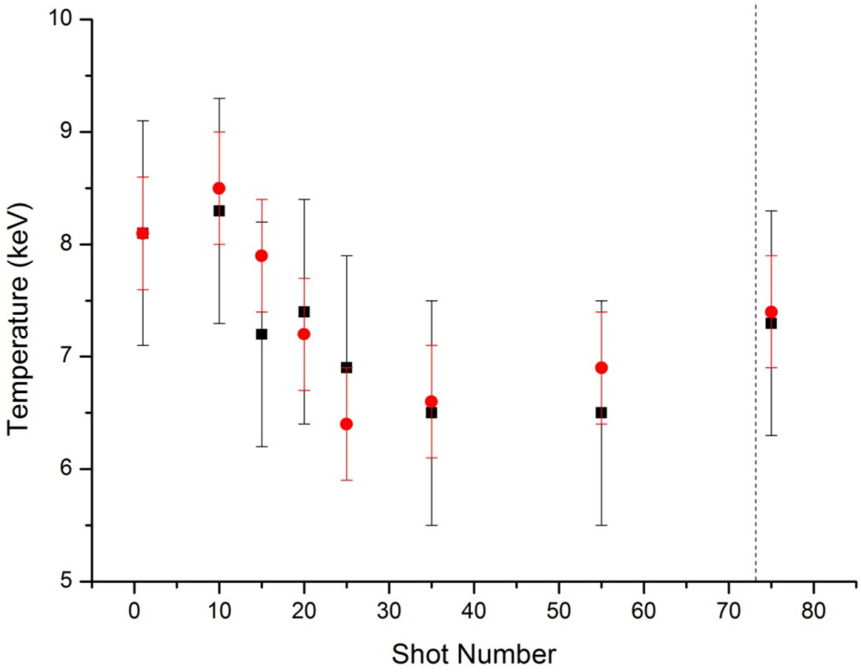

Figure 3.18 Comparison between hot electron temperature calculations as the laser burns through the target. The red points are experimental data calculated using *R1* and the black points use *R2* (see figure 3.10). The vertical dashed line represents the shot number at which the laser has burnt through the 2mm thick aluminium target.

As is discussed in section 3.5, two different ratios between the channels are used to determine the hot electron temperature. A comparison of the calculated temperatures from each ratio can be used as an additional test as to the quality of the result obtained. Figure 3.18 shows a series of measurements taken, where the laser was repeatedly fired on to the same area of the target disk, until the laser burnt through the 2mm thick aluminium. Figure 3.18 shows, firstly, a good agreement between the calculated temperatures from the two ratios and secondly, the temperature decreases as the laser burns through the target. As the laser is not re-focussed after each shot, the on target intensity decreases as the focal position of the lens is progressively further away from the target surface due to the ablation of the target. This lower on target intensity causes a reduction in the hot electron temperature. The reduction in hot electron temperature observed as the laser becomes de-focussed is not as would be expected using the scaling laws in section 2.1.3. One would expect to see a decrease in hot electron temperature until the electron energy was low enough to effectively thermalise within the thermal plasma making it indistinguishable from the thermal population of electrons. This is most likely not observed due to the combination of the de-focussed laser pulse interacting with the sloped walls of the conical cavity, which has been shown to increase hot electron

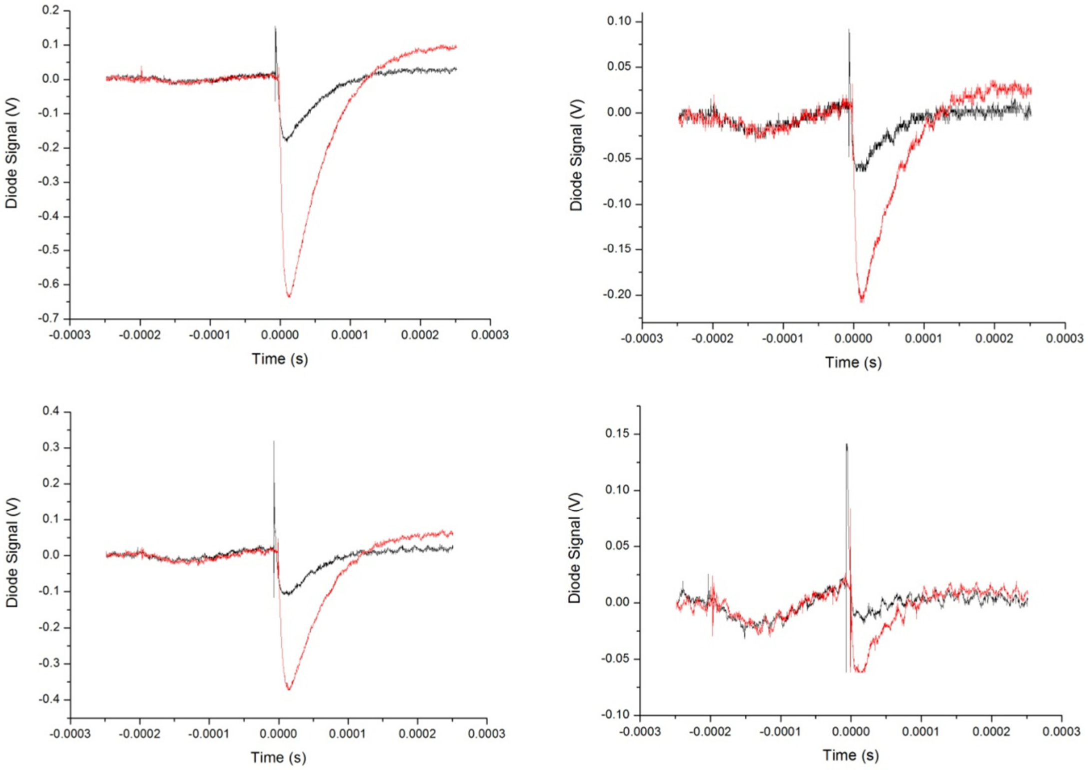

Figure 3.19 Change in diode signal when the laser burns through the 2mm aluminium target. The black lines are the signals on each of the four channels (numbered 1 to 4 as in table 3.1 reading left to right) from the first (in focus) shot and the red lines are the diode signals on the shot after burn through.

generation [67], and thermal self-focusing of the laser within the laser produced plasma [68]. This combination results in a smaller reduction in hot electron temperature as the laser de-focuses. This trend is only seen to continue until the point at which the laser burns through the target where the temperature increases to ~ 7 keV, and remains approximately constant and the individual diode signals rapidly increase by a factor of ~ 4 (see figure 3.19). This increase in signal is very sudden (figure 3.20) and occurs on the shot where visible emission is first seen on the rear side of the target indicating the laser has burnt through the target. As the relative signals between the diodes remain the same (similar temperature), this rapid increase in signal is due to the diodes detecting the emission originating from a larger number of hot electrons than before the laser ablates through the target.

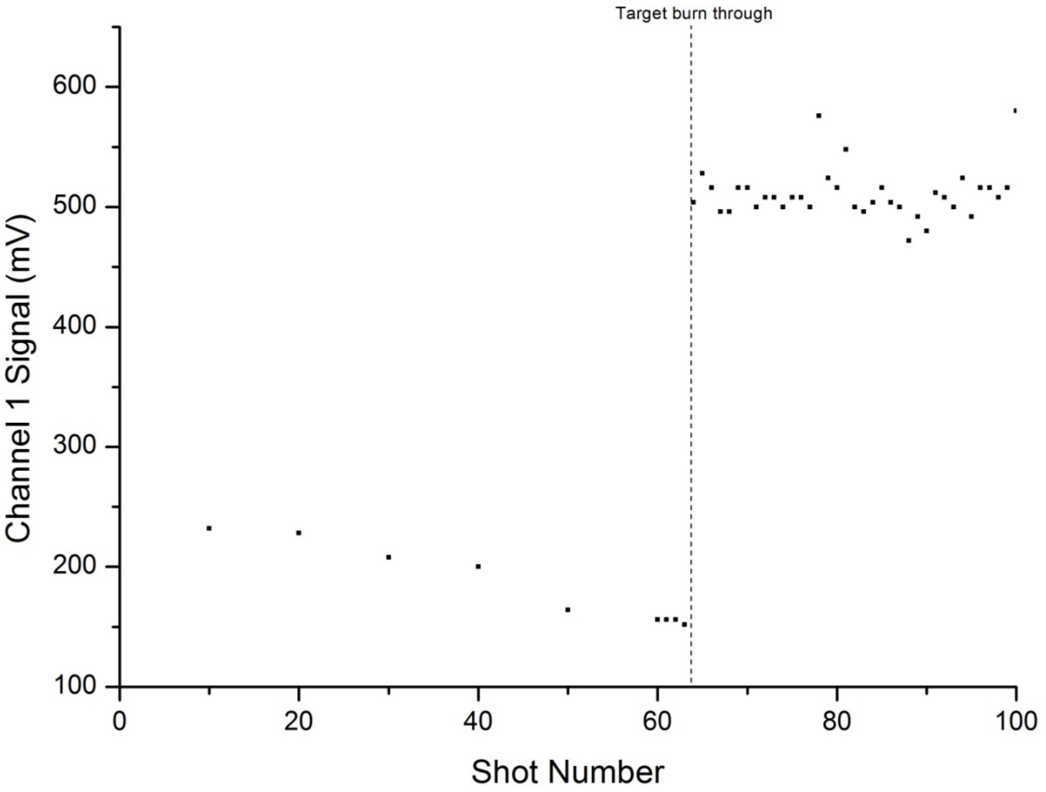

Figure 3.20 Variation in diode signal on channel 1 demonstrating the rapid enhancement of hot electron generation upon target burn through.

The cavity the laser produces is approximately conical in shape, shown in figure 3.21, with a front aperture of diameter 0.55 ± 0.02 mm and a rear aperture of 0.18 ± 0.02 mm. As a result of this open ended conical cavity, or conical frustum, the plasma density profile changes dramatically and as a result changes the mechanisms behind the hot electron generation.

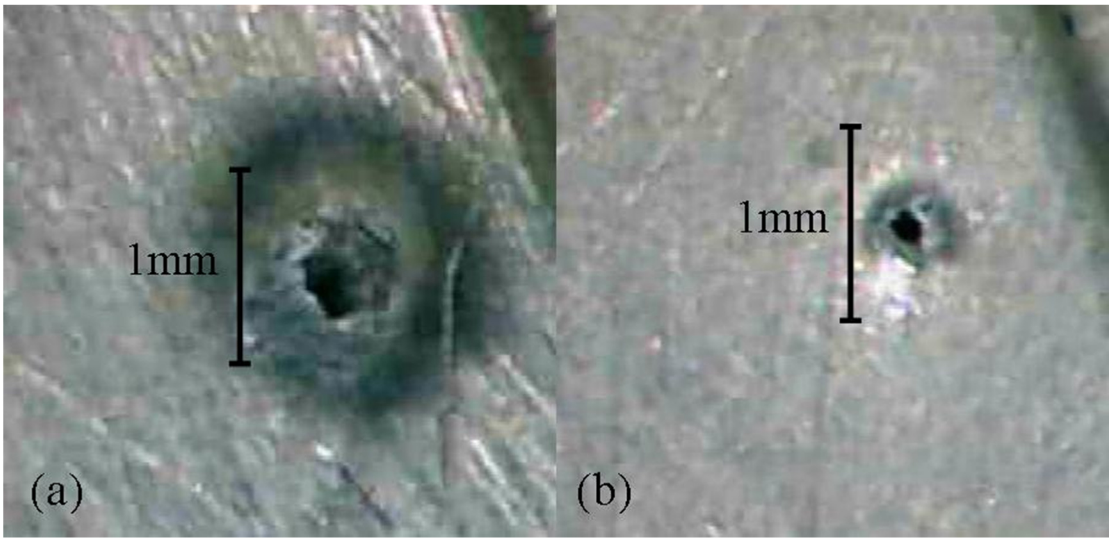

Figure 3.21 Cavity produced by laser 'burn through' as viewed from the front surface (a), and the rear surface (b). The thickness of the aluminium target is 2mm.

The laser continues to interact with the sloped walls of the conical frustum producing hot electrons via resonance absorption (see section 2.1.2) as is observed before burn through noted by the small reduction in hot electron temperature and number as the cavity is forming and the laser is de-focussing. As is shown in figure 3.22, the plasma density profile along the laser axis would be expected to change from an approximately exponential profile to a more Gaussian like profile with a sub-critical peak density. When a calorimeter is placed at the rear side of the target, it is found that ~ 3% of the incident laser energy emerges from the hole produced by the laser burning through the target. This is an indication that the plasma within the cavity, along the laser axis, is sub-critical and can also be shown by estimating the plasma expansion from the ion sound speed, shown in figure 3.22.

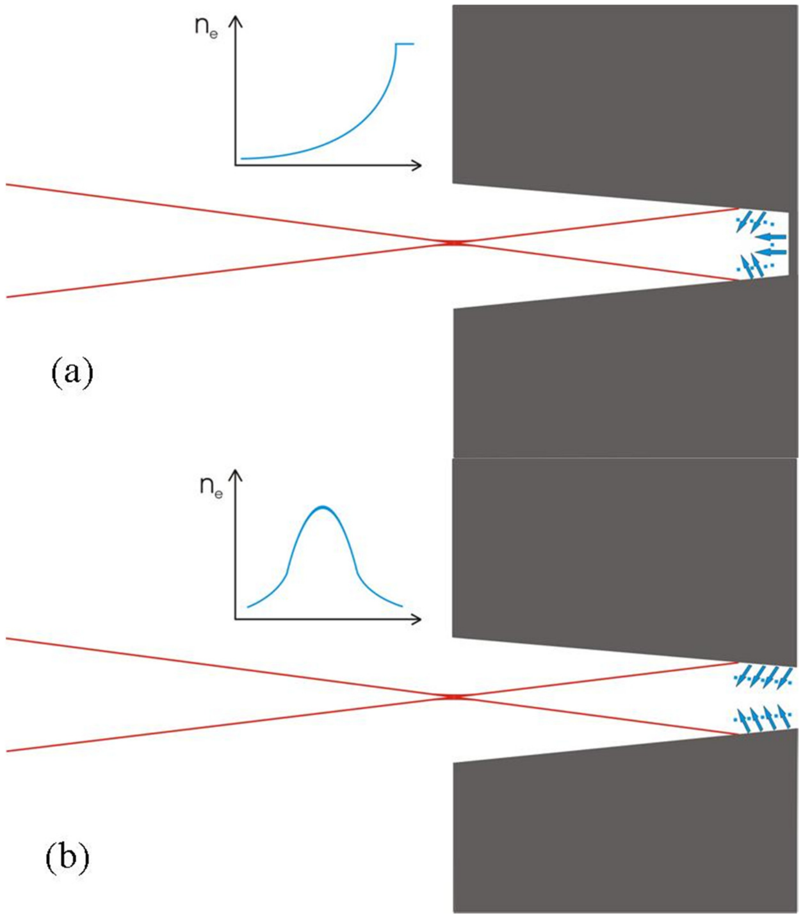

Figure 3.22 Scale diagrams demonstrating the laser beam expansion within the conical cavity before (a) and after (b) burn through. The plasma expansion is directed along the blue arrows and the plasma expansion is shown by the blue dots representing the scale length of the produced plasma. The graph inserts show the expected density profiles schematically.

It has been shown that the interaction of a laser pulse in this irradiance regime with a density profile as shown in figure 3.22(b) can cause a reduction in the irradiance threshold for Stimulated Raman Scattering (SRS) [69]. The result of this would be to increase the volume over which the hot electrons are generated, thus increasing the number of hot electrons as observed.

Work has been carried out more recently investigating the effect of low density foams within a cone-in-shell target for laser fusion by fast ignition [70]. The purpose of the low density foams is to produce near-critical density plasma when they are irradiated by a laser pulse [70-72]. This near-critical density plasma is seen to enhance laser coupling in the plasma and has been found to produce an approximately 3 fold increase in the number of hot electrons with little variation in hot electron temperature [70,72]. A similar effect is observed in this experiment using a lower irradiance (~ 10^{15} W cm^{-2}) than previously investigated and without the low density foam to produce plasma with reduced mass density. In this experiment, the sub-critical density plasma is produced through the interaction of an expanding laser beam with the sloped walls of an open ended conical cavity. This technique could potentially be scaled to higher irradiance to produce a larger number of hot electrons whilst maintaining hot electron temperature, which increases with irradiance. This is highly desirable for fast ignition ICF as the energy of the fast electrons must be carefully controlled in order to heat the ignition region within an ICF capsule [29,73].

3.7 Future Experimentation

As the experiment outlined is a highly reproducible source of hot electrons, it is also a reproducible source of K_α emission as outlined in section 2.3.3. Hot electrons with a temperature of ~7 - 8keV as described here are the most efficient at producing Al K_α emission at 1.5keV as the cross section for the creation of a K-vacancy by electron impact peaks for electrons of temperature 7 - 10keV [74]. A laser produced source of hot electrons and K_α emission of this sort has a number of experimental applications which will now be discussed.

3.7.1 Opacity Measurements

K_α emission can be used as an x-ray back-lighter to probe the opacity of plasma at a specific wavelength. This technique involves measuring the transmission of K_α photons through a plasma produced via a secondary heating mechanism, for example a second laser, or plasma heated via thermal conduction from the front side of the laser produced K_α source. A feasibility study of this type of experiment was performed at the Bhabha Atomic Research Centre (BARC), Mumbai and is presented in chapter 4 and in reference [75].

3.7.2 Hot Electron Interactions

The interaction of hot electrons within a solid target is of particular importance to inertial confinement fusion [54]. For example, heating by hot electrons is of particular importance [54,73] as the concept of fast ignition relies on using an ultra-intense laser pulse to ignite the high densities required for high gain. This is done by generating a beam of electrons (or more recently protons [76]) which propagate towards the core and deposit their energy, heating the fuel, causing ignition [77]. Although the electrons generated in this experimental set-up have a temperature of 7 - 8 keV as opposed to the MeV required for fast ignition [78], the electron source can be used to test theories of hot electron heating in the lower temperature regime. This could be achieved by irradiating a thin foil of Al to produce the hot electrons and positioning a thin foil of some metal to be tested at the rear side and measuring the temperature change. The temperature increase could be determined by absolute time gated imaging in the visible and assuming a black body.

Another interesting aspect concerning the hot electron generation and interaction with matter is that of the divergence of the electron beam. This could be tested using the experimental arrangement described with a series of targets created with buried tracer layers at different depths, for example silicon. Silicon has a K_α energy of 1.74keV, and the electron impact K-shell ionisation cross-section is at its highest for electrons with 7 - 10 keV energies [74]. Using an imaging spectrometer at the rear side of the target to image the Si K_α signal at different depths within the target would give information regarding the divergence of the electron beam.

As is described in section 3.6.3, when the laser ablated through the aluminium disk, the diode signals increased rapidly. Additional work needs to be done to investigate this further, and is part of a subsequent project. This includes the use of different targets with different conical angles and made from different materials as is seen in some recent experimental studies using high power laser systems [66,69-71]. The advantage of having a table-top laser system with this capability means a wide variety of targets can be tested, from which better decisions can be made regarding the construction of targets for experiments using the larger facilities. Similar experimentation using large scale facilities will allow an investigation into the feasibility of scaling the method described to higher irradiances more relevant to fast ignition inertial confinement fusion.

3.8 Conclusion

The x-ray diode array described in this chapter has been used to determine the hot electron temperature of a laser produced plasma with a high level of accuracy. The laser system used has demonstrated a high reproducibility, not only in energy on target (within 10% variation) but also in the produced hot electron temperature which is seen to vary less than 4% over 5 shots on the same target area. Due to this high reproducibility, a comparison of the average hot electron temperature was made between a single photon counting spectrum averaged over 900 shots and average diode signals obtained over 128 shots (128 shots due to a restriction on the oscilloscope). This comparison showed a good agreement in the hot electron temperature, well within experimental error. The XRD array is effective, robust and can be used in a single shot mode to determine the temperature of the hot electron component within a laser produced plasma in real time.

The high reproducibility of the laser system was largely due to the effectiveness of the retro-focussing system, allowing for best focus to be achieved easily and reproducibly under vacuum. Although the initial set-up can be complex, once completed, the system works well. The simple retro system can be achieved by using a simple webcam as opposed to a more expensive CCD.

Once installed and tested, the XRD array showed a rapid enhancement in hot electron generation when the laser burnt through the aluminium target producing a cone shaped cavity with an exit aperture. Approximately 3% of the incident laser energy is seen to emerge from the rear side of the target, indicating sub-critical plasma. This enhancement in the number of hot electrons generated within low density plasma is currently of particular interest to fast ignition fusion research. Previous work involved the use of low density foams to produce a near critical density plasma which enhanced the number of hot electrons produced. This technique produces a similar effect without the need for a foam target and could potentially be scaled for larger irradiances more relevant to the hot electron temperatures required for fast ignition.

Possible future avenues of research have been discussed including the use of K_α emission as an opacity probe. The initial feasibility experiment demonstrating this procedure is discussed in chapter 4. The laser set-up and diagnostics described here were used to prepare for an experiment at the Central Laser Facility, Rutherford Appleton Laboratory, detailed in chapter 6. The experiment discussed in chapter 6 discerns between the effects of relativistic particle heating and the effects of thermal radiation and hydrodynamics within a laser produced plasma by examining the Rayleigh-Taylor instability using a Ti K_α back-lighter.

4. K_α Emission as a Back Lighter to Probe Plasma Opacity of a Conductively Heated Target

4.1 Introduction

As discussed in Chapter 1 and 2, the experimental determinations of opacity for a range of plasma parameters are necessary for a wide range of applications. Methods used previously [13,14] to determine plasma opacity include the use of x-rays emitted from laser produced plasmas as back lighters to probe heated targets. More recently, EUV lasers have been utilised to probe buried layer targets heated by a laser pulse [17]. Multiple beam, high powered lasers have usually been needed to undertake opacity measurements due to the requirement to heat the opacity target and the x-ray back lighter source separately [13,14,17]. Some single laser beam plasma opacity measurements have been undertaken using recorded emission from buried layer targets. Here the plasma is assumed to be in LTE and Kirchoff’s law is used to infer opacity from the emissivity [11]. The work presented in this chapter has been published in Journal of Physics B: Atomic, Molecular and Optical Physics [75].

In this work, we report plasma opacity measurements recorded using a single laser beam to heat the material and produce the back lighter source. We use a single target comprising two layers as a heating source for the probed material, through thermal conduction, and for the probing x-ray emission source. The iron plasma conditions are estimated using 2D fluid code simulations performed by L. M. R. Gartside at the University of York and are summarised in section 4.3.5. With the technique presented here, it is possible to record the opacity of colder material, where emission is too weak for single beam opacity measurements utilising Kirchoff’s law [11].

4.2 Experimental Design

The experiment was carried out using an Nd:glass laser system situated at the Bhabha Atomic Research Centre (BARC). This laser provides an output energy of 8 J per pulse with a duration of 500 ps. The p-polarized laser was incident onto targets at an angle of 45^o to the target normal and focused to a spot size of 120 μm using an f/5 lens, yielding an on target peak intensity of 1.4×10^{14} W cm^{-2}. The targets comprised 0.8 μm thick Al, coated using a thermal evaporation plant, onto a 1 μm layer of Fe foil, supported by photo etched copper mounts with a circular target area of diameter 1 mm. The aluminium side of the targets was irradiated by the laser. Pure aluminium foils of thickness 0.8 μm, mounted in a similar manner, were used as targets for comparative purposes.

A crystal spectrometer was utilised to measure aluminium He- and Li- like lines and the solid K_α emission transmitted through the aluminium and iron layers. The spectrometer was positioned at the rear side of the target along the axis of the laser at 45^o to the target normal. Time integrated spectra in the wavelength range 7 – 9 Å, were recorded by dispersing the x-rays with a flat TAP crystal ($2d$ = 25.75 Å) onto a P-11 phosphor screen followed by an image intensifier tube and a CCD camera (PixelFly QE). Scattered visible light was prevented from entering the spectrometer using B10 filters (aluminised polycarbonate, Alexander Vacuum Research, Inc.). The spectral resolution of the spectrometer was dominated by the source size with $\lambda/\Delta\lambda \approx 400$. Four silicon photodiodes (XUV-100, OSI Optoelectronics), under reverse bias, were used to measure the time and space integrated emissivity of the aluminium plasma. Filters of 5 μm & 20 μm Al, 5 μm Ni, and 12 μm Ti were used to control the spectral range recorded (see figure 4.2). The filtering used in this experiment differs from that described in chapter 3 due to availability of foils at the facility. The diode active area is $100 mm^2$, but different sized apertures were utilised to avoid detector saturation. The diodes viewed the front side of the irradiated targets.

Aluminium K_α emission, at 1.5 keV, from pure 0.8 μm thick aluminium targets was used to calibrate the backward directed emission without an iron layer so that the transmission of iron heated by thermal conduction from the aluminium plasma could be recorded when shots with the iron and aluminium targets were employed. Al K_α emission occurs during the laser pulse as it relies on the hot electron interaction with solid Al and so is used for our time integrated transmission measurements because the time of emission is well defined. Test measurement of transmission through unheated iron placed 7mm behind a pure aluminium target showed that the iron transmission, T, measured by this technique, is within 14% of the value (T=0.067) predicted by Henke et al. [62] (see figure 4.7).

4.3 Analysis

The relatively long laser pulse length of 500 ps allows time for sufficient plasma expansion during the initial rise time of the pulse to provide the large under dense plasma necessary for whole beam self-focussing [79]. Estimation of the ion sound speed ($\sim 8 \times 10^4$ ms^{-1}) yields a scale length of ~ 40 μm at the peak of the laser pulse. A two temperature electron distribution is observed within the Al plasma. Source broadened spectroscopy provides an ‘emission map’ of the plasma and shows a central hot plasma surrounded by cooler material, while measurements of continuum emission show the presence of two temperature components.

4.3.1 Diode Array

Due to the differing filters used for the x-ray diodes in this experiment, both bound-free and free-free emission must be considered as soft x-ray emission is not as effectively attenuated as for the filters described in chapter 3. Continuum emission from the Al plasma is measured using filtered EUV enhanced silicon inversion layer photodiodes. Assuming Maxwellian electron distributions, the continuum emission from the Al plasma can be modelled using [80]:

$$j(\nu) = n_e n_i Z^2 \left(\frac{e^2}{4\pi\varepsilon_0}\right)^3 \frac{8\pi}{3\sqrt{3}m^2c^3}\left(\frac{2m}{\pi kT}\right)^{1/2} \exp\left(-\frac{h\nu}{kT}\right)\left[\bar{g}_{ff} + G_n\frac{\xi}{n^3}\frac{\chi_i}{kT}\exp\left(\frac{\chi_\mathrm{i}}{\mathrm{kT}}\right) + \sum_{p=n+1}^{\infty} G_p\frac{Z^2R_y}{p^2kT}\frac{2}{p}\exp\left(\frac{Z^2R_y}{p^2kT}\right)\right] \tag{4.3.1}$$

where m is the electron mass, R_y is the Rydberg energy, ξ is the number of holes in the ground state of principal quantum number n, $\overline{g}_{ff}$ is the free-free Gaunt factor and is assumed to be 1, G_n and G_m are bound-free Gaunt factors where $G_m = 0$ for $h\nu < Z^2R_y/m^2$ and $G_m = 1$ (or 1.4 if $T > 400$eV) for $h\nu > Z^2R_y/m^2$, $G_n = 0$ for photon energies less than the ground state ionisation potential χ_i, otherwise $G_n = 1$. Analysis of the continuum emission from the Al plasma using equation 1 and comparing the ratios between diode signals indicates the requirement for two temperature regions in order to reproduce the observed signals. The ionisation level, Z, and number densities of electrons and ions, n_e and n_i, are determined by assuming LTE within that region. Adapting this model to allow for two temperature regions of T_c and T_h with relative number fraction f, and incorporating the energy dependant transmission [62] of the filters (T_f) allows for the ratio between diode channels to be determined using:

$$R = \frac{\int_0^\infty T_{f1}(\nu)[G(T_c,\nu) + f^2G(T_h,\nu)]d\nu}{\int_0^\infty T_{f2}(\nu)[G(T_c,\nu) + f^2G(T_h,\nu)]\,d\nu} \tag{4.3.2}$$

where

$$G(T,\nu) = Z(kT)^{-0.5}\exp\left(-\frac{h\nu}{kT}\right)\left[\bar{g}_{ff} + G_n\frac{\xi}{n^3}\frac{\chi_i}{kT}\exp\left(\frac{\chi_i}{kT}\right) + \sum_{p=n+1}^{\infty} G_p\frac{Z^2R_y}{p^2kT}\frac{2}{p}\exp\left(\frac{Z^2R_y}{p^2kT}\right)\right] \tag{4.3.3}$$

and the subscripts *f1, f2* refer to different filters.

Equation 4.3.2 is numerically integrated also taking into account the effect of the photodiode depletion depth. By comparing calculated ratios, *R*, to experimentally measured diode signal ratios, it is possible to deduce the parameters T_c, T_h, and *f*. For example, analysing the ratio between the two highest energy diode channels, R_{High}, (5µm Ni and 12µm Ti) enables a hot electron temperature, T_h, of 1keV to be deduced to within 0.1keV accuracy, as there is negligible effect on this ratio due to a change in T_c or *f*, as shown in figure 4.1.

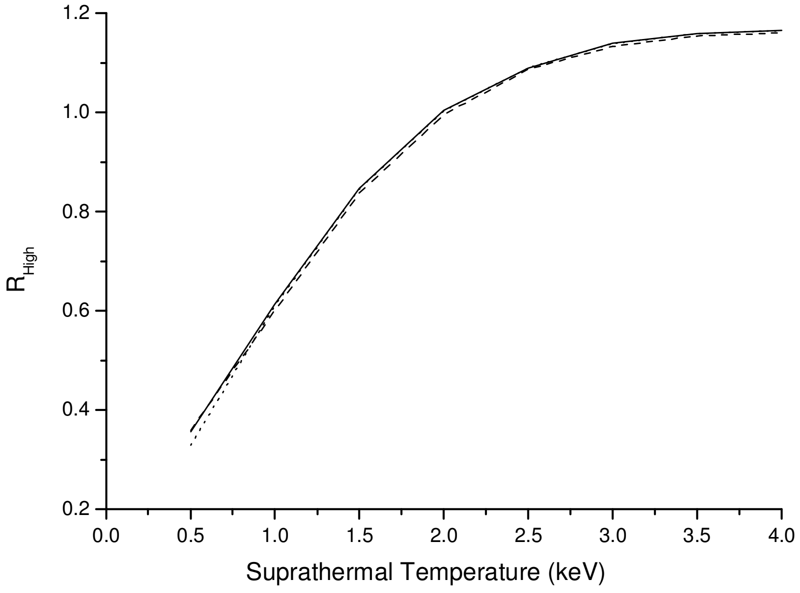

Figure 4.1. Variation of diode signal ratio for the two highest energy channels (5µm Ni and 12µm Ti) as a function of the hot electron temperature. The solid line represents a cold electron temperature of T_c = 140eV and relative fraction of hot to cold number, *f* = 0.008, while the dashed line represents T_c = 240eV and *f* = 0.008 and the dotted line represents T_c = 140eV and *f* = 0.05

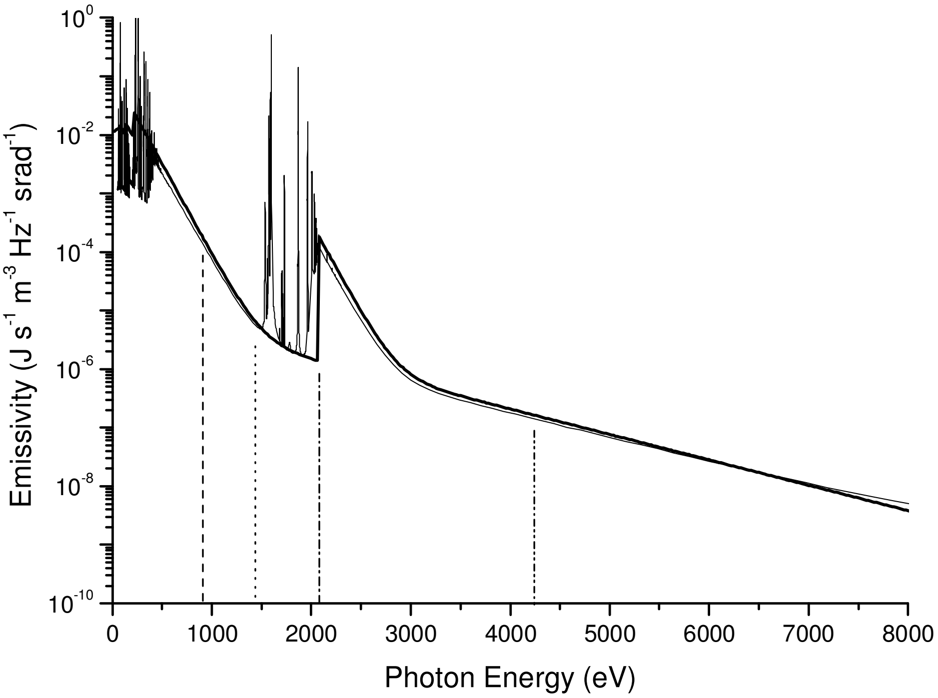

Figure 4.2. Continuum emission from the laser produced aluminium plasma as predicted by equation 1, incorporating two temperature regions within the plasma (thick solid line) with a comparison of total emission as predicted by FLYCHK [44] (thin solid line). Conditions used are T_c = 140eV, T_h = 1000eV and f = 0.008. The peak of the transmitted emissivity curves for the diode filters of 5μm Al (dashed line), 20 μm Al (dotted line), 12 μm Ti (dash-dot line) and 5 μm Ni (dash-dot-dot line) are indicated.

To determine the remaining 2 parameters (T_c and f), a minimisation routine is performed using ratios from all channels to find a best fit of the model (equation 4.3.2) to the experimental data. This yields a thermal temperature of T_c = 140 ± 10eV and a fraction of f = 0.008 ± 0.001, consistent over multiple shots. The peak of the spectral range detected by the diodes for the filters and experimental parameters is illustrated in figure 4.2. A comparison of equation 4.3.1, with temperature T_c = 140eV, T_h = 1keV and f = 0.008, is also made on figure 4.2 with the total emissivity as predicted by the FLYCHK code [44]. The model shows good agreement with continuum emission, omitting line radiation as expected. When the energy dependant filter transmission is included, the integrated diode signals as predicted by our model using equation 4.3.1 and FLYCHK agree to within 4%, so our omission of the small contribution to the diode signal from line emission is not significant.

Figure 4.2 shows the photon energies where the filtering for each diode gives maximum recorded x-ray flux and illustrates how we can use the four diode signals to measure T_h, T_c and f. The spacing of these peaks allows the determination of the hot temperature, T_h, component (from signal ratio R for the two highest energy channels), the cold temperature, T_c, component (from the signal ratio R of the two lowest energy channels) and the ratio, f, the number of hot to cold electrons (from the ratio of the two intermediate channels).

4.3.2 TAP Crystal Spectrometer

A crystal spectrometer utilises the Bragg condition, $n\lambda = 2d\sin\theta$, where n is an integer representing the order number, λ is the wavelength of light, d is the inter-atomic spacing of the crystal and θ is the Bragg angle. When light incident on a crystal has a wavelength comparable to the inter-atomic spacing of that crystal, the light is diffracted, causing constructive interference in accordance with the Bragg condition. Optimisation of the crystal angle with respect to a laser produced plasma allows for the light to be dispersed producing a spectrum. In this experiment, a flat thallium acid phthalate (TAP) crystal ($2d$ = 25.75 Å) is used to disperse x-rays emitted from the laser produced plasma and is optimised to record the spectral region of 1440 – 1620 eV, corresponding to a number of aluminium spectral lines.

The recorded time integrated aluminium spectrum (see figure 4.3 for example) predominantly comprises a series of lines originating from helium-like and lithium-like ions. The most prominent of these lines is the He-like resonance line (w), purposefully instrument saturated to enable an improved resolution of the intercombination line (x, y) and the Li-like satellites (abcd, jkl, op, qr), (the standard letter designation used here for He-like satellite lines has been tabulated by Gabriel [81]). Line ratios between the Li-like and He-like lines enable the determination of plasma characteristics through comparison with the spectral modelling code FLYCHK [44]. Utilising the relative intensity of the He-like intercombination line and the Li-like satellites provides a useful diagnostic tool giving a measure of the electron densities and temperatures in the aluminium at the time and position of peak emission. FLYCHK does not simulate the aluminium K$_\alpha$ emission which is produced by the hot electron interaction with solid aluminium.

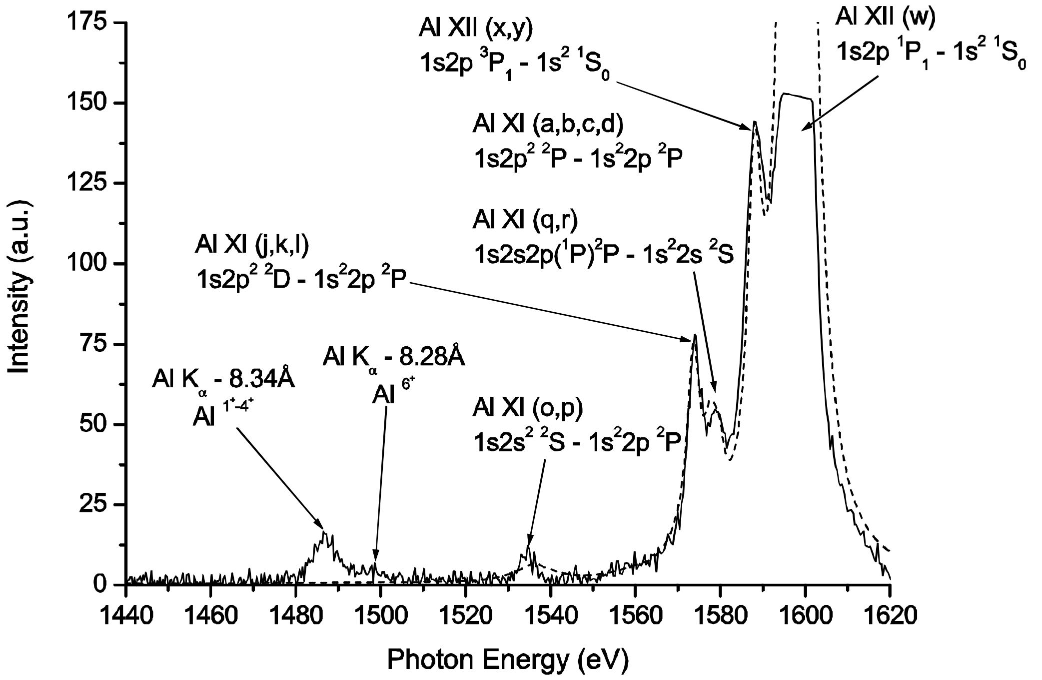

Figure 4.3. Experimental aluminium spectrum (solid line) and superimposed simulation (dashed line) of temperatures $T_c = 140$ eV and $T_h = 1$keV using FLYCHK. The fraction of suprathermal to thermal electrons is $f = 0.008$ [44,82].

In order to obtain a fit to the spectra, such as figure 4.3, using FLYCHK, a parameter scan was performed trialling a range of temperatures (50 – 500 eV) and densities (10^{12} - 10^{21} cm^{-3}). The simulated spectra were instrument broadened with our estimated resolution (~ 3eV) using a post-processor [83] and the peak to peak ratios were deduced and compared with the experimental spectra. A single thermal temperature component could not reproduce the observed spectra. An electron density of $n_c = 5\text{x}10^{20}$ cm^{-3} was found to best fit the spectra, consistent with the turning point density for a 45° obliquely incident 1.06μm Nd:glass laser. As the emission is proportional to n_e^2 and $n_e = 5\text{x}10^{20}\text{cm}^{-3}$ is the highest density directly heated by the laser, we assume emission from this single density is a reasonable approximation to a spatial integration of emission. A parameter scan of the hot electron temperature, T_h, (0.5 - 2keV) and hot to cold component fraction, f, (0.005 - 0.1) was performed and found to require $T_h = 1$keV and $f = 0.008$ for $T_c = 140$eV (see e.g. figure 4.4).

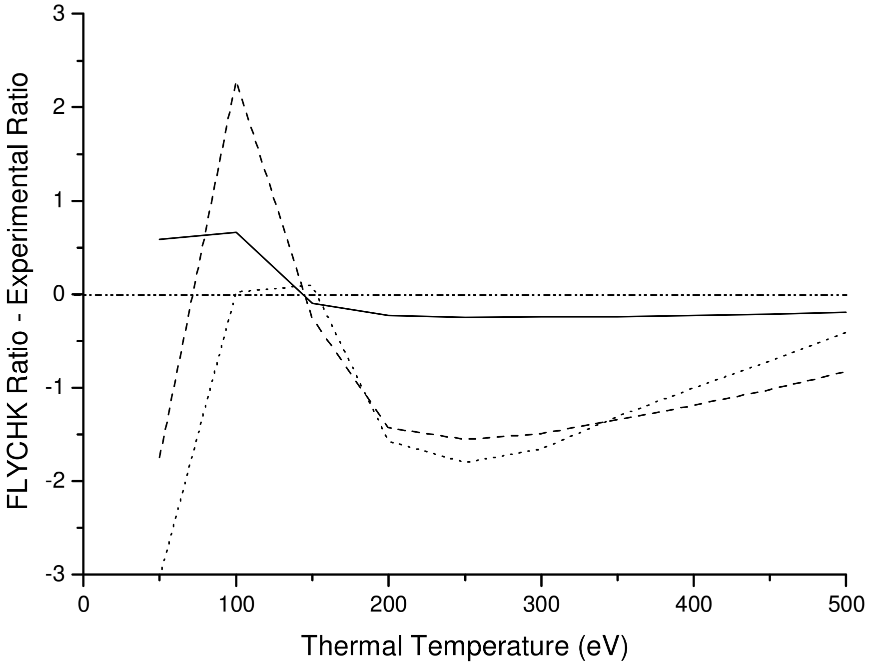

Figure 4.4. Plot of the difference between the satellite ratio determined via FLYCHK and our experimentally measured ratio for satellite lines qr/jkl (solid line), xy/jkl (dashed line), and xy/qr (dotted line) as a function of thermal temperature. The case shown is for T_h=1keV and f=0.008 (best fit). The ratio differences indicate that T_c=140eV.

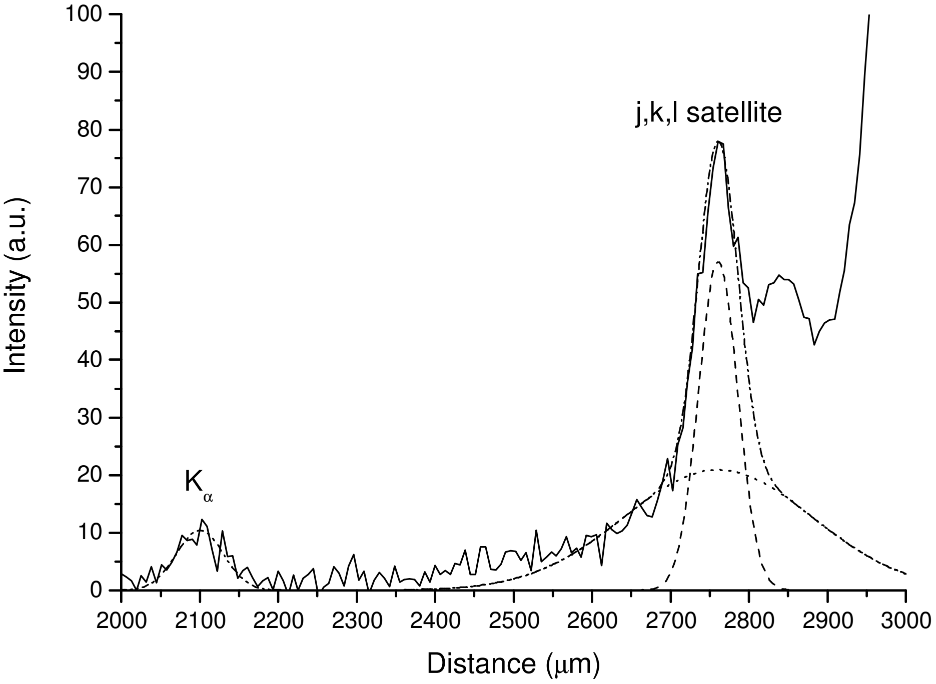

Figure 4.5. Expanded experimental spectrum as a function of distance on the CCD detector with a distance scale corresponding to the source broadening effect on the spectra. A double Gaussian profile for T_c=140eV and 120μm width at the target (dotted line) and of T_h=1keV and 25μm width at the target (dashed line) combine to form the emission profile observed. The K$_\alpha$ peak is best represented by a single Gaussian (dash-dot-dot line) with a spatial width of 60μm.

4.3.3 Spectral Line Profiles

It was found that He-like satellite spectra were best modelled using a double Gaussian line profile. The spectral profiles are strongly source broadened ($\lambda/\Delta\lambda \approx 400$), so the line profile represents a mapping of the spatial emission profiles of the lines, indicating two temperature regions. The superposition of source broadening effects due to a 25μm diameter plasma region of electron temperature T_h=1keV and a 120μm diameter region of electron temperature T_c=140eV is shown on figure 4.5 to fit the experimentally measured line profiles. The relative abundance of the number of hot and cold electrons used for this calculation is f = 0.008, with intensity information obtained from FLYCHK. This relative abundance of hot and cold electrons is approximately consistent with the spatial dimensions of hot electrons (a circular region of radius r = 12μm) and cold electrons (a circular annulus region of radius between r =12μm and R = 60μm). Assuming uniform ablation, we would expect $f = \frac{\pi r^2}{\pi R^2 - \pi r^2} \cong 0.04$, but this could readily drop to f = 0.008 if the T_h value is produced late in the irradiation history or at limited spatial distance from the target surface. Assuming the plasma emission is cylindrically symmetric, the 1D double Gaussian plasma profile, shown in figure 4.5 can be extended to map the 2D temperature profile as shown in figure 4.6.

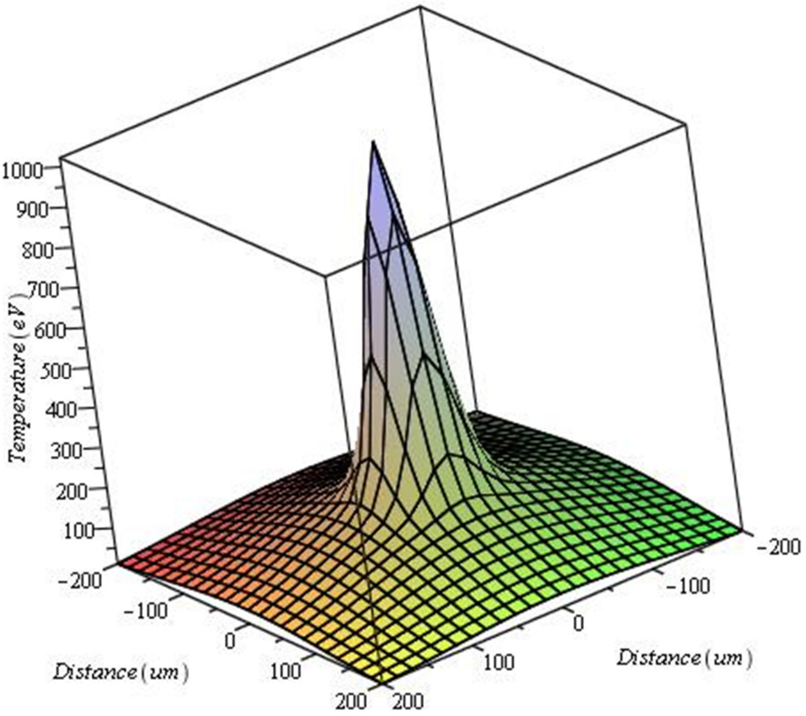

Figure 4.6 Two dimensional temperature profile for the aluminium plasma with a double Gaussian structure of T_c=140eV with 120μm width and of T_h=1keV with 25μm width.

4.3.4 Aluminium K_α Transmission Measurements

The spectrally integrated Al K_α intensity recorded by the spectrometer after transmission through the iron layer was measured for different laser pulse energies and directly compared with the integrated K_α signal originating from a pure Al target created using the same laser energy. A comparison of the transmitted and uninhibited spectra for a laser energy of 7.7 J is shown in figure 4.6. Figure 4.7 demonstrates the change in transmission over the laser energy range investigated and shows a comparison to cold Fe transmission. It is seen that an increase in laser energy of 1.3 J causes sufficient additional heating to the iron layer through enhanced thermal conduction to produce an increase in transmission by almost a factor of 3.

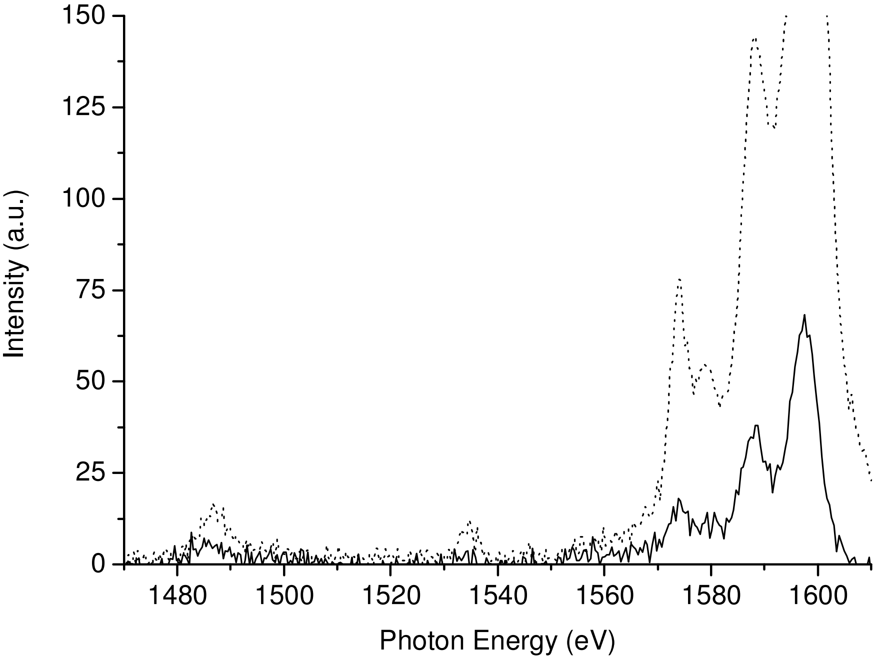

Figure 4.6. Experimentally observed, transmitted Al spectrum through an Fe plasma (solid line) and the spectrum from an aluminium target without iron (dotted line) for a laser energy of 7.7J.

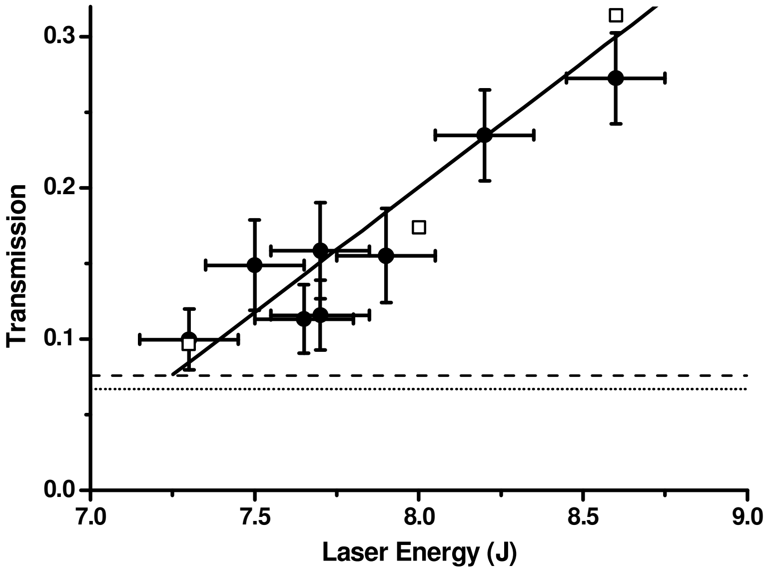

Figure 4.7. Transmission of K$_\alpha$ photons (1.5 keV) as a function of laser pulse energy as determined by experiment. Experimentally measured cold Fe transmission (dashed line) is compared with cold Fe transmission predicted (dotted line) by Henke et al. [62]. The open squares show calculated transmissions from h2d simulation, with line of best fit (solid line).

4.3.5 h2d Simulations

Two dimensional fluid code simulations have been used to estimate the plasma conditions of the aluminium-iron target using the h2d code [84]. The h2d code uses a Lagrangian coordinate system in cylindrical geometry to determine the plasma density, temperature and ionisation as a function of distance and time. Hydrodynamic variables are then calculated using the SESAME equation of state package, developed by the T-1 group at Los Alamos National Laboratory [85]. Opacity data from the Ionised Materials Package code (IMP) [86] was then used to calculate the transmission of Al K$_\alpha$ through the heated Fe layer. Full details of the simulations summarised here are available in a published paper [75].

A laser of pulse length 500ps and a focal spot of 120μm is assumed incident onto a cylindrical target of aluminium and iron, 200μm in diameter, for the h2d simulations.

The h2d simulations predict similar conditions within the aluminium plasma to those predicted by the spectral profile analysis and the x-ray diode array (figure 4.8).

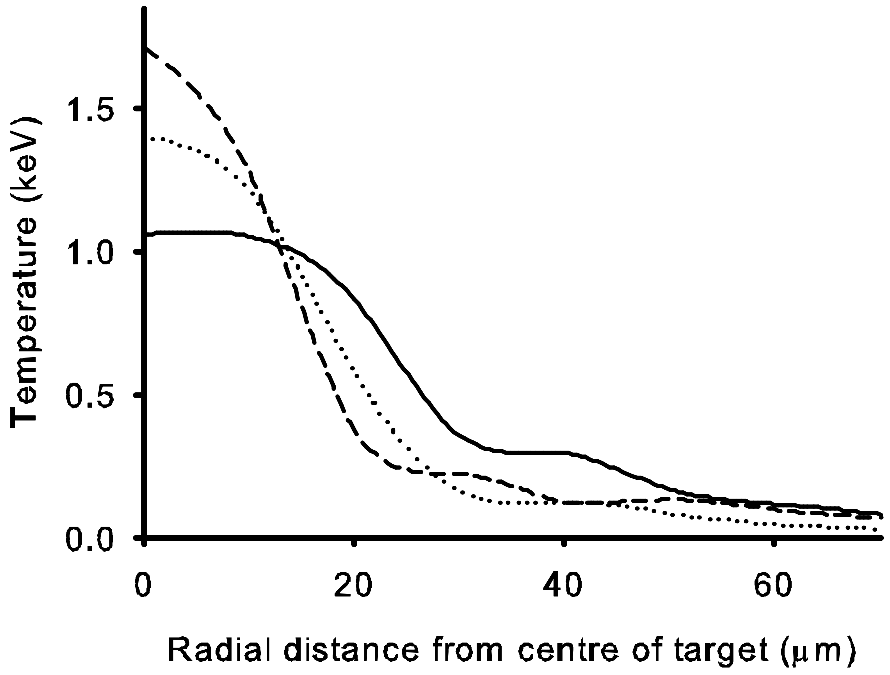

Figure 4.8 Radial temperature profiles produced by a 500ps pulse incident onto the Al side of an Al and Fe target. The simulated critical surface temperatures at the peak of the heating pulse are shown for the laser energies 7.3J (solid line), 8J (dotted line) and 8.6J (dashed line).

The K_α emission originating from the aluminium is estimated using the conditions predicted by the 2D simulations, assuming a Maxwellian distribution of electrons and a constant cross section for K_α production for $E > E_{K\alpha}$, where E is the electron energy and $E_{K\alpha}$ is the Al K_α photon energy.

The transmission as predicted using IMP tabulated opacities is shown in figure 4.9 and demonstrates the peak of transmission is close to the peak of the heating pulse. The transmission data shown in figure 4.9 is in agreement with the experimentally deduced transmission measurements shown in figure 4.7. Figure 4.10 shows the axial temperature profiles of the Fe layer at the time of peak Al K_α transmission as predicted by h2d.

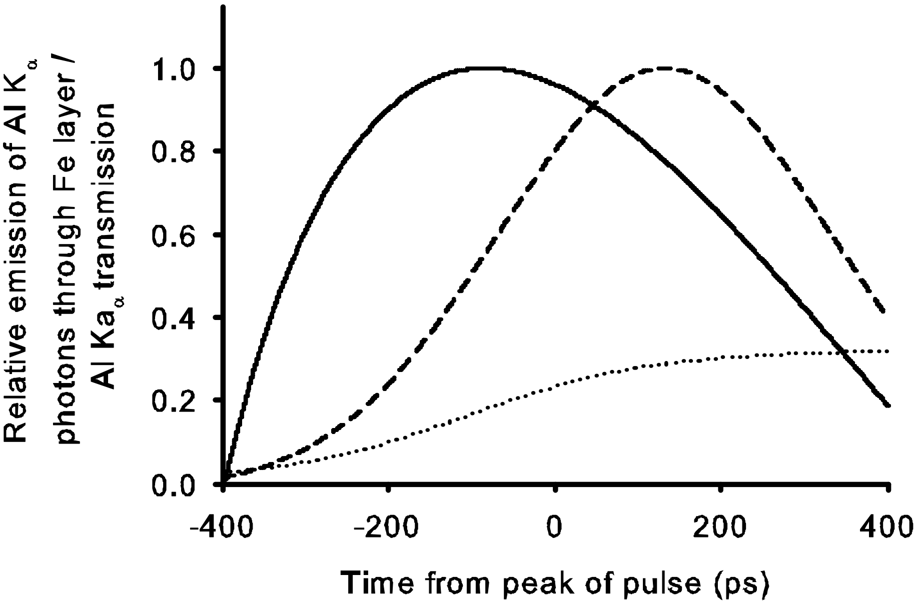

Figure 4.9 Relative emission of Al Ka photons through the conductively heated Fe layer as predicted by h2d and IMP opacities. The transmitted flux (dashed line) is the product of the Al K$_\alpha$ emission (solid line) and the Fe transmission (dotted line).

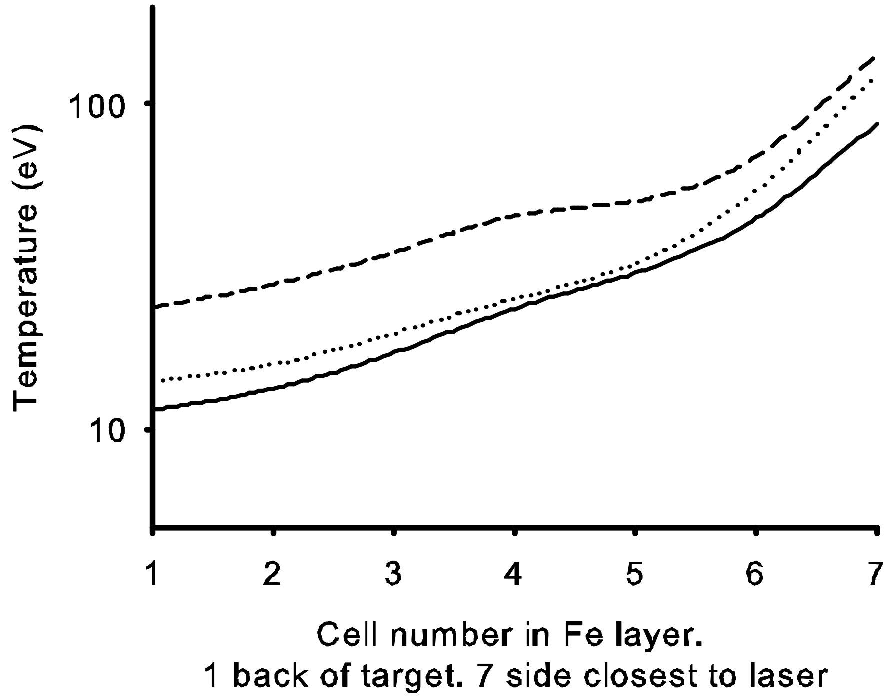

Figure 4.10 Axial temperature profile within the Fe layer at the time of peak Al K$_\alpha$ transmission. Laser pulse energies of 7.3J (solid line), 8J (dotted line) and 8.6J (dashed line) are shown.

4.4 Discussion

Experimental temperature and K_α transmission data agree well with simulations using h2d and opacities from the Ionised Material Package (IMP). A two temperature spatially separate thermal distribution of electron temperatures, as observed here, has recently been reported by Colgan, et al [87].

Aluminium K_α emission has been used in this experiment as there has been a significant amount of previous study into the K_α spectra of aluminium, and the photon energy (1.49keV) results in photo-ionisation from the ground to continuum of Fe up to Fe XIX [88] so that there will be significant absorption of the radiation in iron plasmas up to electron temperatures $\approx$ 90eV. Once temperatures exceed $\approx$ 90eV, iron becomes close to transparent, so our K_α transmission measurements are a good diagnostic of temperatures > 90eV.

The assumption that Al K_α is emitted over a different timescale to that of other spectral lines, due to the hot electron interaction, has been checked by examining the transmission of He-like satellite lines through the iron. These lines were found to be more strongly transmitted by a factor of 2, compared with K_α transmission, suggesting more emission at later times when the iron transmission is greater.

The experiment has demonstrated the feasibility of performing opacity experiments using a table top laser system with modest parameters. Using this technique, we have been able to accurately characterise the Al back lighter and perform transmission measurements using a laser system with a high reproducibility (±10%) on a shot to shot basis. A number of issues need to be addressed to obtain high accuracy opacity information [89]. Simulations have demonstrated using this technique results in large temperature and density gradients in the axial and radial direction which would have to be accurately measured. Gradients in the axial direction can be reduced by introducing a plastic tamp layer on the rear side of the target, inhibiting the Fe plasma expansion, reducing the temperature gradient and providing conditions that can be validated more readily as LTE. Radial temperature gradients can be addressed by using a different heating mechanism than thermal self-focussing. Using a shorter pulse length laser would prevent whole beam self-focussing and could be optimised for resonance absorption to produce a higher number of hot electrons and to produce a shorter pulse back lighter. These hot electrons would increase the K_α signal and propagate into the Fe layer, heating the target, producing plasma with higher radial uniformity. The shorter pulse back lighter would provide better temporal resolution. Diagnosing the plasma conditions within the Fe layer has relied on using computer codes to simulate the thermal conduction from the front side Al plasma. An independent plasma diagnostic for the Fe layer is therefore required in order to determine the plasma conditions independently of hydrodynamic simulations. This could be achieved using absolute time gated imaging, probably in the visible, of the iron target to deduce a temperature assuming emission as a black-body.

4.5 Conclusion

A method for the characterisation of a plasma back lighter and the determination of plasma opacity using a single laser beam and a layered target has been investigated. Thermal conduction from laser produced aluminium plasma has been used as a heating mechanism for an iron target layer. K_α x-rays produced from the Al layer are used to measure transmission through the iron plasma. Whole-beam self-focusing of the laser has reduced the effective spot size and increased the energy deposition into the iron. The temperature increase in the iron allows for opacity measurement over a temperature range ~ 10 – 150 eV. Combining source broadened spectroscopy with continuum emission analysis has enabled a plasma back lighter produced by whole beam self-focussing to be characterised. The experimental data is in good agreement with 2D modelling using opacities from the Ionised Material Package code for 1.5 keV photon energy.

5. Characterisation of a Line Focussed EUV Back-lighter for Plasma Opacity Measurements

5.1 Introduction

As discussed in earlier chapters, opacity measurements at EUV wavelengths of high energy density plasmas are difficult to undertake as the probe has to overcome the high self-emission of the opaque plasma and it is difficult to create sufficiently uniform and well characterised plasma for accurate measurements. Laser produced EUV and x-ray back-lighters have been used previously to perform opacity measurements [13,14], when the flux of x-rays generated is sufficient to ‘outshine’ the plasma self-emission. More recently, much brighter plasma based EUV lasers have been employed to probe iron plasma [17]. In the present experiment, we set out to use a short duration (3ps) Ne-like Ge laser at 19.6nm to probe the opacity of laser heated iron.

This experiment generated an extreme ultra-violet (EUV) back-lighter in a set-up similar to that used to create a plasma based x-ray laser, without lasing being observed. A line focus back-lighter pointing at a sample can produce bright emission over a broad spectral range, from a small area, as the more intense spectral line intensities approach black-body intensities due to the high optical depth along the plasma line. This chapter is primarily concerned with the characterisation of the back-lighter with the aim of improving our understanding of the line focus EUV back-lighter and to investigate why lasing was not observed. Accurate information regarding the plasma conditions within the EUV source is required for high quality opacity measurements.

This chapter firstly discusses the experimental arrangement used in the experiment in Target Area West (TAW) at the Central Laser Facility, including a description of the diagnostics used. Section 5.3 discusses in detail the characterisation method used for the x-ray back-lighter. Section 5.4 briefly discusses the images obtained from the pinhole camera followed by a summary of the EUV transmission analysis (Section 5.5) carried out in conjunction with E. Wagenaars, University of York. Results presented in this chapter are available in published form [90,91].

5.2 Experimental Set-up

The back-lighter was created using two optical pulses from the VULCAN Nd:Glass laser system at the Rutherford Appleton Laboratory to irradiate a germanium target of thickness 500nm deposited onto a glass slab of 6mm width. A pre-pulse of duration 300ps and energy of 20J was focussed into a line 100μm × 6mm, using a refracting lens and a spherical mirror, giving an irradiance of $\sim 8 \times 10^{12}$ W cm^{-2}. A main (chirped pulse amplification or CPA) pulse of 3ps duration had an energy of 35J and was focused into a line of similar dimensions using a single f/3 off-axis parabola, giving an irradiance of $\sim 1 \times 10^{15}$ W cm^{-2}. The line foci of both beams were over lapped on the target, with a delay between the pulses of $\Delta t = 400$ ps.

A 50nm thick iron foil, tamped with 100nm thick paralene-N (C_8H_8) on both sides, mounted in a 0.5mm wide copper mount, was heated using another CPA beam from the VULCAN laser and the plasma created probed with the EUV back-lighter. The second CPA beam contained 25J energy in a duration of 1ps and was focused to a spot size of about 200μm in diameter on the opacity target. The delay between the heating pulse and the main CPA pulse was varied between 5 and 20ps to allow probing at different stages of iron plasma evolution.

5.2.1 Crossed slit and Pinhole Cameras

In order to verify the homogeneity and to enable the characterisation of the line focus on a shot-to-shot basis, a crossed slit camera is employed. The crossed slit camera allows for different levels of magnification in the horizontal and vertical directions using two orthogonal slits of different slit widths at different distances from the source. The layout is as shown in figure 5.1.

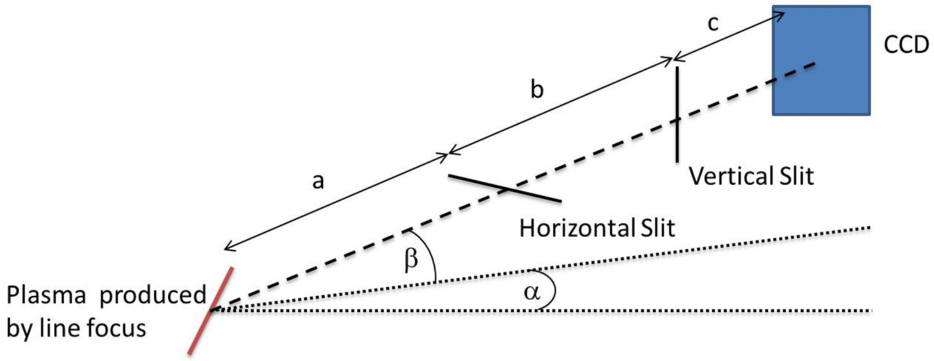

Figure 5.1 Configuration and definition of terms for a simple crossed slit camera

Using the terms as defined in figure 5.1, the magnification in the vertical and horizontal directions are calculated by

$$M_v = \frac{b+c}{a}\cos\beta \qquad\qquad M_h = \frac{c}{a+b}\cos\alpha \tag{5.2.1}$$

A crossed-slit camera with an Andor CCD was positioned at an angle of 22 degrees with respect to the plane of the target normal. The vertical and horizontal resolution was 19µm and 180µm respectively. The crossed-slit camera was filtered using 3µm aluminium and 25µm beryllium so that emission in the range 0.5 to 5 keV was recorded. The CCD had an exposure time of 500ms so we record time integrated Ge emission over the laser plasma lifetime. The parameters for the experiment gave a horizontal magnification of 1.2 and a vertical magnification of 3.6.

The pinhole camera uses a similar premise as the crossed slit camera, by replacing the double slits with a single pinhole. The pinhole produces a magnification dependent upon the distances defined in figure 5.2, where the magnification is given by

$$M = \frac{b}{a} \tag{5.2.2}$$

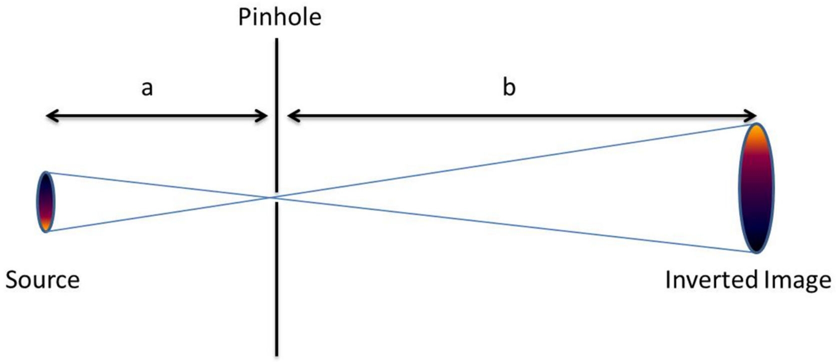

Figure 5.2 Geometry of a simple pinhole camera

5.2.2 Flat-field Spectrometer

The flat-field spectrometer provides spectral resolution in the vertical direction and angular resolution in the horizontal direction. X-rays are dispersed using an aperiodically ruled concave grating which is illuminated under a grazing angle by the source under investigation. An aperiodically ruled grating is used in order to compensate for the rapidly varying focal lengths between the central wavelength and those at the limits of the crystal position. The differing focal lengths lead to a curved focal plane, which reduces the resolving power of the spectrometer. The specially designed grating with varied groove spacing corrects for the differing focal lengths and focuses the x-rays onto a plane normal to that of the x-ray source.

5.3 Germanium Back-Lighter Characterisation

The crossed-slit images provide an ‘emission map’ of the Ge back-lighter and have been characterized using simulated data from the spectral modelling code FLYCHK [44]. The code was used to evaluate total emission from the Ge plasma as a function of photon energy and temperature for the density in the region of highest gain and emission as

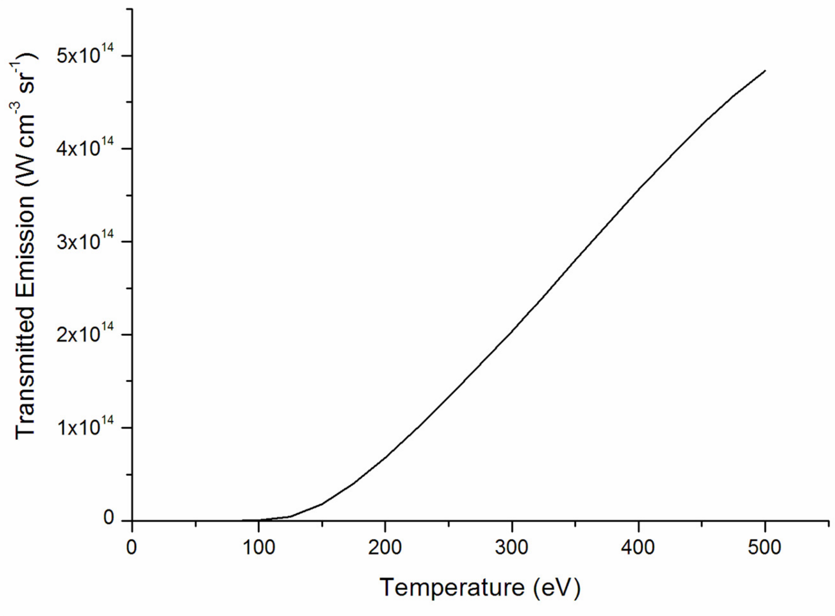

Figure 5.3 Spectrally integrated emission, transmitted through filters of 3µm Al and 25µm Be as a function of temperature for Ge as determined with the FLYCHK code [44] and using filter transmission data from Henke et al. [62]. The electron density assumed is that seen in the region of highest gain as predicted by Ehybrid (5×10^{21} cm^{-3}) [25].

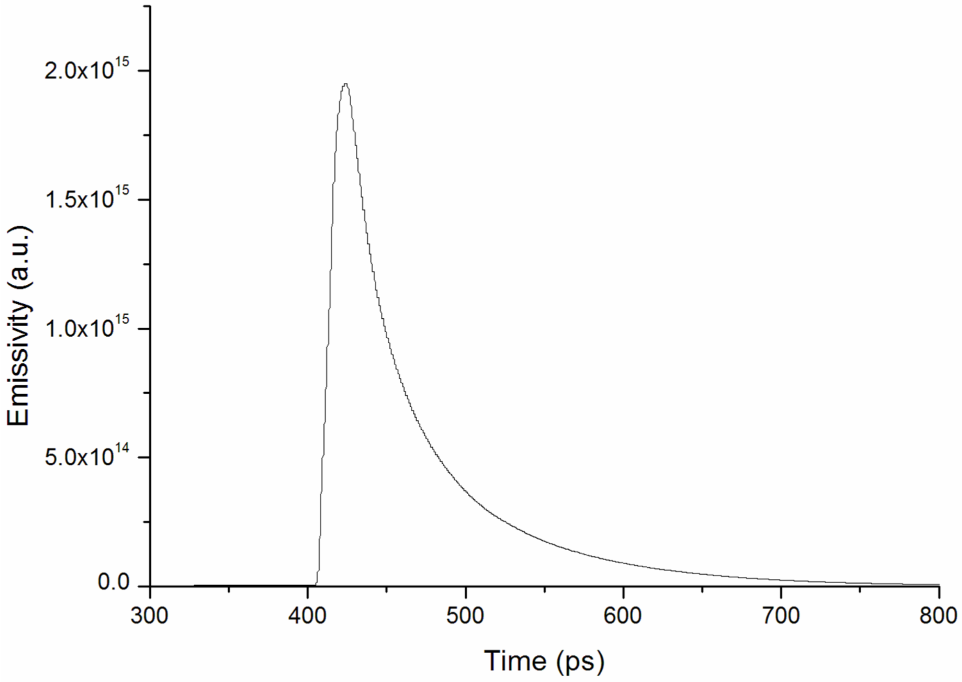

Figure 5.4 Emission of radiation from a Ge plasma transmitted through the filter combination for our crossed-slit camera as a function of time calculated by the Ehybrid [25] code.

predicted by the Ehybrid code [25] (n_e = 5 x 10^{21} cm^{-3}). Multiplying the photon energy dependant transmission [62] of the filter with the total emission and integrating over frequency gives the total transmitted emission as seen by the crossed-slit camera per unit volume (see figure 5.3). For our filter combination, the relationship between the transmitted emission and temperature is approximately linear in the temperature range of 150 – 500eV, with a threshold for any significant emission at ≈ 120eV. We assume that the plasma emission through the crossed-slit filter combination (3μm Al, 25μm Be) is dominated both spatially and temporally by the hottest temperature and highest density (5×10^{21} cm^{-3}) plasma. The area of plasma viewed by each pixel on the CCD is calculated using the geometry of the crossed-slit camera. A thickness of emitting plasma can be determined by calculating the plasma expansion from the turning point density by calculating the ion sound speed, v_s, for each temperature and considering a characteristic length scale, $v_S \Delta t$ (where Δt = 400ps, is the time between the pre-pulse and the main pulse). The time of emission of the plasma (100ps) is found from simulations using the 1D hydrodynamic code Ehybrid [25] (figure5.4).

A calibration factor for the CCD (8eV/count) is used to deduce the absolute number of counts per pixel associated with the transmitted emissivity. Figure 5.3 then enables the crossed-slit images of recorded emission to be converted to a spatial variation of electron temperature (figure 5.5 and 5.6). This conversion of CCD counts to temperature is reasonably accurate (±10%) due to the rapid linear increase of emission with temperature and the threshold temperature for any significant emission (see figure 5.3). The error estimate for the temperature measurement of ±10% does not include the error associated with our assumption of a spatially and temporally constant density and temperature. The incident laser irradiance profile has a width of 100μm and comparing this with the deduced temperature profile width of 150μm, the relationship $T_e \propto I^{\beta}$, results in $\beta = 0.44 \pm 0.05$ in agreement with temperature scaling results [92].

Simulations using Ehybrid demonstrate peak ionisation levels in agreement with the FLYCHK model used to determine the temperature profile of the back-lighter. The peak temperature of the pre-pulse only back-lighter was found to be 120eV or less. A peak temperature of 155 ± 20eV is found when the two-pulse set-up is used. These temperatures explain the presence of spectral lines from Ge XX to Ge XXIII [93-97] as seen in the spectrum shown in figure 5.7 and the significant change in emission between the pre-pulse and double pulse plasma. The figure 5.7 spectrum was recorded with a flat field spectrometer viewing down the line focus axis (see section 5.4).

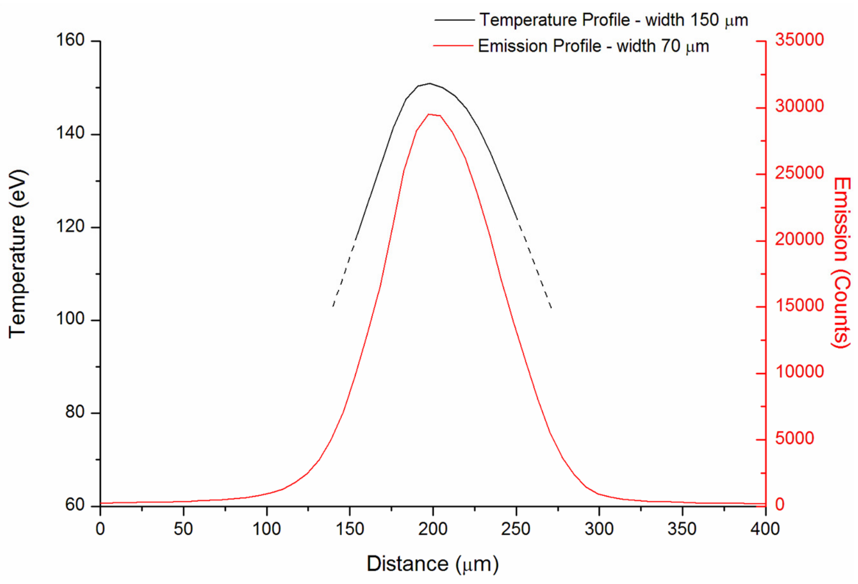

Figure 5.5 Emission cross-section over the line profile and the resulting temperature profile deduced as discussed in the text.

Although the experimental set-up was similar to that used to generate a plasma based x-ray laser, no x-ray lasing was observed. A temperature analysis of the pre-pulse only shots shows the temperature to be < 120eV, and according to ionisation curves simulated using the collisional-radiative code FLYCHK, the plasma then consists mainly of Ge^{19+} or lower ionisation stages. This ionisation is consistent with the peak ionisation determined via simulations using Ehybrid. For lasing the main pulse has to couple enough energy into the plasma to raise the ionisation level up to the Ne-like ionisation stage (Ge^{22+}) and provide the population inversion necessary for lasing, within the 3ps pulse length.

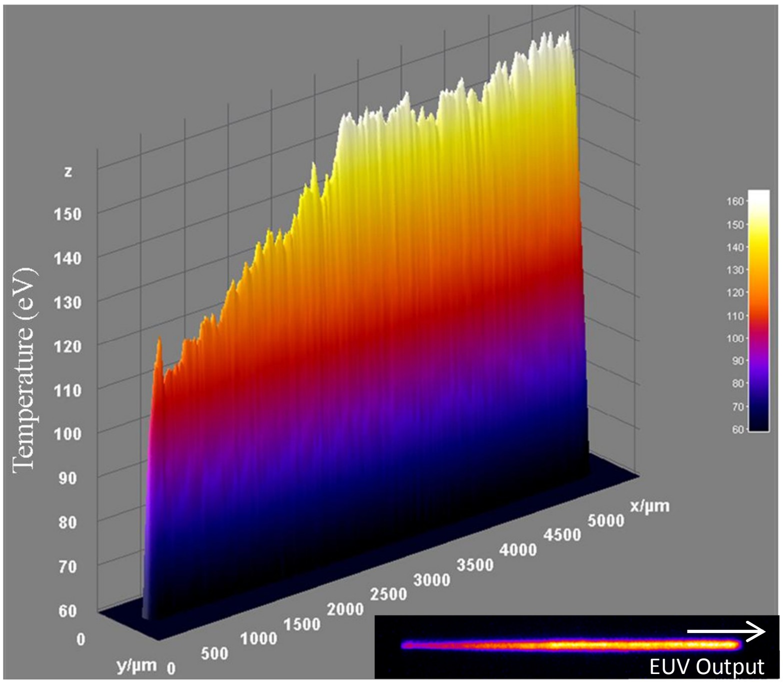

Figure 5.6 2D temperature profile for the Ge back-lighter.

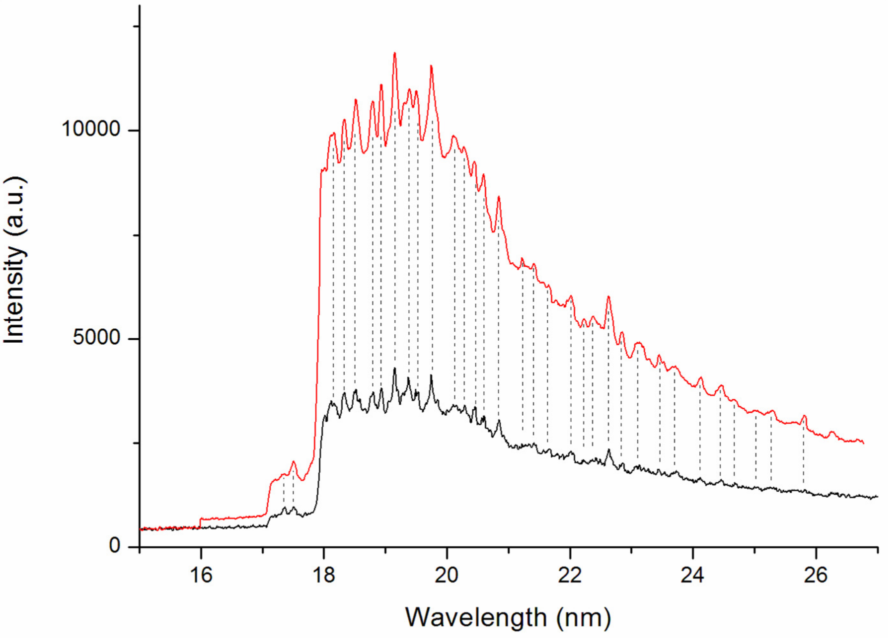

Figure 5.7 Ge spectrum as recorded by a flat field spectrometer. The red line demonstrates the spectrum originating from a back-lighter created using the two-pulse setup and the black line shows the spectrum from a back-lighter created using only the pre-pulse. The drop in intensity at 18nm is due to the CCD chip being partially covered with aluminium. The intensity drop at 17nm is the aluminium K edge.

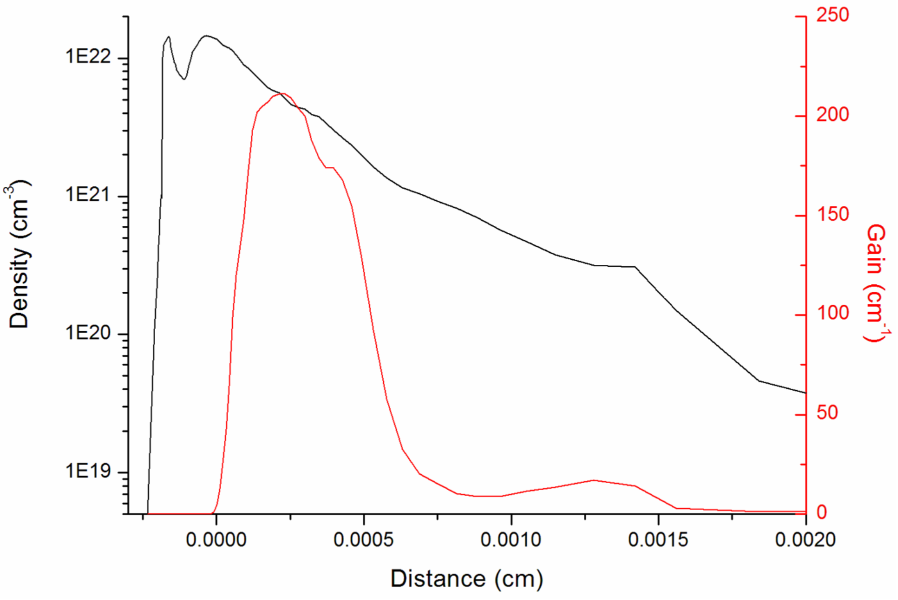

Figure 5.8 Density and small signal gain profile at the time of peak gain, t = 409 ps, 6 ps after the end of the main CPA pulse as simulated by Ehybrid for the conditions of the experiment.

Due to the short pulse duration (3ps) of the laser, the main pulse energy is largely coupled at higher densities, meaning any x-ray laser photons produced may be refracted out of the gain medium, reducing amplification. This effect has been reported previously by Smith et al. [98] and so has been investigated through simulations with Ehybrid (figure 5.8). Ehybrid demonstrates that the experiment produces the maximum gain within the Ge plasma at a density of 5×10^{21} cm^{-3}. The region of gain as simulated by Ehybrid has width $\Delta s \approx$ 4mm (figure 5.8) and has a peak gain value of G = 200cm^{-1}. Refraction at such high densities is significant. We can write that the refraction angle θ is related to the density scale length Δx and electron density n_e by [99]

$$\theta \approx \frac{L}{\Delta x}\frac{n_e}{2n_c} \tag{5.3.1}$$

where n_c is the x-ray laser critical density. Setting the maximum refraction angle $\theta = \Delta s/L$, gives that the x-ray laser propagation distance L in the gain region is such that

$$L \leq \sqrt{\Delta s \Delta x \frac{2n_c}{n_e}} \tag{5.3.2}$$

For Δs = 4μm, $n_e = 5\times10^{21}$ cm^{-3} and density gradient as shown in figure 5.8, we obtain $L \leq 100$mm, implying maximum gain length product $GL \leq 2$ which would not be observable.

5.4 Pinhole Camera

A pinhole camera was used to image the focal spot of the laser incident onto the iron layer in order to investigate the radial uniformity of the heating. The filtering used to cover the pinhole was 3μm thick Al foil, predominantly attenuating radiation with photon energies of < ~ 1keV. Figure 5.9(a) shows a single image from the pinhole camera and figure 5.9(b) shows a horizontal line out across the centre of the image. Figure 5.9 demonstrates the uniformity of the heating of the second CPA pulse in the radial direction.

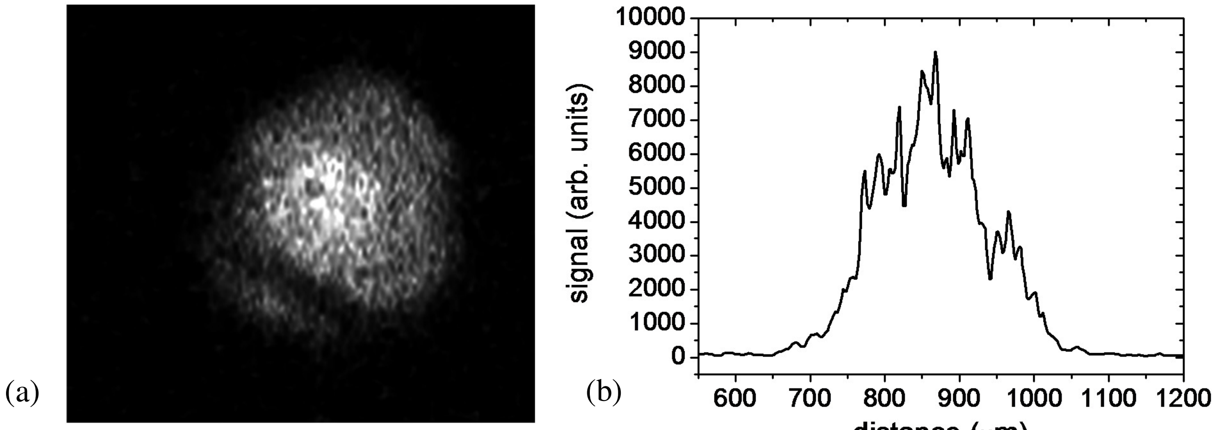

Figure 5.9 Pinhole camera image of the heated iron plasma (a) and a horizontal line out (b) across the centre of the image.

5.5 Transmission Results

The transmission of EUV light through the heated Fe foil was characterised using a flat-field spectrometer with an Andor CCD (Andor DX-435-BN). The flat-field spectrometer used a 1200 grooves/mm aberration corrected concave grating (Hitachi 001-0437) to spectrally disperse the EUV emission in the vertical direction on the CCD chip and provided spatial information in the horizontal direction. Filtering of 500nm aluminium was used to prevent visible light from entering the flat-field spectrometer. A sample image from the flat field spectrometer demonstrating the position of the opacity target, a fiducial wire and the heated target region is shown in figure 5.10.

The iron target was heated to a temperature of ~ 55eV as simulated using the 2D Lagrangian hydrodynamic code h2d [84] with a flux limiter of 0.1. Opacity data was generated using the IMP opacity code, and the SESAME [85] equation of state tables. The electron temperature and mass density radial profiles as simulated by h2d for different positions within target are shown in figure 5.11 (a) and 5.11 (b). These demonstrate a roughly uniform temperature profile in the radial direction, in agreement with the pinhole camera images, and densities ranging from 5 - 25% of solid density [91]. A steep temperature gradient is seen in the longitudinal direction through the target. Combining the hydrodynamic data from h2d with IMP code opacities (as in Chapter 4) a theoretical value for the transmission is generated for comparison with the experimental as is shown in figure 5.12.

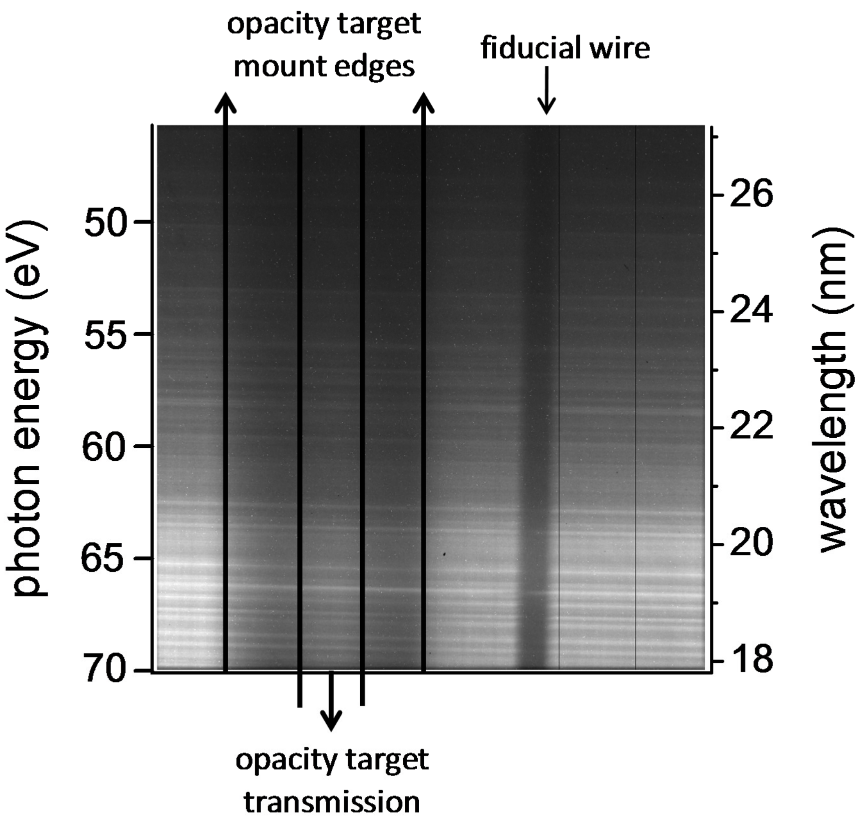

Figure 5.10 Sample image from the flat field spectrometer with spatial information in the horizontal direction and dispersed spectrally in the vertical direction. The position of the target and fiducial wire is shown, with the wavelength range and the transmission region of the opacity target.

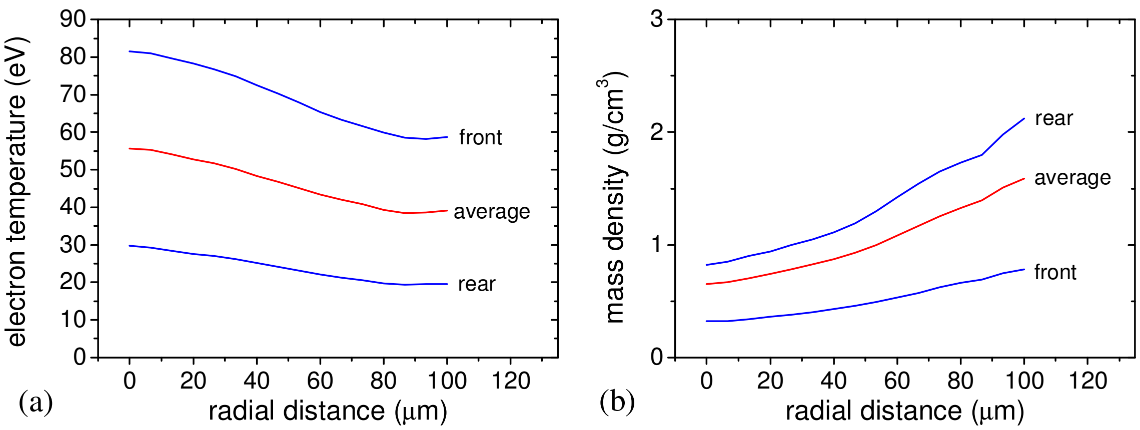

Figure 5.11 Electron temperature (a) and mass density (b) radial profiles as simulated using h2d for the iron target using a flux limiter of 0.1 and the experimental parameters outlined in the text.

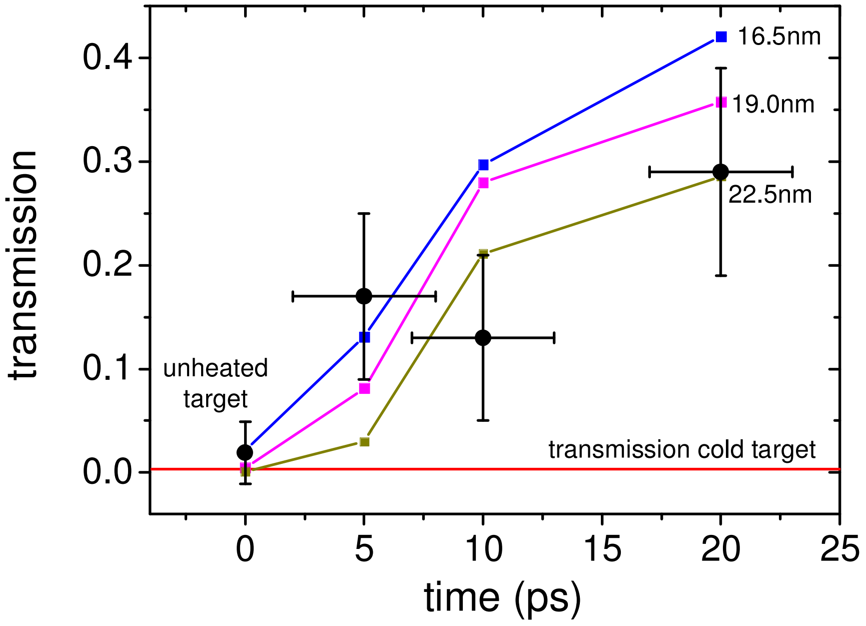

Figure 5.12 Experimental values (black circles) for the iron transmission at different time delays after the heating pulse at t = 0. Coloured squares represent h2d and IMP simulations of transmission for three different wavelengths.

5.6 Conclusion

This experiment has demonstrated how a plasma back-lighter can be well characterized through imaging the time and spectrally integrated emission profile of the plasma using a crossed-slit camera. By applying a detailed model of emission to the back-lighter images, a spatially dependant electron temperature profile can be inferred and used as a useful diagnostic of the plasma. Further study has shown the pulse duration of the main CPA pulse not to be ideal for lasing. Simulations using Ehybrid demonstrate that the short pulse duration and other conditions of the experiment result in energy coupling at higher densities where the increased refraction deflects lasing photons out of the gain region inhibiting amplification.

Experimental transmission results show some agreement with theoretical values calculated using h2d, IMP and SESAME codes. Although this experiment utilised targets tamped with plastic to inhibit plasma expansion, the target design was not optimal. Modelling using h2d demonstrates a steep temperature gradient in the longitudinal direction, decreasing the accuracy, as it is difficult to convert the measured transmission values into opacity measurements. Additional hydrodynamic simulations can be performed before the experiment in order to optimise the target design, allowing for more uniform plasma to be created.

6. Investigation of Radiation Hydrodynamics Using Titanium K_α Emission

6.1 Introduction

An instability which occurs when a lighter fluid supporting a heavier fluid undergoes acceleration in the direction of the heavier fluid is known as the Rayleigh-Taylor (RT) instability [100]. This effect is caused by acceleration mechanisms such as the acceleration due to gravity in ordinary fluids or the instability seen in inertial confinement fusion when accelerated plasma of a lower density compresses higher density plasma [101]. The Rayleigh-Taylor instability in plasmas is observed in astrophysics such as within the outer portion of a collapsed, massive star [102] or in the Crab Nebula [103]. The Rayleigh-Taylor instability in laser-produced plasmas has recently had to be taken into account in order to explain the expansion behaviour of thick (25 and 50μm) layered targets [104]. In the experiment of Lancaster et al [104], a plastic and copper layered target was found to be RT unstable as the copper layer cooled quickly via radiative emission and was therefore 'pushed' by the higher temperature, lower Z plastic, creating the instability.

The aim of this experiment is to investigate the RT instability in the configuration used by Lancaster et al [104], by imaging titanium K_α (4.51keV) emission through a RT unstable target. As in the Lancaster et al. experiment, plastic and copper layered targets were used to create the Rayleigh Taylor unstable plasma. The instability is seeded by introducing an approximately sinusoidal variation in thickness between the copper and plastic layers. In order to achieve approximately uniform heating across the target, a reduced mass target of dimensions 200μm × 200μm is used to encourage hot electron refluxing [105-107].

Myatt et al [106], demonstrated that in mass-limited targets ≥ 90% on the hot electron energy is converted into thermal energy within the target. Hot electron refluxing is due to strong space charge fields established as a hot electron leaves the target causing a significant number of electrons to return [108]. Mass limited targets encourage hot electron refluxing due to a minimal volume of cooler material to provide a cold return current, which neutralises the space charge fields. By measuring and imaging the transmission of Ti K_α radiation through the RT unstable target at different times, the evolution of the Rayleigh-Taylor instability can be investigated. Plasma conditions within the copper layer of the RT unstable target are calculated using PIC simulations (see section 6.4) and spectral modelling of He-like lines. This experiment demonstrates how knowledge of K_α back-lighters and plasma opacity can be used to investigate plasma phenomena.

6.2 Measuring the Rayleigh-Taylor Instability

6.2.1 The Rayleigh-Taylor Instability

The Rayleigh-Taylor instability occurs when a lighter fluid is accelerating a heavier fluid, causing instability between two layers. In some systems both fluids are acted upon by gravity where the force experienced by the heavier fluid is higher causing the heavier fluid to be pulled downwards, displacing the lighter fluid. The instability begins as slight irregularities between the planar layers which increase in time, creating ‘finger-like’ columns between the immiscible fluids [102].

The process described above evolves in the same manner in laser produced plasmas, where the acceleration force is thermodynamically driven. A sinusoidal interface, with wave number k, between two layers will grow with a rate proportional to $\exp(\gamma t)$ [109]. The growth rate, γ, is a function of the acceleration, g, the wave number of the oscillation,

k, and the properties of the target material which enters the growth equation given in 6.2.1 through the Atwood number, A given by equation 6.2.2 [110].

$$\gamma = \sqrt{Agk} \tag{6.2.1}$$

where,

$$A = \frac{\rho_h - \rho_l}{\rho_h + \rho_l} \tag{6.2.2}$$

and ρ_h and ρ_l are the densities of the heavier and lighter fluids respectively.

6.2.2 Fast Fourier Transform Analysis

In order to detect variations in transmission across the back lit target, Fourier analysis can be used on the image from a 2D crystal imager (described in section 6.3.2). Fourier analysis can be used to convert an image from the spatial domain into the frequency domain and is used to detect repetitive signals within an image (see figure 6.1). The Fourier transform analysis used to examine the Rayleigh-Taylor growth of a sinusoidal variation of copper and plastic is introduced and tested in this section.

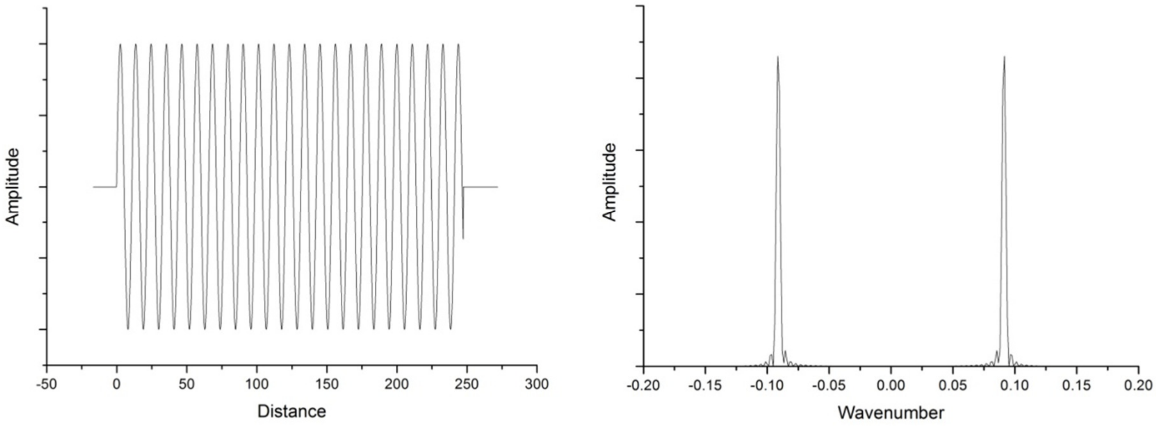

Figure 6.1 (a) Sinusoidal oscillation over an arbitrary distance with a wavelength of $\lambda = 11$. (b) FFT of oscillation showing asymmetric delta peaks corresponding to the wave number of $k = 0.09$.

Mathematically, a discrete Fourier Transform is given by:

$$F(k) = \sum_{k=0}^{N-1} f(n) \exp\left(-\frac{i2\pi kn}{N}\right) \tag{6.2.3}$$

where *n* is the index, *N* is the number of input data points, *k* is the wave number of the perturbation and *f(n)* is the signal. The Fast Fourier Transforms in this chapter are calculated using Origin software 6.1 [111]. A sample signal over an arbitrary distance is shown in figure 6.1 (a) with its corresponding Fourier Transform shown in figure 6.1 (b). It is seen that the sinusoidal variation with distance produces two asymmetrical delta peaks at $k = \pm 0.09$ which correspond to the wavelength of oscillation $\lambda = 11$.

6.3 Experimental Set-up

The K_α back-lighter was created using a pulse from the VULCAN Nd:Glass laser system at the Rutherford Appleton Laboratory to irradiate a titanium target of thickness 25μm. A CPA pulse of duration 2ps and energy of 100J was focussed to a spot ~ 200μm in diameter, using an f/3 parabolic mirror, giving an irradiance of ~ 2×10^{17} W cm^{-2}. A second (chirped pulse amplification or CPA) pulse of 3ps duration with energy of 300J was focused into a spot ~ 10μm in diameter (~ 1×10^{20} W cm^{-2}) onto the RT unstable target described in the following section. The delay between the heating pulse and the back-lighting pulse was varied between 50 and 200ps to study the evolution of the RT instability. A schematic for the experimental layout showing the relative positions of the targets, the 2D crystal imager and the HOPG spectrometer is shown in figure 6.2.

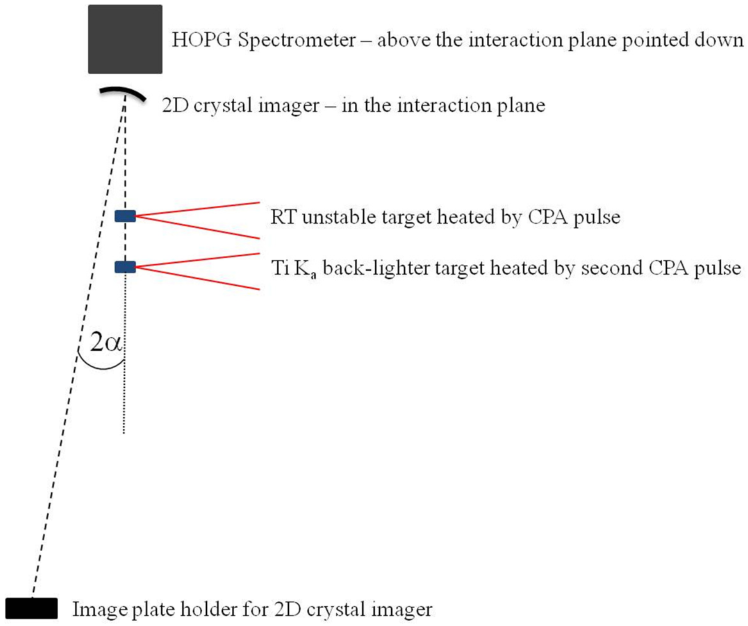

Figure 6.2 Experimental schematic showing the relative positions of the diagnostics where $\alpha = 90 - \theta_B$ and θ_B is the Bragg angle for Ti K_α.

6.3.1 Target Design

The RT unstable targets comprised 25μm thick plastic covered with a 2μm thick copper layer with a sinusoidal oscillation of thickness with amplitude 300nm and wavelength 30μm at the interface between the two layers (see figure 6.3). The oscillation between the layers varies the copper thickness by 600nm from peak to trough, thus varying the transmission of K_α photons through the target as shown in figure 6.4. The sinusoidal oscillation between the two layers seeds the Rayleigh-Taylor instability which grows on a timescale longer than the heating pulse when irradiated by a laser pulse as also illustrated in figure 6.3. It is expected that hot electron refluxing will approximately uniformly heat the target in the direction of the laser. As the instability grows, the change in transmission across the target increases and by varying the time delay between the heating pulse and the pulse used to generate the Ti K_α back-lighter, the evolution of the instability can be investigated. The expected variation in transmission across a cold target is shown in figure 6.4.

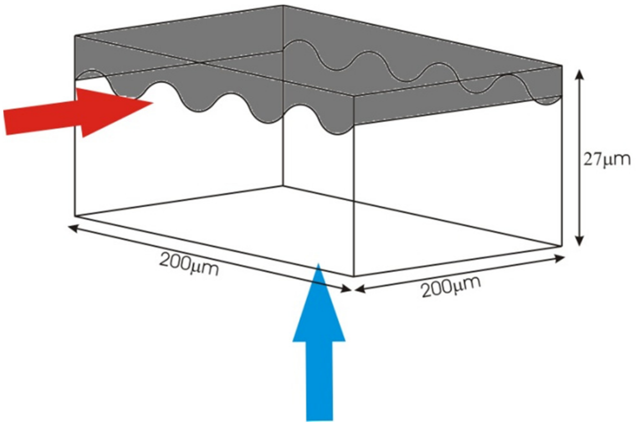

Figure 6.3 Rayleigh-Taylor unstable target design. Copper (dark region) of thickness ~ 2μm is coated onto plastic (light region) of thickness ~ 25μm with a sinusoidally oscillating interface of amplitude 300nm and wavelength of 30μm. Red arrow indicates direction of heating laser and blue arrow indicates direction of Ti K$_\alpha$ back-lighter.

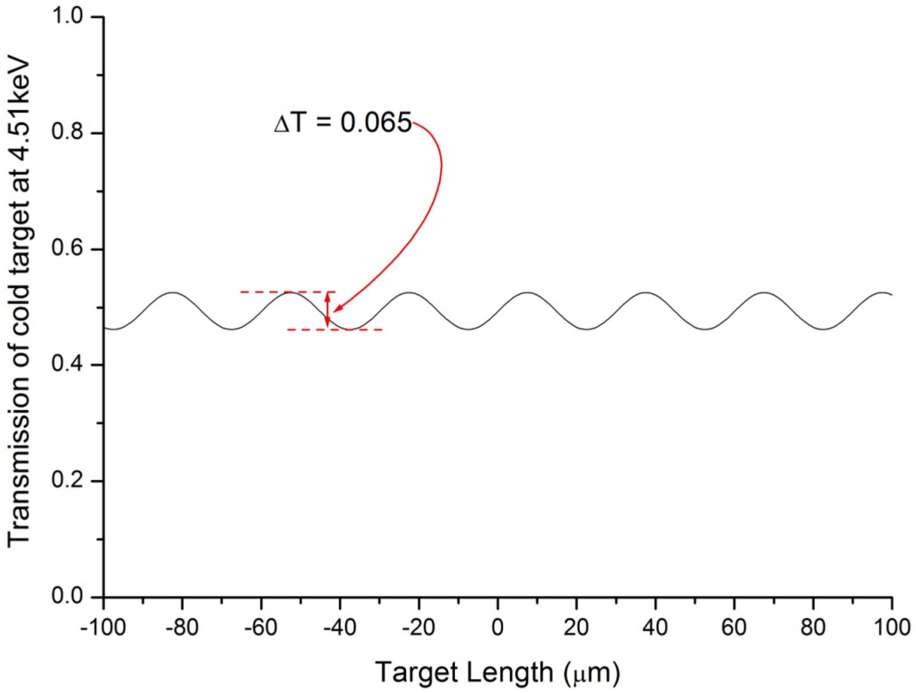

Figure 6.4 Variation in transmission across a cold RT target and the corresponding change in CCD signal across the target as the back-lighter passes through the varying thickness of copper. The theoretical change in transmission, *ΔT*, is calculated to be *ΔT* = 0.065 for a cold target.

The targets are prepared as 200 × 200 μm squares supported on a 50 μm wire. The sinusoidal oscillations run horizontally, parallel to the heating CPA pulse which is incident onto the front surface as shown in figure 6.3. The laser pulse heats the two regions simultaneously to the same temperature by hot electron propagation and refluxing. The denser copper layer cools quicker than the plastic layer due to more effective radiative cooling (see the Z dependence on radiation emission discussion in section 2.3). The lighter and hotter plastic can then accelerate the denser, cooler copper layer, enhanced by the initial perturbations, creating the Rayleigh-Taylor instability.

The Ti K_α back-lighter passes through the RT unstable target in the direction perpendicular to the laser axis (figure 6.3). As the instability evolves, and the 'finger-like' columns emerge, the copper thickness can be expected to increase and decrease in different areas of the target, changing the transmission and thus the amplitude of the oscillation. By imaging the back-lighter at the RT target position at different times, the evolution of the instability is investigated.

6.3.2 2D K_α Imager

A spherically bent SiO_2 quartz (2023) crystal with a radius of curvature of 38cm was used to image titanium K_α radiation generated from the back-lighter foil after passing through the RT unstable target onto an image plate. The crystal operated at an angle of 1.5° from target normal and had a target to crystal distance of 21cm and a crystal to image plate distance of 297cm, giving a magnification of ≈ 14. A spherically curved crystal disperses x-rays according to Bragg's law with the curvature of the crystal acting as a lens, focussing a high resolution image of the back-lighter onto an image plate filtered with 12μm aluminium foil.

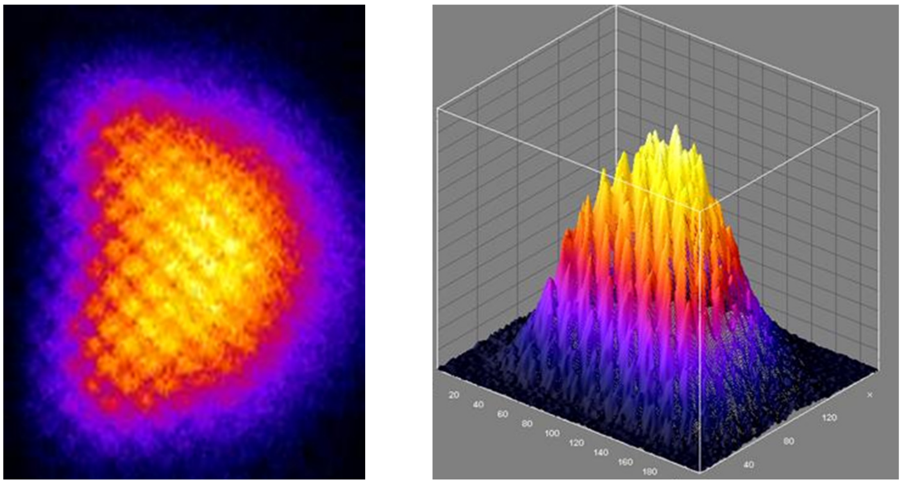

Figure 6.5 Image (a) and a 2D intensity plot (b) of a copper mesh with 5μm wires and 40μm spacing using Ti K_α emission as a back-lighter and a 2D spherical K_α imaging crystal as a collecting optic.

In order to ascertain the resolution of the K_α imaging system, a copper mesh with 5μm copper wires with 40μm spacing was placed at the RT target position and imaged (see figure 6.5). The modulation transfer function (MTF) of an optical system is a measure of the ability of the system to transfer contrast from the sample to the image plane and is a function of spatial frequency. The MTF as a function of spatial frequency, φ, is defined as [112],

$$MTF(\varphi) = \frac{M_{image}(\varphi)}{M_{object}}, \tag{6.3.1}$$

where M is the modulation (contrast) of the image or object, defined by [112],

$$M = \frac{I_{max} - I_{min}}{I_{max} + I_{min}}, \tag{6.3.2}$$

where I_{max} and I_{min} are the image/object irradiances (see figure 6.6). For example, a system of periodic strips of black and white spatial profiles, such as shown in figure 6.6(a), would lose contrast when imaged due to the optical system being imperfect, as shown in figure 6.6(b). The MTF is a measure of this loss of contrast as a function of spatial frequency, i.e. the spacing between the lines in figure 6.6(a).

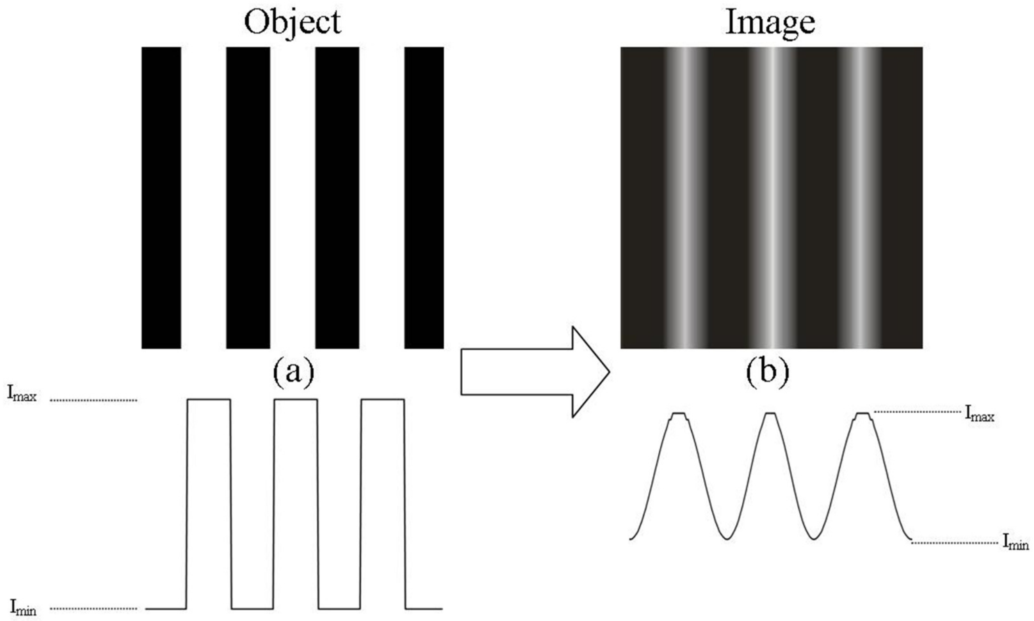

Figure 6.6 (a) Object of periodic strips of black and white (above) and associated lineout (below) and (b) image of object (above) and associated lineout (below).

Taking into account the transmission of 5μm of copper at 4.51keV [62], a fast Fourier transform (FFT) of an ideal mesh lineout similar to that shown in figure 6.6(a) is calculated and compared to the FFT of the experimental image of the mesh as shown in figure 6.7. The MTF for this system as a function of spatial frequency is shown in figure 6.8 and shows that the MTF for the initial perturbation wave number of 0.033 μm^{-1} (λ = 30 μm) is 0.88 ± 0.02.

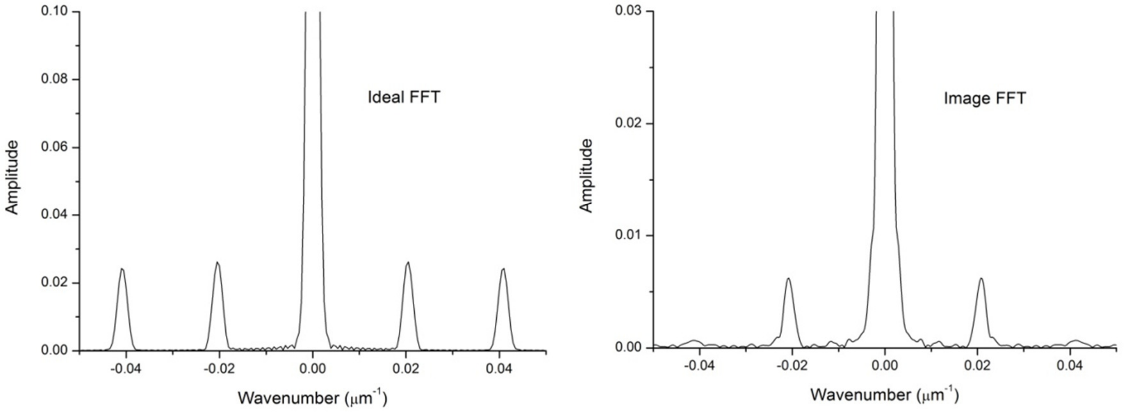

Figure 6.7 Fast Fourier transform of an ideal mesh compared with an FFT of a lineout from the mesh image shown in figure 6.5.

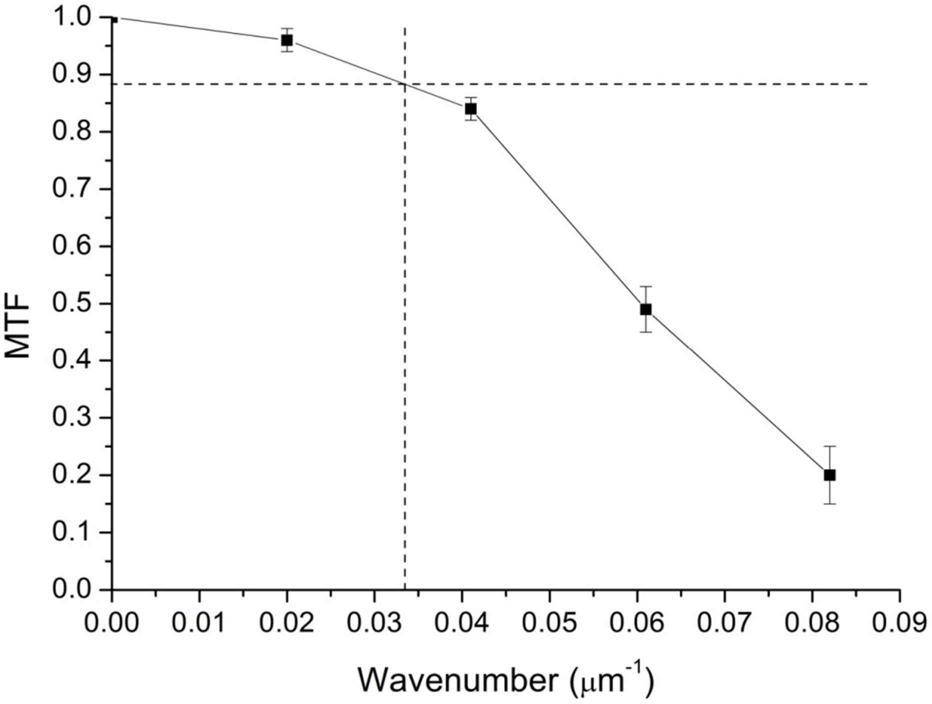

Figure 6.8 Modulation transfer function for the 2D crystal K_α imaging system as determined from the FFT of the mesh image shown in figure 6.5

6.3.3 HOPG Spectrometer

A HOPG (highly ordered pyrolytic graphite) spectrometer was positioned above the target plane aligned pointing downward at the RT unstable target. The HOPG crystal with 2d = 6.71Å, was optimised to disperse copper K_α photons onto an image plate filtered by 12μm aluminium foil. The HOPG crystal is a mosaic, layered polycrystalline with a well-defined layer spacing and high stability under a range of environmental conditions and is ideal for dispersing copper K_α radiation at 1.54Å.

Using dynamical crystal theory, a rocking curve can be deduced and describes the diffracting properties of a crystal. The rocking curve of a HOPG crystal is characterised by a Gaussian rocking curve due to the random nature of the mosaicity, of width $W = 0.4°$. The peak reflectivity and the integrated reflectivity are $P = 0.29$ and $R = 0.41$, respectively [113] for Cu K_α photons at 4.51keV with a Bragg angle of $\theta_B = 13.3°$. A sample rocking curve is shown in figure 6.9.

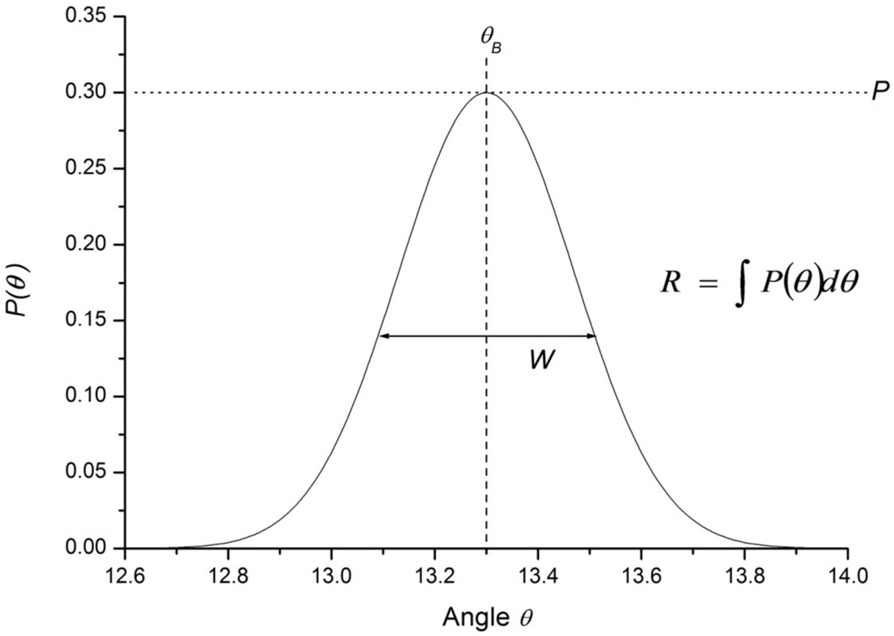

Figure 6.9 Sample rocking curve for a HOPG crystal [113].

6.4 LPIC++

The code to be used in this work is LPIC++ [49], a one spatial dimension, relativistic, electromagnetic PIC code, written in C++ and developed by Roland Lichters, at the Max-Planck-Institut für Quantenoptik during his PhD thesis [114]. The one spatial dimension of the code means that the integration of Maxwell's equations involves integrating the transverse fields $E_{y,z}$ and $B_{y,z}$ and the longitudinal field E_x [49] and uses the algorithms of Birdsall and Langdon [50] and Villasenor and Bunemann [51]. The code has considerable flexibility, largely due to the clear program structure and convenient method of varying the input data. All of the input parameters are described by dimensionless quantities. The user can specify up to two laser pulses incident onto the target, one front side and one at the rear, defined in terms of polarization, shape, rise time and duration, and the dimensionless field amplitude, a_0. Collisions between ions, electrons and free electrons are modelled assuming the Coulombic interaction.

The field amplitude for use in PIC code simulations is defined by [114]

$$a_0 = \frac{eE_0}{m_e \omega c} \qquad (6.4.1)$$

which can be related to the intensity and wavelength of the laser by [114]

$$I\lambda^2 = a_0^2 \times 1.37 \times 10^{18}\ W\ \mu m^2\ cm^{-2} \qquad (6.4.2)$$

where e and m_e are the electron charge and mass, E_0 is the amplitude of the laser electric field and ω and λ are frequency and wavelength, respectively, of the laser. As the PIC code does not consider atomic physics, which has a dependence on photon frequency, only a_0 needs to be specified and not the laser wavelength. The rise time and duration of the laser pulse incident onto the target is defined in terms of laser periods, the polarisation can be set to s-, p-, or circular and the temporal shape of the pulse can be described by linear, sine, or sine^2 edges.

In addition to specifying the parameters of the incident laser pulse(s), the target parameters and simulation time must be defined. The length of the simulation time can be longer or shorter than the duration of the laser pulse, and is again specified by a number of laser periods. The target parameters are specified by an arbitrary number of cells, whose size is defined by the parameter, “cells per wavelength” (laboratory frame) which states how many cells equals a distance of one wavelength. The user can then go on to specify the total number of cells, the number of cells in the linear density ramp and the number of cells available as vacuum. The density is specified by defining the maximum ion density over the critical density (n_i/n_c).

The particle species (electrons and ions) are described by a maximum number of macro-particles per cell and by the parameter ‘v_{therm}’ which represents the initial temperature of the plasma in terms of v/c, where v is the velocity of the particle and can be calculated by

$$\frac{1}{2}m\left(v_x^2 + v_y^2 + v_z^2\right) = \frac{3}{2}kT \qquad (6.4.3)$$

where $v_x = v_y = v_z = v$ and $v_{therm} = v/c$. The ions have two further parameters to specify, one is the ionisation, z, and the second is the mass of the ion in terms of m_i/m_e which defines the element under consideration.

6.4.1 Obliquely Incident Laser Pulses

When examining the interaction of a laser pulse with plasma, the angle of incidence is often an important factor, especially in the case of hot electron generation (see section 2.1.3). As LPIC++ operates in one spatial dimension, it would not normally lend itself to oblique angles of incidence. However, a Lorentz transformation can be used to bring the laser pulse normal to the target surface again in a different frame (figure 6.10). By introducing a frame velocity $^{v}/_{c} = \sin\alpha$, in the y direction, where α is the angle of incidence, the laser is now firing normally into streaming plasma in frame M as opposed to oblique incidence in the laboratory frame. This frame velocity is represented in the code by additional ion and electron currents and follows Bourdier's method [115]. This means the laser wavelength and frequency are Doppler shifted in the moving frame M by [49],

$$\begin{aligned} \lambda &= \frac{\lambda_0}{\cos\alpha} \\ \omega &= \omega_0 \cos\alpha \end{aligned} \tag{6.4.4}$$

where the λ_0 and ω_0 are the wavelength and frequency in the laboratory frame respectively.

6.4.2 LPIC++ Output

LPIC++ provides a variety of output and the user specifies what is required. The main output of interest to this work is that of the electron velocity distribution. A small program has been written in Fortran by the author to convert the electron velocity distribution file produced by LPIC++ into an electron energy spectrum (see figure 6.12), in order to determine the hot electron temperature.

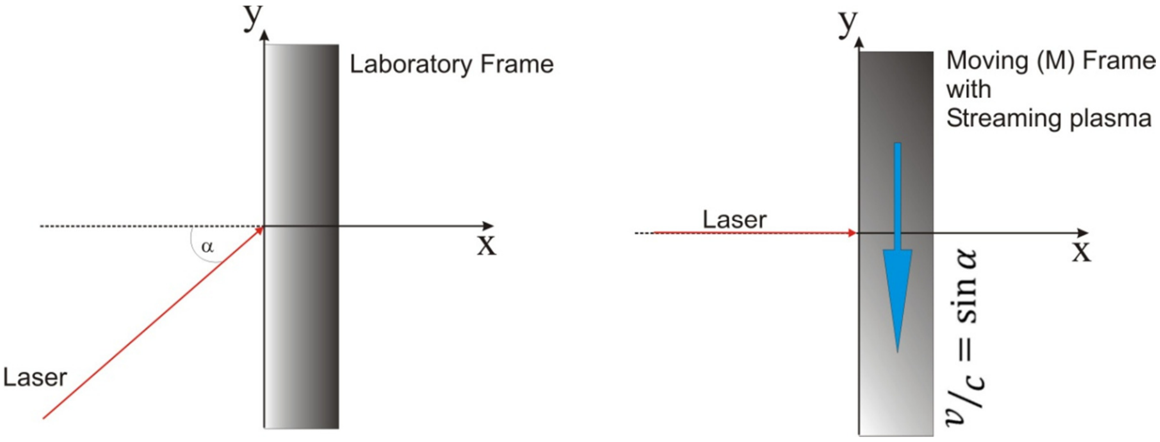

Figure 6.10 Lorentz transformation to account for an oblique angle of incidence.

6.5 HOPG Spectrometer Results

The HOPG spectrometer was used to investigate the K_α and He-like spectrum of the copper. Figure 6.11 shows the spectrum containing the Cu K_α line (8.05 keV), He-like intercombination (x,y - 8.35 keV) and resonance (w - 8.39 keV) lines and Li-like satellites (e,f,u) around 8.30 keV. The standard letter designation is as defined by Gabriel [81].

6.5.1 K_α Photon Number

The particle-in-cell code, LPIC++, described in detail in section 6.4, was used to simulate the laser interaction with a copper target in order to calculate the hot electron temperature. The simulated hot electron energy spectrum is shown in figure 6.12 and indicates a hot electron temperature of T_h = 65 keV and a hot electron fraction of f_h = 0.28. The parameters used for this simulation were a_0 = 10.33, angle of incidence = 20.00°, pulse duration = 848 periods (corresponding to 3ps) with a rise time of 60 periods, n_i/n_c = 100 and 2000 cells of plasma (500 cells per laser wavelength) with an initial steep ramp of 20 cells.

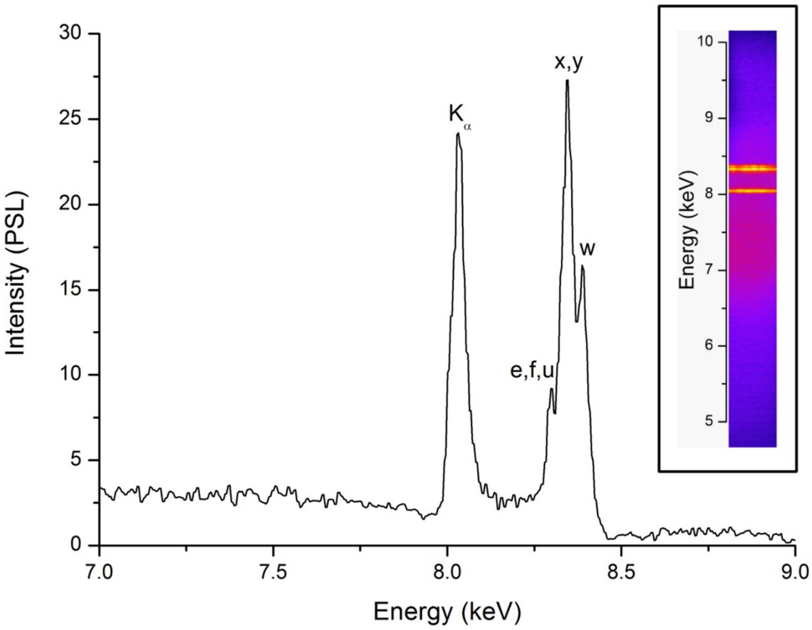

Figure 6.11 Calibrated spectrum obtained from HOPG crystal spectrometer showing the Cu K$_\alpha$ line, He-like resonance line (w), He-like intercombination line (x,y) and Li-like dielectronic recombination satellites (e,f,u). Letter designation is as defined by Gabriel [81]. Insert is an image of the raw HOPG spectrum.

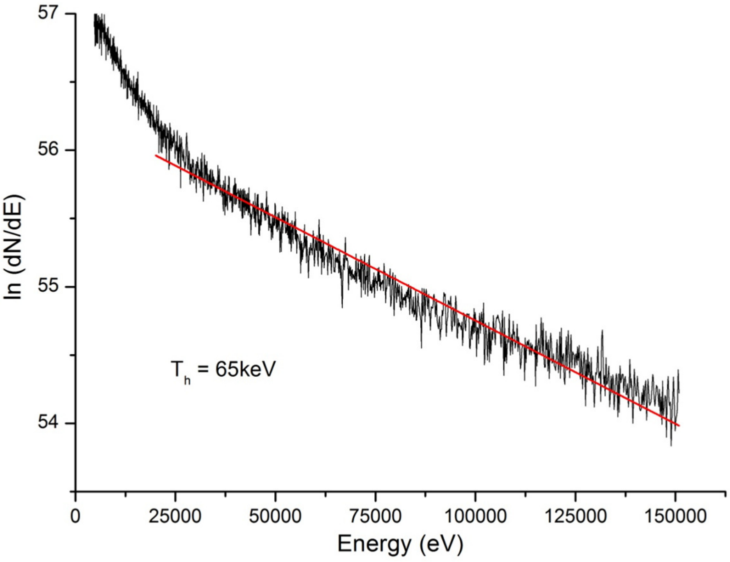

Figure 6.12 Hot electron energy spectrum simulated by LPIC++ using the laser parameters defined in text. A hot electron temperature of 65keV is calculated where the fraction of hot electrons (f_h) compared with the total number of electrons is $f_h = 0.28$.

The values T_h = 65 keV and f_h = 0.28, as calculated by LPIC++ are used in a model of K_α photon production as described in previous work [116,117]. It is assumed that refluxing of hot electrons ensures that all of their energy is dumped in the target.

K_α production in a refluxing target can be described by [116]:

$$N_{K\alpha} = N_h n_i \omega_K \int_0^\infty f(E_0)\, dE_0 \int_0^{E_0} \sigma_K(E) \left(\frac{dE}{ds}\right)^{-1} dE \tag{6.5.1}$$

where N_h is the number of hot electrons, n_i is the ion density, ω_K is the K_α fluorescence yield for copper, $f(E_0)$ is the initial normalised electron distribution, $\sigma_K(E)$ is the K-shell ionisation cross-section and (dE/ds) is the electron stopping power. For copper, $\omega_K = 0.44$ [118], $n_i = 8.4 \times 10^{22}$ cm^{-3}, and dE/ds can be approximated by $dE/ds \cong aE^{-\alpha}$ [119].

Using electron stopping power data from NIST [120], the stopping power can be calculated for $E_0 < 100$ keV by:

$$\frac{dE}{ds} = 0.52 E_0^{-0.7} \tag{6.5.2}$$

where E_0 is the initial electron energy. The total number of hot electrons is determined by incorporating the fractional abundance of hot electrons from the LPIC simulations into a deflagration model of laser ablation [121]. The deflagration model calculates the mass ablation rate by assuming the laser energy absorption occurs at the critical surface and is given by [121]

$$\frac{dm}{dt} = 136 \rho_c^{2/3} I_a^{1/3} \tag{6.5.3}$$

where ρ_c is the mass density at the critical surface and I_a is the absorbed laser intensity. The fractional laser absorption at the critical surface due to the excitation of an electrostatic wave can be deduced by examining the resonance function, $\phi(\tau)$, which describes the strength of the absorption as a function of incident angle and plasma scale length [24]. The fractional absorption, f_a, of the laser is given by [24],

$$f_a = \frac{\emptyset(\tau)^2}{2} \tag{6.5.4}$$

where

$$\emptyset(\tau) = 2.3\tau \exp\left(-\frac{2\tau^3}{3}\right), \tag{6.5.5}$$

$$\tau = \left(\frac{\omega L}{c}\right)^{1/3} \sin\theta \ , \tag{6.5.6}$$

ω is the laser frequency, L is the scale length of the plasma and θ is the angle of incidence. Using the parameters of this experiment and estimating the scale length of the plasma from the ion sound speed, $c_s \cong (ZkT/m_i)^{1/2}$, gives a fractional absorption of $f_a = 0.61$ and thus $I_a = 6.1 \times 10^{19}$ W cm^{-2} and $dm/dt = 1.26 \times 10^{7}$ g cm^{-2} s^{-1}. Using this mass ablation rate, the total mass ablated during the laser pulse is $m = 1.47 \times 10^{-11}$ g or total number of copper ions, $N_i = 1.39 \times 10^{11}$ ($N_e = ZN_i = 4.04 \times 10^{12}$) which gives the total number of hot electrons, $N_h = 1.13 \times 10^{12}$.

The K-shell ionisation cross-section is calculated using a Relativistic Binary Encounter Bethe (RBEB) model [122], and is given by,

$$\sigma_K = \frac{4\pi a_0^2 \alpha^4 N}{(\beta_t^2 + \beta_u^2 + \beta_b^2) 2b'} \left\{ \frac{1}{2}\left[\ln\left(\frac{\beta_t^2}{1-\beta_t^2}\right) - \beta_t^2 - \ln(2b')\right]\left(1 - \frac{1}{t^2}\right) + 1 - \frac{1}{t} - \frac{\ln(t)}{t+1}\,\frac{1+2t'}{(1+t'/2)^2} + \frac{b'^2}{(1+t'/2)^2}\,\frac{t-1}{2} \right\} \tag{6.5.7}$$

where

$$\beta_t = {}^{v_t}/_{c} \ , \qquad \beta_t^2 = 1 - \frac{1}{(1 + {}^{t'}/_{2})^2} \ , \qquad t' = {}^{T}/_{mc^2} \ ,$$

$$\beta_b = {}^{v_b}\!/_{c}\ , \qquad \beta_b^2 = 1 - \frac{1}{(1 + {}^{b'}\!/_{2})^2}\ , \qquad b' = {}^{B}\!/_{mc^2}\ ,$$

and

$$\beta_u = {}^{v_u}\!/_{c}\ , \qquad \beta_u^2 = 1 - \frac{1}{(1 + {}^{u'}\!/_{2})^2}\ , \qquad u' = {}^{U}\!/_{mc^2}\ .$$

The terms used in the RBEB model are as follows; a_o is the Bohr radius, α is the fine structure constant, N is the occupation number ($N = 2$ for a full K-shell), T is the kinetic energy of the incident electron, B is the binding energy of the K-shell electron (B = 8.980keV for copper [122]), U is the kinetic energy of the K-shell electron (U = 11.32keV for copper [122]) and the v terms are the speeds of electrons with kinetic energies of T, B or U depending on the subscript. Figure 6.13 shows the dependence of the K-shell ionisation cross-section as a function of electron energy as calculated using equation 6.5.7 and agrees well with previously published work [122,123].

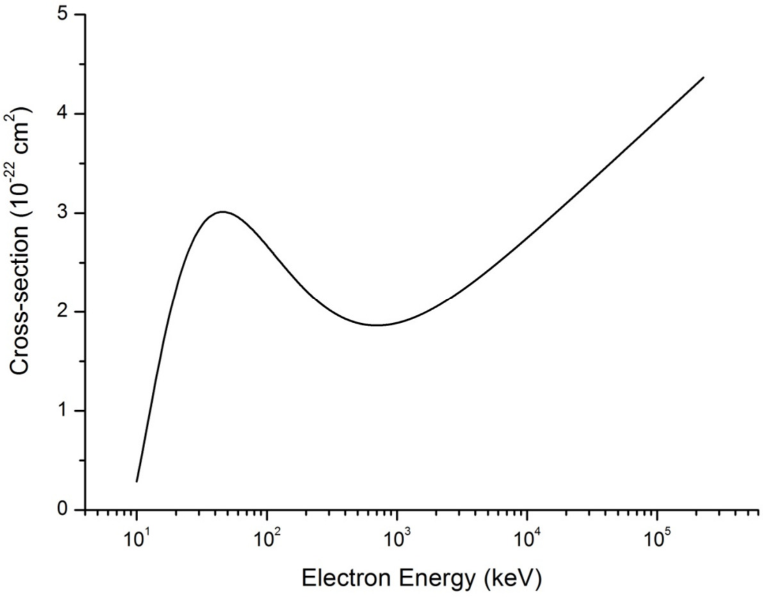

Figure 6.13 K-shell ionisation cross section as a function of electron energy as calculated using the RBEB model.

By numerically integrating $\int_0^{E_0} \sigma_K(E) \left(\frac{dE}{ds}\right)^{-1} dE$ and using the relationship denoted in equation 6.5.1, the total number of K_α photon produced is $N_{K\alpha} = 2.15 \times 10^{10}$ photons over 4π steradians. Using the rocking curve of the HOPG crystal to define the crystal distance in the spectrally dispersive direction and the width of the crystal in the spatial direction, a solid angle of detection of $\Omega = 0.00776$ sr is calculated for the spectrometer. Taking into account, this solid angle, the reflectivity of the HOPG crystal, and the transmission of the 12.5μm aluminium filter, the predicted $N_{K\alpha}$ detected at the image plate is $N_{K\alpha} = 4.8 \times 10^6$ photons.

The K_α line on the raw spectrum as shown on the insert in figure 6.11 is integrated to obtain a total number of photostimulated luminescence (PSL) counts. Using a known conversion of PSL counts to photon number [124], the total number of K_α photons detected is calculated to be $N_{K\alpha(IP)} = (5 \pm 1) \times 10^6$ photons, in excellent agreement with the theoretical result. This measurement gives confidence to the values of $T_h = 65$keV and $f = 0.28$.

6.5.2 FLYCHK Simulations

The spectral modelling code FLYCHK [44], was used to simulate the He-like lines generated in the copper plasma. Using the values of $T_h = 65$ keV and $f = 0.28$ and varying the thermal temperature, T_c, and the electron density, n_e, the dependence of the line ratios upon these parameters is shown in figure 6.14. A heated supercritical density ($n_e > 10^{21}$ cm^{-3}) is required to reproduce the observed line ratios, indicating significant heating beyond the critical surface. The FLYCHK simulations indicate a temperature of between $T_c = 300 - 400$ eV and a density of $n_e = 10^{22} - 10^{23}$ cm^{-3}. The high density reinforces the idea of hot electron heating within the target as it is above the critical density of the laser. As the recorded spectra are time averaged, the instantaneous peak in emission will be close at higher density.

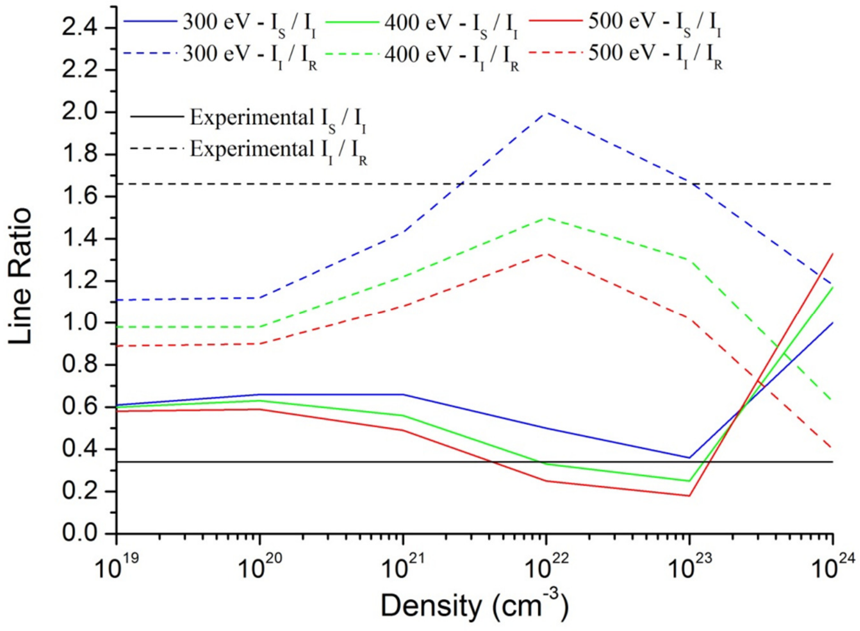

Figure 6.14 Dependence of spectral line ratios on density and thermal temperature (T_c) as simulated using FLYCHK with the fixed parameters of T_h = 65keV and f = 0.28. The line ratios shown are the Li-like satellites to the intercombination line (I_S/I_I – solid lines), and the intercombination line to the resonance line (I_I/I_R – dashed lines).

6.5 2D K$_\alpha$ Imager Results

A sample image of the Ti K$_\alpha$ back-lighter passing through the RT unstable target is shown in figure 6.15. With the conditions discussed in section 6.3 and the target design in 6.3.1, it was found that the contrast between peaks and troughs in the back-lighter transmission was not sufficient to allow for 2D Fourier analysis. As a result the back-lighter signal over a section of the images was integrated along the direction of the grooves (see figure 6.15) so as to enhance the contrast of any perturbations present. The section of image selected for the integration is behind the laser interaction region, the size of which is shown in figure 6.15. A 1D Fourier transform is then performed on the resulting line out in order to analyse any spatial frequencies present.

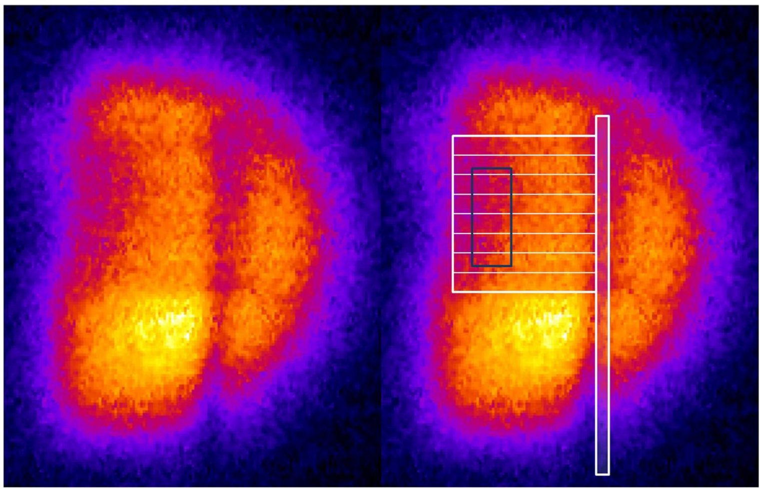

Figure 6.15 Sample images from 2D spherical crystal imager, left shows Ti K_α back-lighter passing through the RT unstable target, right shows the same image with a schematic of the target overlaid indicating the perturbation orientation. The delay between the heating pulse and the pulse to generate the Ti K_α back-lighter is 150ps and the heating laser is incident on the left hand side of the target. The blue box demonstrates the integration area (integration is parallel to the oscillation) for FFT analysis.

The portion of the back-lighter in each image which does not pass through the RT target is used to calculate a mean PSL value for the initial back-lighter intensity which is then used to normalise the images with the original back-lighter intensity, $I_0 = 1$. The amplitude of the Fourier transform then represents the amplitude of the oscillation in terms of change in transmission, where $\Delta T = 2 \times$ FFT amplitude and ΔT is defined in figure 6.4. Figure 6.16 shows an example of an FFT of the theoretical transmission plot shown in figure 6.4. As the sinusoidal function shown in figure 6.4 is restricted to a finite space (i.e. over the target length) the function must be thought of as a top hat function multiplied by a sine function. The resulting FFT shown in figure 6.16 is a sinc function originating from the top hat component convolved with a pair of antisymmetrical delta functions corresponding to the frequency and amplitude of the sinusoidal oscillation. By normalising the Ti K_α images taken at different time intervals, integrating over a section of the target and performing a 1D FFT on the resulting line out, the evolution of the perturbations within the target can be investigated.

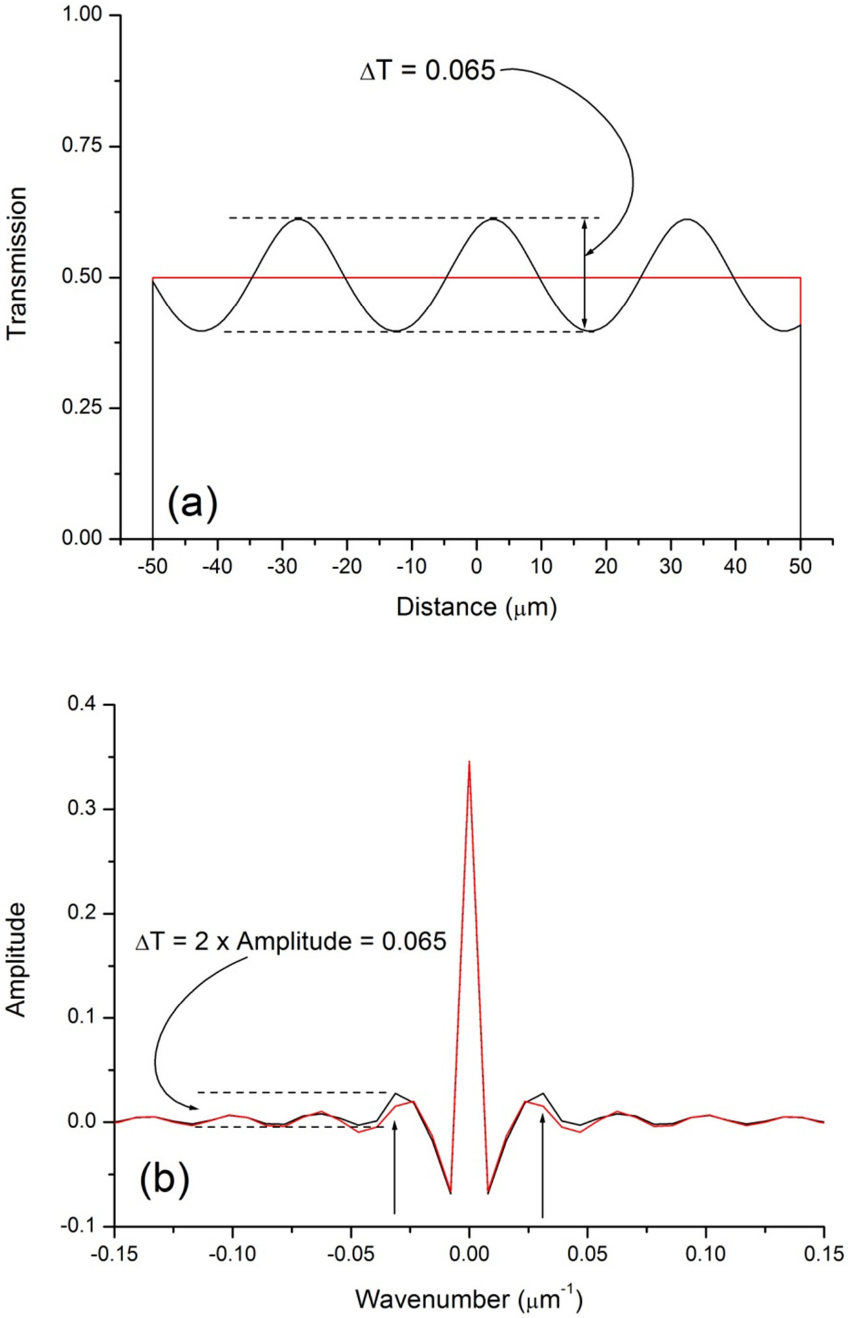

Figure 6.16 Theoretical target cross-sections (a) showing a planar target (red) and a target with sinusoidal perturbation (black) and the corresponding FFT (b) showing a sinc function and indicating the delta function due to the perturbation frequency (arrows show position). The value *ΔT* is twice the amplitude of the oscillation as shown in figure 6.4 and represents the change in transmission from peak to trough.

6.5.1 Fast Fourier Transform Results

The delay between the RT target heating pulse and the pulse used to generate the Ti K_α back-lighter was varied to probe the instability at the different time intervals of 75, 100, 150 and 200ps. For comparison purposes, the Ti K_α back-lighter was used to back-light a cold RT unstable target, the results of which are shown in figure 6.17 and are found to agree with the theoretical modelling for a cold target. The cold perturbation wavelength was calculated to be $\lambda = (24.5 \pm 6.1)$ μm and the change in transmission was $\Delta T = (0.062 \pm 0.007)$ in agreement with the information supplied by the target manufacturer ($\lambda = 30$μm with $\Delta T = 0.065$ arising from the thickness modulation). The FFTs for each of the four time delays are shown in figure 6.18, the perturbation wavelengths and ΔT values are summarised in figure 6.19.

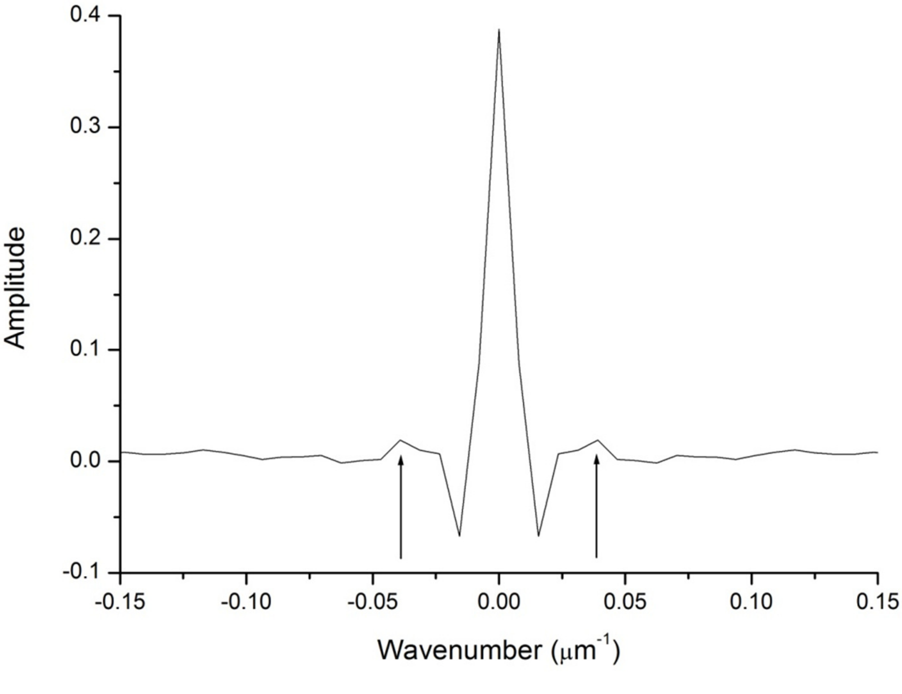

Figure 6.17 FFT of the Ti K_α image back-lighting a cold RT unstable target. The frequency peak due to the target oscillation is shown (arrows) and corresponds to $\Delta T = (0.062 \pm 0.007)$ and $\lambda = (24.5 \pm 6.1)$ μm.

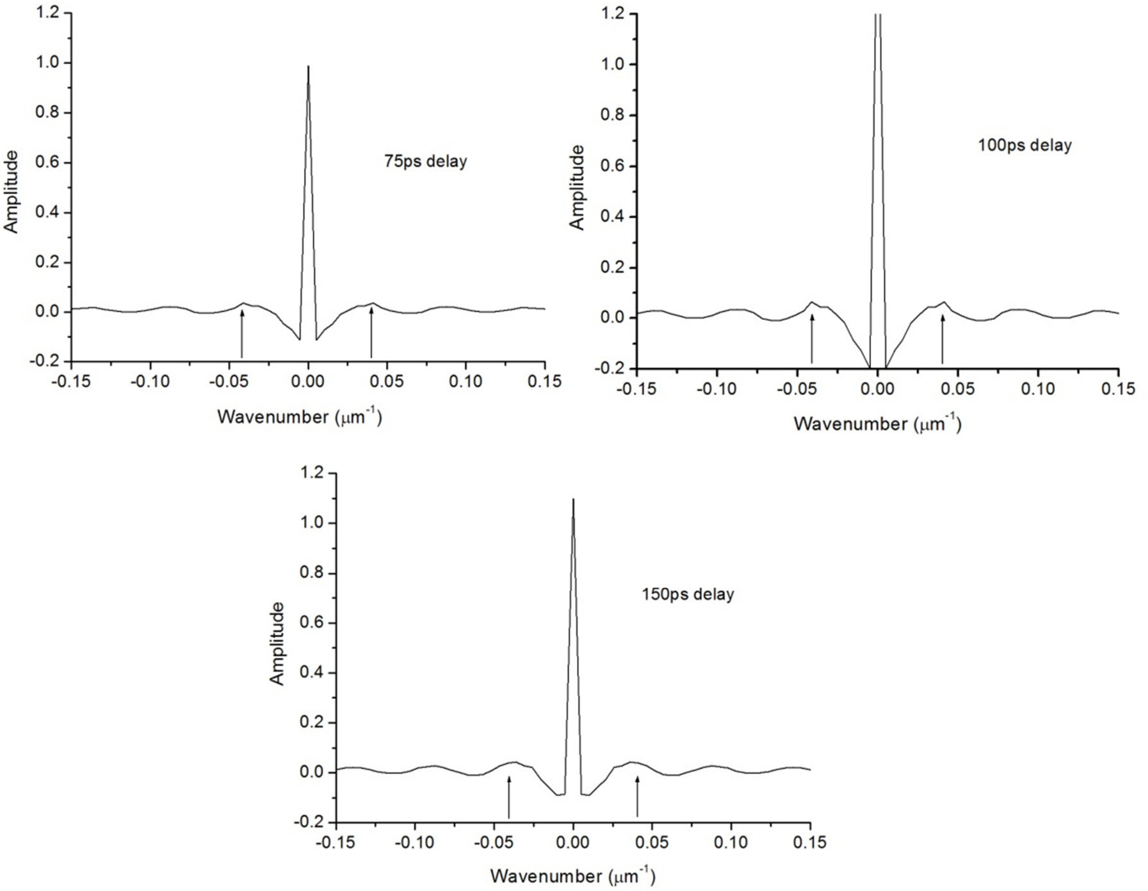

Figure 6.18 FFTs of the Ti K_α images at different time delays between the RT heating beam and the Ti K_α back-lighter beam.

The transmission data indicates that classical Rayleigh-Taylor growth dominates within the first 100ps of the interaction; an increase in ΔT means an increase in the oscillation between the two different layers and indicates the presence of RT 'finger-like' structures. The measured increase in ΔT corresponds to an increase in copper thickness of 350 ± 100 nm. This results in an instability amplitude of 650 ± 100 nm after 100ps and gives a Rayleigh-Taylor growth rate of $\gamma = 10 \pm 2$ ns^{-1}.

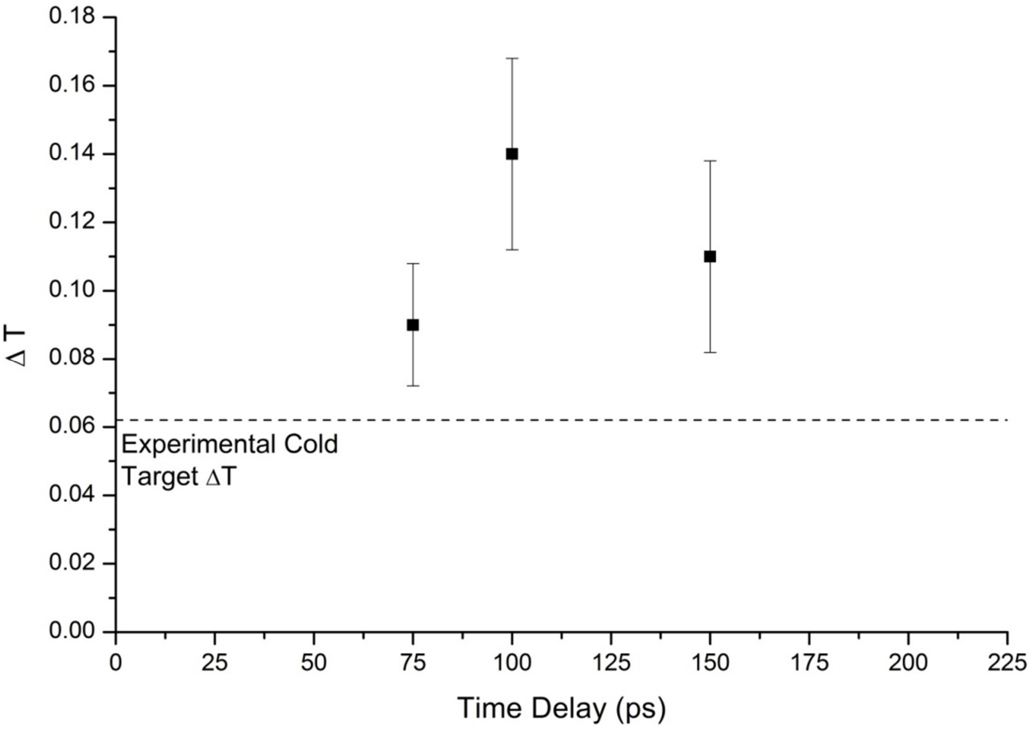

Figure 6.19 Summary of the *ΔT* results from the FFT analysis. The *ΔT* values shown here are twice the amplitude from the FFTs and represent the total change in transmission from peak to trough of the target perturbation. The dashed line represents the experimentally measured value of *ΔT* for the cold RT target.

Future work for this experiment involves collaboration with a research group who has access to a 2D hydrodynamic code in order to model the interaction. Further work will optimise the target design (or detection method) so as to improve the contrast and thus make a 2D Fourier transform feasible, potentially enabling spatial resolution through the target thickness. A 2D Fourier transform would give more information regarding frequencies present along the direction of the oscillation and would help to experimentally investigate the processes occurring after the period of RT growth, but this would require an initially greater thickness variation in the copper. Changing the perturbation wavelength of the RT unstable target would result in separating the delta and the sinc function within the Fourier transform which would be advantageous for smaller perturbation amplitudes.

6.5 Conclusion

The experiment outlined in this Chapter has utilised a titanium K_α source as a back-lighter to investigate the temporal evolution of the Rayleigh-Taylor instability in a laser-produced plasma. A laser plasma of parameters; $T_c = 300 - 400$eV, $T_h = 65$keV and $f = n_h/n_e = 0.28$ is produced by heating a Rayleigh-Taylor unstable target using the Vulcan laser system with an irradiance of 1×10^{20} W cm^{-2}. A target, seeded with an initial perturbation of amplitude 300nm between layers of copper and plastic, demonstrated Rayleigh-Taylor growth within the first 100ps of the interaction with a growth rate of 10 ± 2 ns^{-1}. Future work will include modelling this experiment using a 2 dimensional hydrodynamic code and improvements in the target design and detection method.

7. Conclusion

7.1 Summary

The work presented in this thesis has investigated methods of characterising and utilising emission in laser plasma experiments involving measurements of opacity. Three high power laser experiments have been undertaken and have utilised plasma based x-ray and EUV back-lighters to investigate plasma opacity and hydrodynamics. Diagnostic development has been undertaken in order to develop a new and more accurate method for determining a plasma hot electron temperature by analysing bremsstrahlung emission using filtered x-ray diodes.

A new method of compensating filters has been developed to investigate the bremsstrahlung emission spectrum from hot electrons. The compensating filters are used in conjunction with an x-ray diode array which has been developed for use with the Nd:YAG laser system at the University of York. The diode array and filtering has been optimised to calculate hot electron temperatures in the 5 – 15keV range and is found to agree well with single photon counting and has an accuracy of 0.5keV. The x-ray diode array demonstrated a rapid enhancement in hot electron generation when the laser ablated through a 2mm thick aluminium target, resulting in the laser firing into a conical frustum.

An experiment has been undertaken to exploit K_α emission as a back-lighter to probe plasma opacity of a heated target. A two layer target consisting of 0.8 μm Al and 1 μm Fe was heated using the laser system at the Bhabha Atomic Research Centre. The laser was incident onto the aluminium surface producing K_α emission and conductively heating the iron layer on the rear side of the target. By combining spectroscopic techniques with continuum analysis, the aluminium K_α back-lighter was fully characterised and the plasma parameters determined were used in hydrodynamic simulations. The experimental data for the opacity of iron was found to be in good agreement with opacities from the Ionised Material Package code for a 1.5keV photon energy.

A line focus EUV back-lighter created using the Vulcan laser has been well characterised through imaging the time and spectrally integrated emission profile using a crossed slit camera. A spatially dependant electron temperature profile has been inferred by applying a detailed model of emission to the crossed slit camera images. This temperature profile is a useful diagnostic indicating a low temperature and low ionisation, part of the reason why lasing was not observed. Simulations using Ehybrid demonstrated the laser energy was most effectively coupled at too high density which also inhibited amplification as photons were refracted out of the gain region.

The Rayleigh-Taylor (RT) instability has been investigated using a Ti K_α back-lighter to probe a RT unstable target, both of which are heated using two CPA pulses from the Vulcan laser system. The RT unstable target consisted of a 2μm layer of copper on 50μm plastic with a sinusoidal perturbation at the interface of wavelength 30μm and amplitude 300nm. The copper layer cools quicker via radiative cooling and establishes the RT instability. Rayleigh-Taylor growth is observed in the first 100 ps of the interaction with a growth rate of $\gamma = 10 \pm 2\ ns^{-1}$.

7.2 Future Work

Further experiments investigating plasma opacity will be carried out at the University of York, utilising the techniques outlined in Chapters 3 and 4. Initially experimentation will investigate the enhanced K_α source produced on ablative burn-through of an aluminium target. Using spectroscopic methods, the absolute K_α signal will be determined and compared to theory similar to the analysis in Chapter 6. The directionality of the K_α

source will be investigated to determine if there is any angular dependence or if there is an even distribution over 4π steradians. Once the K_α source has been characterised, opacity experiments of a similar design to that described in Chapter 4 will be undertaken. The irradiance regime of the laser situated at the Bhabha Atomic Research Centre is similar to that of the table top system at the University of York. This means a similar style of experiment is possible with the added advantage of a shorter pulse length of 170ps. However, the issues discussed in Chapter 4, such as axial and radial temperature gradients, need addressing.

The future opacity experiments using the York laser system could utilise tamped microdots to address the issue of temperature gradients within the produced plasma. Using a thin double layer target tamped both sides with plastic will help to address the issue of axial temperature gradients by inhibiting the expansion of the iron layer. The radial temperature gradients can be addressed through the use of microdot targets held in plastic. The significantly smaller target area would reduce the temperature gradient in the radial direction as the irradiance would be approximately constant across the area of the dot. The opaque region would be detachable from the surrounding plastic due to the difference in transmission. The plasma temperature of the iron layer could be deduced via time-gated optical imaging as discussed in Chapter 4 or by applying a detailed model of emission to an image integrated over a larger spectral region as described in Chapter 5. Provided the temperature gradients were minimised by using thin targets, the analysis described in Chapter 5 would be sufficiently accurate to deduce the temperature of the iron layer.

Further work investigating the Rayleigh-Taylor (RT) instability as described in Chapter 6 is planned in the near future. Different parameters are to be investigated, such as different perturbation wavelengths and amplitudes in order to ascertain the effects on the RT growth rate. Modelling using a 2 dimensional hydrodynamic code is to be carried out in order to compare the predicted growth rate with the experimental rate observed.

Appendix A: Recent Publications

[1] A. K. Rossall, I. A. Bush, C.P. Edwards, G. J. Tallents, N. C. Woolsey, K. Lancaster, T. Winstone, C. Spindloe, H. Lowe, W. Nazarov, P. Morantz, and J. Pasley, *Measurements of Rayleigh-Taylor instability growth in a layered target heated by a high power short pulse laser,* Central Laser Facility, UK, Annual Report 2010 - 2011.

[2] A. K. Rossall, G. J. Tallents, E. Wagenaars, and N. C. Woolsey, *Enhancement of X-ray Generation in a High Repetition Rate Laser-Plasma Experiment,* Accepted to IEEE Transactions on Plasma Science, Special Issue - Images in Plasma Science 2011.

[3] L. M. R. Gartside, G. J. Tallents, A. K. Rossall, E. Wagenaars, D. S. Whittaker, M. Kozlová, J. Nejdl, M. Sawicka, J. Polan, M. Kalal, and B. Rus, *Extreme ultraviolet interferometry of laser plasma material between the critical and ablation surfaces,* High Energy Density Physics 7 91-97 (2011)

[4] S. Chaurasia, S. Tripathi, D. S. Munda, G. Mishra, C. G. Murali, N. K. Gupta, L. J. Dhareshwar, A. K. Rossall, G. J. Tallents, R. Singh, D. K. Kohli and R. K. Khardekar *Laser interaction with low-density carbon foam* Pramana 75, 1191-1196 (2010).

[5] A. K. Rossall, E. Wagenaars, L. M. R. Gartside, N. Booth, G. J. Tallents, S. White, C. L. S. Lewis, M. M. Notley, and R. Heathcote *Characterization of a line-focus back-lighter* Central Laser Facility, UK, Annual Report 2009 - 2010.

[6] L. M. R. Gartside, G. J. Tallents, A. K. Rossall, E. Wagenaars, D. S. Whittaker, M. Kozlová, J. Nejdl, M. Sawicka, J. Polan, M. Kalal, and B. Rus *Extreme ultraviolet interferometry of warm dense matter in laser plasmas* Opt. Lett. 35, 3820-3822 (2010).

[7] A. K. Rossall, L. M. R. Gartside, S. Chaurasia, S. Tripathi, D. S. Munda, N. K. Gupta, L. J. Dhareshwar, J. Gaffney, S. J. Rose and G. J. Tallents *X-ray back lighter characterisation for iron opacity measurements using laser produced aluminium K-alpha emission* J. Phys. B: At. Mol. Opt. Phys. 43 (2010) 155403.

[8] S. Chaurasia, A. K. Rossall, D. S. Munda, S. Tripathi, L. J. Dhareshwar, and G. J. Tallents, *Optimization of x-ray line emission from copper plasma with laser focal spot* Journal of Physics: Conference Series 208 (2010) 012095

[9] E. Wagenaars, L. M. R. Gartside, A. K. Rossall, N. Booth, S. White, C. L. S. Lewis, M. M. Notley, R. Heathcote, and G. J. Tallents *Laboratory measurements of hot iron opacities at EUV wavelengths*, Proc. SPIE 7451, 74510G (2009)

[10] G. J. Tallents, N. Booth, M. H. Edwards, L. M. R. Gartside, H. Huang, A. K. Rossall, E. Wagenaars, D. S. Whittaker and Z. Zhai *X-Ray Lasers as Probes of Plasma Parameters*, X-Ray Lasers 2008, Springer Proceedings in Physics, Volume 130, ISBN: 978-1-4020-9923-6 (Print) 978-1-4020-9924-3 (Online)

References

[1] J. Gordon, H. Zeiger, and C. Townes, Physical Review **95**, 282-284 (1954).

[2] S. Eliezer, Plasma Physics and Controlled Fusion **45**, 181 (2003).

[3] D. Strickland and G. Mourou, Optics Communications **56**, 219-221 (1985).

[4] F. Serduke, E. Minguez, S. Davidson, and C. Iglesias, Journal Of Quantitative Spectroscopy and Radiative Transfer **65**, 527-541 (2000).

[5] S. J. Rose, Journal Of Quantitative Spectroscopy and Radiative Transfer **51**, 317-318 (1994).

[6] A. Rickert, Journal Of Quantitative Spectroscopy and Radiative Transfer **54**, 325-332 (1995).

[7] G. B. Rybicki and A. P. Lightman, *Radiative Processes In Astrophysics* (Wiley VCH, 1985), p. 400.

[8] J. N. Bahcall, A. M. Serenelli, and S. Basu, The Astrophysical Journal **621**, L85-L88 (2005).

[9] E. Mínguez, P. Martel, J. M. Gil, J. G. Rubiano, and R. Rodríguez, Fusion Engineering and Design **60**, 8 (2002).

[10] J. E. Bailey, G. A. Chandler, R. C. Mancini, S. A. Slutz, G. A. Rochau, M. Bump, T. J. Buris-Mog, G. Cooper, G. Dunham, I. Golovkin, J. D. Kilkenny, P. W. Lake, R. J. Leeper, R. Lemke, J. J. MacFarlane, T. A. Mehlhorn, T. C. Moore, T. J. Nash, A. Nikroo, D. S. Nielsen, K. L. Peterson, C. L. Ruiz, D. G. Schroen, D. Steinman, and W. Varnum, Physics Of Plasmas **13**, 056301 (2006).

[11] K. Nazir, S. J. Rose, A. Djaoui, G. J. Tallents, M. G. Holden, P. A. Norreys, P. Fews, J. Zhang, and F. Failles, Appl. Phys. Lett. **69**, 3686-3688 (1996).

[12] T. J. Orzechowski, M. D. Rosen, H. N. Kornblum, J. L. Porter, L. J. Suter, A. R. Thiessen, and R. J. Wallace, Physical Review Letters 3545-3548 (1996).

[13] S. Davidson, J. Foster, C. Smith, K. Warburton, and S. J. Rose, Applied Physics Letters **52**, 847 (1988).

[14] T. Perry, S. Davidson, F. Serduke, D. Bach, C. Smith, J. Foster, R. Doyas, R. Ward, C. Iglesias, F. Rogers, J. Abdallah, R. Stewart, J. Kilkenny, and R. Lee, Physical Review Letters **67**, 3784-3787 (1991).

[15] P. Springer, D. Fields, B. Wilson, J. Nash, W. Goldstein, C. Iglesias, F. Rogers, J. Swenson, M. Chen, A. Bar-Shalom, and R. Stewart, Physical Review Letters **69**, 3735-3738 (1992).

[16] J. Foster, D. Hoarty, C. Smith, P. Rosen, S. Davidson, S. Rose, T. Perry, and F. Serduke, Physical Review Letters **67**, 3255-3258 (1991).

[17] M. Edwards, D. Whittaker, P. Mistry, N. Booth, G. Pert, G. Tallents, B. Rus, T. Mocek, M. Koslová, C. McKenna, A. Delserieys, C. Lewis, M. Notley, and D. Neely, Physical Review Letters **97**, (2006).

[18] C. Chenais-Popovics, H. Merdji, T. Missalla, F. Gilleron, J. C. Gauthier, T. Blenski, F. Perrot, M. Klapisch, C. Bauche-Arnoult, J. Bauche, A. Bachelier, and K. Eidmann, The Astrophysical Journal Supplement Series **127**, 275-281 (2000).

[19] B. Dromey, M. Zepf, A. Gopal, K. Lancaster, M. S. Wei, K. Krushelnick, M. Tatarakis, N. Vakakis, S. Moustaizis, R. Kodama, M. Tampo, C. Stoeckl, R. Clarke, H. Habara, D. Neely, S. Karsch, and P. Norreys, Nature Physics **2**, 456-459 (2006).

[20] P. Norreys, M. Zepf, S. Moustaizis, A. Fews, J. Zhang, P. Lee, M. Bakarezos, C. Danson, A. Dyson, P. Gibbon, P. Loukakos, D. Neely, F. Walsh, J. Wark, and A. Dangor, Physical Review Letters **76**, 1832-1835 (1996).

[21] M. Zepf, G. Tsakiris, G. Pretzler, I. Watts, D. Chambers, P. Norreys, U. Andiel, A. Dangor, K. Eidmann, C. Gahn, A. Machacek, J. Wark, and K. Witte, Physical Review E **58**, R5253-R5256 (1998).

[22] U. Teubner and P. Gibbon, Reviews Of Modern Physics **81**, 445-479 (2009).

[23] B. Nagler, U. Zastrau, Roland R. Fäustlin, S. M. Vinko, T. Whitcher, A. J. Nelson, R. Sobierajski, J. Krzywinski, J. Chalupsky, E. Abreu, S. Bajt, T. Bornath, T. Burian, H. Chapman, J. Cihelka, T. Döppner, S. Düsterer, T. Dzelzainis, M. Fajardo, E. Förster, C. Fortmann, E. Galtier, S.H. Glenzer, S. Göde, G. Gregori, V. Hajkova, P. Heimann, L. Juha, M. Jurek, F. Y. Khattak, A. R. Khorsand, D. Klinger, M. Kozlova, T. Laarmann, H. J. Lee, R. W. Lee, K.-H. Meiwes-Broer, P. Mercere, W. J. Murphy, A. Przystawik, R. Redmer, H. Reinholz, D. Riley, G. Röpke, F. Rosmej, K. Saksl, R. Schott, R. Thiele, J. Tiggesbäumker, S. Toleikis, T. Tschentscher, I. Uschmann, H. J. Vollmer, and J. S. Wark, Nature Physics **5**, 693-696 (2009).

[24] W. L. Kruer, *The Physics Of Laser Plasma Interactions* (Westview Press, 2003).

[25] G. J. Pert, Journal Of Fluid Mechanics **131**, 401 (1983).

[26] A.G. Mordovanakis, P. Masson-Laborde, J. Easter, K. Popov, B. Hou, G. Mourou, W. Rozmus, M. G. Haines, J. Nees, and K. Krushelnick, Applied Physics Letters **96**, 071109 (2010).

[27] M. Haines, M. Wei, F. Beg, and R. Stephens, Physical Review Letters **102**, 045008 (2009).

[28] F. N. Beg, A. R. Bell, A. E. Dangor, C. N. Danson, A. P. Fews, M. E. Glinsky, B. A. Hammel, P. Lee, P. A. Norreys, and M. Tatarakis, Physics Of Plasmas **4**, 447 (1997).

[29] M. Tabak, J. Hammer, M.E. Glinsky, W.L. Kruer, S. C. Wilks, J. Woodworth, E. M. Campbell, M. D. Perry, and R. J. Mason, Physics Of Plasmas **1**, 1626 (1994).

[30] S.C. Wilks and W.L. Kruer, IEEE Journal Of Quantum Electronics **33**, 1954-1968 (1997).

[31] E. Wagenaars, D.S. Whittaker, and G.J. Tallents, High Energy Density Physics (2010).

[32] T. Fujimoto, *Plasma Spectroscopy* (Oxford University Press, 2004).

[33] D. Salzmann, *Atomic Physics In Hot Plasmas* (Oxford University Press US, 1998).

[34] W. J. Karzas and R. Latter, The Astrophysical Journal Supplement Series **6**, 167 (1961).

[35] R. Pratt, Akiva Ron, and H. Tseng, Reviews Of Modern Physics **45**, 273-325 (1973).

[36] S. Oh, J. McEnnan, and R. Pratt, Physical Review A **14**, 1428-1436 (1976).

[37] D. Botto, J. McEnnan, and R. Pratt, Physical Review A **18**, 580-586 (1978).

[38] S. J. Rose, The Astrophysical Journal **453**, L45-L47 (1995).

[39] S. J. Rose, Journal Of Physics B: Atomic, Molecular and Optical Physics **26**, L29-L34 (1993).

[40] C. J. Hansen, S. D. Kawaler, and V. Trimble, *Stellar Interiors: Physical Principles, Structure, and Evolution* (Springer, 2004).

[41] F. Serduke, Journal Of Quantitative Spectroscopy and Radiative Transfer **65**, 527-541 (2000).

[42] C. Bauche-Arnoult, J. Bauche, and M. Klapisch, Physical Review A **31**, 2248-2259 (1985).

[43] C. Bauche-Arnoult, J. Bauche, and M. Klapisch, Physical Review A **30**, 3026-3032 (1984).

[44] H. Chung, M. Chen, W. Morgan, Y. Ralchenko, and R. Lee, High Energy Density Physics **1**, 3-12 (2005).

[45] G. Pert, Journal Of Computational Physics **27**, 241-255 (1978).

[46] P. Hagelstein, M. Rosen, and V. Jacobs, Physical Review A **34**, 1931-1937 (1986).

[47] H. R. Griem, *Plasma Spectroscopy* (McGraw-Hill, 1964), p. 580.

[48] G.J. Pert, Laser and Particle Beams **12**, 209-222 (1994).

[49] R. E. W. Pfund, R. Lichters, and J. Meyer-ter-Vehn, AIP Conference Proceedings **426**, 141-146 (1998).

[50] C. K. Birdsall and A. B. Langdon, *Plasma Physics Via Computer Simulation* (Taylor & Francis, 2004), p. 479.

[51] J. Villasenor and O. Bunemann, Computer Physics Communications **69**, 306-316 (1992).

[52] S Eliezer, Plasma Physics and Controlled Fusion **45**, 181-181 (2003).

[53] D. Salzmann, Ch. Reich, I. Uschmann, E. Förster, and P. Gibbon, Physical Review E **65**, 036402 (2002).

[54] J. Hares, J. Kilkenny, M. Key, and J. Lunney, Physical Review Letters **42**, 1216-1219 (1979).

[55] T. Nakamura, K. Mima, H. Sakagami, T. Johzaki, and H. Nagatomo, Laser and Particle Beams **26**, 207-212 (2008).

[56] R. E. Kidder, Nuclear Fusion **21**, 145-151 (1981).

[57] J. J. Honrubia, M. Kaluza, J. Schreiber, G. D. Tsakiris, and J. Meyer-ter-Vehn, Physics Of Plasmas **12**, 052708 (2005).

[58] A. Maksimchuk, S. Gu, K. Flippo, and D. Umstadter, Physical Review Letters **84**, 4108-4111 (2000).

[59] J. Sparkes, *Semiconductor Devices, 2nd Edition* (Taylor and Francis, 1994).

[60] OSI Optoelectronics company website: http://www.osioptoelectronics.com, (accessed 21st October 2010).

[61] T. E. Hansen, Physica Scripta **18**, 471-475 (1978).

[62] B. Henke, Atomic Data and Nuclear Data Tables **54**, 181-342 (1993).

[63] Ortec company website: http://www.ortec-online.com, (accessed 21st October 2010).

[64] C. Stoeckl, W. Theobald, T. C. Sangster, M. H. Key, P. Patel, B. B. Zhang, R. Clarke, S. Karsch, and P. Norreys, Review Of Scientific Instruments **75**, 3705 (2004).

[65] K. Yasuike, M. H. Key, S. P. Hatchett, R. A. Snavely, and K. B. Wharton, Review Of Scientific Instruments **72**, 1236 (2001).

[66] F. Ewald, H. Schwoerer, and R. Sauerbrey, Europhysics Letters (EPL) **60**, 710-716 (2002).

[67] B. F. Lasinski, A. B. Langdon, C. H. Still, M. Tabak, and R. P. J. Town, Physics Of Plasmas **16**, 012705 (2009).

[68] F. W. Perkins and E. J. Valeo, Physical Review Letters **32**, 1234 LP - 1237 (1974).

[69] C. J. Walsh, D. M. Villeneuve, and H. A. Baldis, Physical Review Letters **53**, 1445 LP - 1448 (1984).

[70] A. L. Lei, K. A. Tanaka, R. Kodama, G. R. Kumar, K. Nagai, T. Norimatsu, T. Yabuuchi, and K. Mima, Physical Review Letters **96**, 255006 (2006).

[71] B. S. Paradkar, M. S. Wei, T. Yabuuchi, R. B. Stephens, M. G. Haines, S. I. Krasheninnikov, and F. N. Beg, Physical Review E **83**, 46401 (2011).

[72] T. Nakamura, M. Tampo, R. Kodama, S. V. Bulanov, and M. Kando, Physics Of Plasmas **17**, 113107 (2010).

[73] M. H. Key, M. D. Cable, T. E. Cowan, K. G. Estabrook, B. A. Hammel, S. P. Hatchett, E. A. Henry, D. E. Hinkel, J. D. Kilkenny, J. A. Koch, W. L. Kruer, A. B. Langdon, B. F. Lasinski, R. W. Lee, B. J. MacGowan, A. MacKinnon, J. D. Moody, M. J. Moran, A. A. Offenberger, D. M. Pennington, M. D. Perry, T. J. Phillips, T. C. Sangster, M. S. Singh, M. A. Stoyer, M. Tabak, G. L. Tietbohl, M. Tsukamoto, K. Wharton, and S. C. Wilks, Physics Of Plasmas **5**, 1966 (1998).

[74] M. A. R. Patoary, M. Alfaz Uddin, A. K. F. Haque, M. Shahjahan, A. K. Basak, M. R. Talukder, and B. C. Saha, International Journal Of Quantum Chemistry **109**, 897-906 (2009).

[75] A. K. Rossall, L. M. R. Gartside, S. Chaurasia, S. Tripathi, D. S. Munda, N. K. Gupta, L. J. Dhareshwar, J. Gaffney, S. J. Rose, and G. J. Tallents, Journal Of Physics B: Atomic, Molecular and Optical Physics **43**, 155403 (2010).

[76] J Meyer-ter-Vehn, Plasma Physics and Controlled Fusion **43**, A113 (2001).

[77] Z. L. Chen, R. Kodama, M. Nakatsutsumi, H. Nakamura, M. Tampo, K. A. Tanaka, Y. Toyama, T. Tsutsumi, and T. Yabuuchi, Physical Review E **71**, (2005).

[78] B. Chrisman, Y. Sentoku, and A. J. Kemp, Physics Of Plasmas **15**, 056309 (2008).

[79] S. E. Coe, T. Afshar-Rad, and O. Willi, Europhysics Letters (EPL) **13**, 251-256 (1990).

[80] I. H. Hutchinson, *Principles Of Plasma Diagnostics* (Cambridge University Press, 2002), p. 440.

[81] A. H. Gabriel, Mon. Not. Astron. Soc. **160**, 99 (1972).

[82] National Institute of Standards and Technology: http://physics.nist.gov/asd, (accessed 12th November 2011).

[83] H. Chung, (Private Communication) Post-processor Used To Broaden theoretical FLYCHK Spectra **NIST**, (2008).

[84] J. Larsen, (Cascade Applied Sciences, Inc., Longmont, Colo.) (2010).

[85] S.P. Lyon and J.D. Johnson, Los Alamos National Laboratory Report LA-UR-92-3407 (1992).

[86] S. J. Rose, Journal Of Physics B: Atomic, Molecular and Optical Physics **25**, 1667 (1992).

[87] J. Colgan, J. Abdallah Jr., C.J. Fontes, D.P. Kilcrease, J. Dunn, M. Purvis, and R.W. Lee, High Energy Density Physics **6**, 295-300 (2010).

[88] C. Corliss and J. Sugar, Journal Of Physical and Chemical Reference Data **11**, 135 (1982).

[89] T. Perry, P. Springer, D. Fields, D. Bach, F. Serduke, C. Iglesias, F. Rogers, J. Nash, M. Chen, B. Wilson, W. Goldstein, B. Rozsynai, R. Ward, J. Kilkenny, R. Doyas, L. Da Silva, C. Back, R. Cauble, S. Davidson, J. Foster, C. Smith, A. Bar-Shalom, and R. Lee, Physical Review E **54**, 5617-5631 (1996).

[90] A. K. Rossall, E. Wagenaars, L. M. R. Gartside, N. Booth, G. J. Tallents, S. White, C. L. S. Lewis, M. M. Notley, and R. Heathcote, CLF Annual Report 8 (2010).

[91] E. Wagenaars, L. M. R. Gartside, A. K. Rossall, N. Booth, S. White, C. L. S. Lewis, M. M. Notley, R. Heathcote, and G. J. Tallents, in *Soft X-Ray Lasers and Applications VIII*, edited by James Dunn and Gregory J. Tallents (SPIE, San Diego, CA, USA, 2009), p. 74510G-8.

[92] H. Puell, H. J. Neusser, and W. Kaiser, Z. Naturforsch A **25**, 1815 (1970).

[93] G. P. Gupta and A. Z. Msezane, Physica Scripta **77**, 035303 (2008).

[94] J. Reader, V. Kaufman, J. Sugar, J. O. Ekberg, U. Feldman, C. M. Brown, J. F. Seely, and W. L. Rowan, Journal Of the Optical Society Of America B **4**, 1821 (1987).

[95] J. O. Ekberg, A Redfors, C M Brown, U Feldman, and J F Seely, Physica Scripta **44**, 539-547 (1991).

[96] G. Yuan, Y. Kato, H. Daido, R. Kodama, K. Murai, and T. Kagawa, Physica Scripta **53**, 197-203 (1996).

[97] B. C. Fawcett and R. W. Hayes, Journal Of the Optical Society Of America **65**, 623 (1975).

[98] R. Smith, J. Dunn, J. Filevich, S. Moon, J. Nilsen, R. Keenan, V. Shlyaptsev, J. Rocca, J. Hunter, and M. Marconi, Physical Review E **72**, 036404 (2005).

[99] G. J. Tallents, Journal Of Physics D: Applied Physics **36**, R259-R276 (2003).

[100] Lord Rayleigh, Proc. London Math. Soc. **s1-14**, 170-177 (1883).

[101] B.A. Hammel, S.W. Haan, D.S. Clark, M.J. Edwards, S.H. Langer, M.M. Marinak, M.V. Patel, J.D. Salmonson, and H.A. Scott, High Energy Density Physics **6**, 171-178 (2010).

[102] D. Sharp, Physica D: Nonlinear Phenomena **12**, 3-18 (1984).

[103] J. Jeff Hester, Annual Review Of Astronomy and Astrophysics **46**, 127-155 (2008).

[104] K. L. Lancaster, J. Pasley, J. S. Green, D. Batani, S. Baton, R. G. Evans, L. Gizzi, R. Heathcote, C. Hernandez Gomez, M. Koenig, P. Koester, A. Morace, I. Musgrave, P. A. Norreys, F. Perez, J. N. Waugh, and N. C. Woolsey, Physics Of Plasmas **16**, 056707 (2009).

[105] P. M. Nilson, W. Theobald, J. Myatt, C. Stoeckl, M. Storm, O. V. Gotchev, J. D. Zuegel, R. Betti, D. D. Meyerhofer, and T. C. Sangster, Physics Of Plasmas **15**, 056308 (2008).

[106] J. Myatt, W. Theobald, J. A. Delettrez, C. Stoeckl, M. Storm, T. C. Sangster, A. V. Maximov, and R. W. Short, Physics Of Plasmas **14**, 056301 (2007).

[107] S. Baton, M. Koenig, P. Guillou, B. Loupias, A. Benuzzimounaix, J. Fuchs, C. Rousseaux, L. Gremillet, D. Batani, and A. Morace, High Energy Density Physics **3**, 358-364 (2007).

[108] Ch. Reich, P. Gibbon, I. Uschmann, and E. Förster, Physical Review Letters **84**, 4846-4849 (2000).

[109] K. Rifai, F. Vidal, and T. W. Johnston, Physics Of Plasmas **14**, 082311 (2007).

[110] H.J. Kull, Physics Reports **206**, 197-325 (1991).

[111] Origin (OriginLab, Northampton, MA) (2010).

[112] Glenn D. Boreman, *Modulation Transfer Function In Optical and Electro-optical Systems* (SPIE Press, 2001), p. 10.

[113] B. Beckhoff, N. Langhoff, B. Kanngiefer, R. Wedell, and H. Wolff, *Handbook Of Practical X-ray Fluorescence Analysis* (Springer, 2006), p. 863.

[114] R. Lichters, Relativistische Wechselwirkung Intensiver Kurzer Laserpulse Mit Uberdichten Plasmen: Erzeugung Hoher Harmonischer, PhD Thesis Technische Universitat Munchen, 1997.

[115] A. Bourdier, Physics Of Fluids **26**, 1804 (1983).

[116] P. Neumayer, B. Aurand, M. Basko, B. Ecker, P. Gibbon, D. C. Hochhaus, A. Karmakar, E. Kazakov, T. Kühl, C. Labaune, O. Rosmej, An. Tauschwitz, B. Zielbauer, and D. Zimmer, Physics Of Plasmas **17**, 103103 (2010).

[117] W. Theobald, K. Akli, R. Clarke, J. A. Delettrez, R. R. Freeman, S. Glenzer, J. Green, G. Gregori, R. Heathcote, N. Izumi, J. A. King, J. A. Koch, J. Kuba, K. Lancaster, A. J. MacKinnon, M. Key, C. Mileham, J. Myatt, D. Neely, P. A. Norreys, H.-S. Park, J. Pasley, P. Patel, S. P. Regan, H. Sawada, R. Shepherd, R. Snavely, R. B. Stephens, C. Stoeckl, M. Storm, B. Zhang, and T. C. Sangster, Physics Of Plasmas **13**, 043102 (2006).

[118] J. H. Hubbell, P. N. Trehan, Nirmal Singh, B. Chand, D. Mehta, M. L. Garg, R. R. Garg, Surinder Singh, and S. Puri, Journal Of Physical and Chemical Reference Data **23**, 339 (1994).

[119] R. Harrach and R. Kidder, Physical Review A **23**, 887-896 (1981).

[120] National Institute of Standards and Technology: http://srdata.nist.gov/gateway/gateway, (accessed 12th November 2010).

[121] M. Edwards, D. Whittaker, G. Tallents, P. Mistry, G. Pert, B. Rus, T. Mocek, M. Kozlová, J. Polan, A. Praeg, M. Stupka, and P. Homer, Physical Review Letters **99**, (2007).

[122] J. P. Santos, F. Parente, and Y.-K. Kim, Journal Of Physics B: Atomic, Molecular and Optical Physics **36**, 4211-4224 (2003).

[123] X. Llovet et al, Journal Of Physics B: Atomic, Molecular and Optical Physics **33**, 3761 (2000).

[124] D. J. Cookson, Journal Of Synchrotron Radiation **5**, 1375-82 (1998).